AN EXPERIMENTALLY-VALIDATED COUPLED OPTO-THERMAL-ELECTRICAL MODEL FOR PV PERFORMANCE AND RELIABILITY

A Dissertation

Submitted to the Faculty

of

Purdue University

by

Yubo Sun

In Partial Fulfillment of the

Requirements for the Degree

of

Doctor of Philosophy

May 2020

Purdue University

West Lafayette, Indiana

THE PURDUE UNIVERSITY GRADUATE SCHOOL
STATEMENT OF DISSERTATION APPROVAL

Dr. Peter Bermel, chair

School of Electrical and Computer Engineering

Dr. Mark Lundstrom

School of Electrical and Computer Engineering

Dr. Minghao Qi

School of Electrical and Computer Engineering

Dr. Zhihong Chen

School of Electrical and Computer Engineering

Approved by:

Dr. Dimitrios Peroulis

Head of the school of Electrical and Computer Engineering

This thesis is dedicated to my parents, my wife and my son for their selfless love, support and sacrifices.

ACKNOWLEDGMENTS

I would like to extend my sincere appreciation to my advisor, Professor Peter Bermel, for allowing me to conduct research in his group as a PhD student over past few years, for his continuous mentorship from academic perspective and generous support from financial perspective during these years. He always provides me with useful suggestions and valuable advice to drive my research forward. His expertise in modeling of Optoelectronic devices leads me to break through obstacles in research and helps me enhance the quality of my research work.

I am grateful to Professor Mark Lundstrom for serving as my PhD committee member, and his tutoring to help me establish fundamental skills in performing academic research since I was an undergraduate. I also benefits a lot from his outstanding lectures in carrier transport, fundamental semiconductor devices, without which I would not be able to build up good basis for my research.

I like to thank Professor Minghao Qi for serving as my PhD committee member. His lecture in physics and manufacturing of solar cells solidify my understanding of photovoltaic devices from both theoretical and experimental perspectives. His insightful questions on my research are always great guidance to improve my research quality.

I am thankful to Professor Zhihong Chen for serving as my PhD committee member. I especially thank her for allowing me to attend her research group meeting when I was an undergraduate which offers me the opportunity to understand graduate research better. Her lecture in introduction to electron design and analysis directs me to set up good knowledge basis in semiconductor devices.

I would also like to thank Professor Muhammad A. Alam and Professor Rakesh Agrawal for their innovative insights and kind help on my research work from physics and chemical engineering perspective. I could not make significant progress in my

research without their inputs and contributions as the leading professors in Network for Photovoltaics group.

I would also like to express my appreciation to Dr. Kyle Montgomery, Dr. Stephanie Tomasulo, Dr. Sudhajeet Misra, Dr. Mark Hettick, Dr. Caroline Sutter-Fella, Dr. Benoit Gaury, Dr. Paul Haney, Professor Minjoo L. Lee, Professor Ali Javey and Professor Michael A. Scarpulla for their collaborations with me in conducting research projects and publishing research outcome.

I would like to thank all the present and past members from Professor Peter Bermel's research group: Dr. Xufeng Wang, Chao Zhou, Dr. Haejun Chung, Dr. Enas Sakr, Dr. Roman Shugayev, Hao Tian, Dr. Zhiguang Zhou, Evan Schlenker, Dan Kanopa, Sayan Roy, Elizabeth Grubbs, David Kortge, Ze Wang, Allison Perna, Oluseye Akomolede, Haimabati Dey and Jie Zhu, with whom I have a great time work closely in the past few years. I treasure most the friendship we established and collaborations we made in solving scientific problems together.

I would like show my gratitude to all the past and present members from Network for Photovoltaics Technology: Dr. Ryyan Khan, Dr. Raghu Chavali, Dr. Xingshu Sun, Reza Asadpour, Tahir Patel, Dr. James Moore, Kevon Charles, Dr. Charles Hages, Dr. Mark Koeper, Dr. Xianyi Hu, Dr. Scott McClary, Dr. Brain Graeser, Ryan Ellis, David Rokke, Swapnil Deshmukh, Joseph Andler, Essam Alruqobah for inspiring me with their high-quality research presentations and their invaluable opinions to my research work.

I would like to thank Vicki Johnson, Christine Ramsey, Joanne Lax, Brooke Davies, Steckel Blair, Vicki Leavitt, Michelle Wagner, Matt Golden, and Elisheba Vanwinkle for their help in scheduling meetings, reserving rooms and administrative assistance.

Last but not least, I would like to express my deepest gratefulness to my family. I would like to thank my parents: Jianjun Sun and Xiangdong Liu for their countless love and support towards every aspect of my life. I would like to show my gratitude to my wife: Shaoou Chen for taking care of our family, giving birth to our son Liam Sun,

the most precious gift I received in my life. Without the joint efforts and sacrifices from the whole family, I would not be able to pursue Ph.D.

TABLE OF CONTENTS

Page

Page

LIST OF TABLES

LIST OF FIGURES

Figure Page

Figure Page

Figure Page

Figure Page

Figure Page

ABSTRACT

Sun Yubo Ph.D., Purdue University, May 2020. An Experimentally-validated Coupled Opto-Thermal-Electrical Model for PV Performance and Reliability. Major Professor: Peter A. Bermel.

Photovoltaics (PV) are a renewable energy technology experiencing rapidly increasing commercial adoption today. Nonetheless, many proposed PV applications still require higher efficiencies, lower costs and comparable reliability to currently available in commercial devices (typically made from silicon). To enable the rigorous study of a much wider range of materials and novel design concepts, particularly those based on compound thin films, Concentrated Photovoltaics (CPV), cells with bifaciality, a comprehensive modeling framework is developed to couple photon absorption, carrier transport, photon recycling, and thermal transport in PV devices. The universality of this framework manifest itself in approaching various PV related problems as follows: 1) exploring the novel design of wide-E_g GaInP solar cells as an intermediate step to enhance the efficiency of multijunction PV devices; 2) characterizing the open-circuit voltage (V_{OC}) degradation in thin-film vapor liquid solid (TF-VLS) grown InP solar cell through combined device and circuit model for interpreting photoluminescence (PL) image; 3) establishing optic-electric-thermal coupled framework to assess and compare the passive cooling effect for Silicon CPV devices that employ porous soda-lime glass radiative cooler and conventional copper cooler respectively; 4) Investigating and formulating the analytic solution of the optimal design that minimizes combined optical shadowing loss and electrical resistive loss for two types of bifacial PV devices: a) interdigitated back contact (IBC) Silicon heterojunction (SHJ) solar cells and b) Copper Indium Gallium DiSelenide (CIGSe) solar cell with Al_2O_3 passivation; and 5) Constructing an Neural Network Autoen-

coder (NNA) that compresses and reconstructs the J-V characteristics obtained from TCAD simulation and literature for rapid screening and automated classification.

1. INTRODUCTION

1.1 Overview of PV technology

The steady growth of renewable energy is now significantly supplementing conventional energy sources such as coals, natural gas and oil etc., and allows society to address environmental issues that may arise from CO_2 emissions [1].Photovoltaics (PV) is the fastest growing renewable energy generation technology based on capacity added in 2017; it makes up 18% of total renewable generation capacity globally [2]. As PV become increasingly important, levelized cost of energy (LCOE) is acknowledged to be a vital metric for wider adoption. Despite the fact that LCOE of utility scale PV has been reduced substantially in recent years, the major obstacle preventing PV from becoming the dominant energy generation resource is still the relatively high LCOE compared to other conventional energy resources [3]. Further reduction of LCOE would require improvement of PV industry from three perspectives: 1). decreasing the cost of solar panel manufacturing process (e.g. scalable roll-to-roll printing technique replaces vacuum processed film growth recipe) [4]; 2). enhancing the power output and/or solar power conversion efficiency for a fixed footprint of solar module (e.g. *bifacial* PV allows sunlight to be absorbed at both sides of solar module [5]); 3). expanding the lifespan of PV cells through developing reliable solar devices with prolonged stability [6].

The topics covered in this thesis aim to address challenges and improvements of PV from aforementioned three perspectives. 1). From the perspective of manufacturing process cost reduction, a novel cost effective design approach for InP solar cells is evaluated and open-circuit voltage (V_{OC}) degradation is understood through rigorous device and circuit level modeling; 2). To combat the challenge of efficiency/power output enhancement, a novel design principle for high efficiency III-V compound

GaInP solar cell is assessed through analytical and numerical modeling efforts; optimization and development of bifacial Silicon (Si) and Copper Indium Gallium di-Selenide (CIGS) solar cells are achieved by opto-electric coupled device model and well-calibrated analytic formula; 3). For the sake of enhancing the reliability and stability of PV cells, an opto-electro-thermal coupled framework with self-consistent calculation of energy-balanced equation is implemented to investigate the novel radiative cooling effect for Silicon Concentrating Photovoltaics (CPV). In addition, a machine learning framework for data compression and clustering is developed to meet the demand of rapid screening and automated detection of PV cell performance by PV manufacturers.

1.2 Outline of thesis

In this thesis, we will be covering several absorber material systems of Photovoltaics from the aspects of device performance and reliability. We will be establishing multi-physics based modeling framework that couple opto-thermal-electric components to tackle various challenges for different type of solar cells. The framework developed in this thesis is validated by the benchmark of the modeling results against experiments. The breadth of topics covered in the thesis provides insights and solutions to novel concepts/design proposed in the PV community. Essentially, four main topics are deployed in details in this thesis:

1. III-V compound solar cells (chapter 2, 3, and 4): By coupling the optical generation and electron transport within the multi-layered structure, the device modeling can accurately capture the drift-diffusion process of generated carriers and predict the collection efficiency of III-V compound solar cells. The framework lays a solid foundation for exploration of novel design concept, explanation of performance degradation in the cost effective growth method, and investigation of alternative structure for improvement.

2. Radiative cooling (chapter 5): By coupling the temperature and illumination intensity dependent efficiency of concentrator photovoltaics with convective, conductive, and radiative heat transfer into an opto-electric-thermal coupled energy balance equation, equilibrium operational temperature of CPV devices can be obtained to help assess the effectiveness of different passive cooling techniques.

3. *Bifacial* solar cells (chapter 6 and 7): By allowing front and rear side absorption of sunlight into the multi-layered solar cell structure, the established opto-electric coupling framework can help identify the optimal design of manufactured bifacial cells for maximum power output.

4. Machine Learning in PV (chapter 8): We will build neural network autoencoder that compress and reconstruct the J-V characteristics for clustering pattern generation and analysis. Our results pave the way for realization of rapid screening and automated detection of manufactured cell performance.

Detailed outline of each chapter is given as follows:

In chapter 2, the goal of this chapter is to reproduce the experimentally measured performance of wide-bandgap ($E_g = 2.1$ eV) GaInP solar cells, and then to propose an upgraded design of the multi-layered structure for efficiency enhancement. We will frame a device model that captures essential physics of the wide-E_g GaInP operation and analyze the major source of efficiency loss. First, detailed absorption data for the Ga-rich alloy is obtained by extrapolating literature values for InP and $Ga_{0.5}In_{0.5}P$. We then combine these values with estimates of carrier lifetime (0.1 ns) and interface recombination (9×10^5 cm/s) to construct detailed electro-optical models. They are found to accurately reproduce the EQE, Jsc, and Voc observed in published experimental devices. Small discrepancies of 0.1% are caused by slight differences in optical constants and interface recombination. This modeling process illustrates the major sources of loss, namely interface recombination between the emitter and window layer and low bulk minority carrier lifetimes in the active region. An improved

design is also proposed and implemented in this framework, which involves adjusting the doping and thickness of key layers. These findings will help define a path towards increasing the performance of these wide E_g cells to approach their theoretical limit – approximately 16.5%.

In chapter 3, the goal of this chapter is to find out and quantify the efficiency gap between front homojunction and rear heterojunction design of GaInP solar cells that are lattice matched to GaAs. Achieving record efficiencies in multijunction and spectrally split photovoltaics requires maximal performance in wide-E_g top junctions. GaInP is the prioritized material for top cells in multi-junction PV devices. Recent advances in single-junction wide-E_g GaInP photovoltaic devices have been driven by a rear-junction design, in which the p-n junction is placed near the back contact. This approach is the opposite of usual front-junction designs and is also counter-intuitive since carriers are now generated further away from the space charge region. In this chapter, we aim to understand the advantages and disadvantages of rearjunction designs from both numerical and analytic perspectives. First, we develop an analytical model for dark recombination current of two design configurations to address the discrepancy and use TCAD drift-diffusion solver to find out cutoff points for switching design configurations. This allows us to point out the tradeoffs between the two photovoltaic device configurations and to generically identify the parameters where the optimal configuration flips. This understanding helps both to explain the historical development of GaInP photovoltaic technology and to predict the most promising paths toward further improvements. Our general approach may also aid in designing other thin-film photovoltaic devices.

In chapter 4, the goal of this chapter is to identify the cause of performance degradation of vapor-liquid-solid deposition, a cost effective deposition technique employed in fabricating InP solar cells. Two hypotheses are investigated to explain the open-circuit voltage (V_{OC}) degradation observed in thin-film vapor-liquid-solid (TF-VLS) grown p-type InP photovoltaic cells: bandgap narrowing and local shunting. To explore these ideas, we develop a comprehensive modeling approach that com-

bines TCAD device modeling and Spice circuit model to explain the physical origin of degradation. First, a bandgap (E_g) narrowing effect is hypothesized, based on the surface inhomogeneity of VLS InP captured by the photoluminescence (PL) image. The PL data was used to estimate a spatially-resolved active V_{OC} across surface of the InP sample. Combining this data with the effective J_{SC} allowed an assessment of the I-V characteristics of individual unit cells. Next, an HSPICE diode compact model is utilized to reproduce the I-V characteristics of the whole sample. We find a good fit to the I-V performance of TF-VLS grown InP solar cell. Second, a local shunting effect was also considered as an alternative explanation of the V_{OC} degradation effect. Again, PL image data was used, and small local shunt resistance was added in arbitrary elementary unit cells to represent certain dark spots seen in the PL image and dictate the V_{OC} degradation occurred in the sample.

In chapter 5, the goal of this chapter is to assess the radiative cooling effect on concentrator photovoltaic devices. Radiative cooling, a unique and uncommon passive cooling method for devices operating outdoors, has recently been demonstrated to be effective for photovoltaic thermal management. Here, we investigate the effect of radiative cooling as a complement to existing passive cooling methods like convective cooling in a related system with much higher heat loads: a high-concentration photovoltaic (HCPV) system. We start by establishing a rigorous physics-based device model for Silicon concentrator photovoltaic devices under various temperatures and illumination intensities. We then couple convective, conductive and radiative heat transfer with the device model to self-consistently identify the equilibrium operational temperature of the CPV device. This framework provides platform for comparing different passive cooling techniques for PV devices operated under high heat load condition. A feasible radiative cooler design addressing the thermal management challenges here is proposed. It consists of low-iron soda-lime glass with a porous layer on top as an anti-reflection coating and a diamond layer as heat spreader. It is found that the proposed structure has strong mid-IR emittance as well as high solar transmission, allowing radiative cooling under direct sunlight and low loss in the

concentrated solar irradiance. A systematic simulation with realistic considerations is then performed. Compared with a conventional copper cooler, the lowest temperature reached by the proposed radiative cooler is 14 K lower. Furthermore, less area of the proposed cooler is needed to reach a standard target temperature (333.15 K) for steady-state operation under high concentrations for the crystalline silicon PV module. In order to compare the coolers quantitatively, a figure of merit – cooling power per weight - is introduced. At the target temperature, the proposed cooler is determined to have a cooling power per weight of 75 W/kg, around 3.7 times higher than that of the conventional copper cooler.

In chapter 6, the goal of this chapter is to optimize the *bifacial* design of interdigitated back contact silicon heterojunction solar cell via TCAD device modeling and develop a generalized formula that allows PV manufacturers to find the optimal rear side design of *bifacial* devices without performing complicated device simulations. One promising and highly feasible approach for increasing PV power generation is to add bifaciality to existing *monofacial* PV devices, allowing more output power from the additional reflection of sunlight from the ground (albedo α). For example, bifaciality can be added to Silicon Heterojunction (SHJ) solar cell with Interdigitated Back Contacts (IBC) by opening up the gaps between the back metal contacts, but the optimum gap (w) that maximizes power output is unknown. In this thesis we show that that the optimum gap ($w = 1-(1+\alpha)(\alpha(\alpha+c))^{-1/2}$) maximizes IBC-SHJ *bifacial* power output ($P \propto (1+\alpha)(1-2\sqrt{a/c})$), where c is the ratio of output power density to power loss due to shadowing and Joule heating. We then validate these results by applying a self-consistent finite-element TCAD device model in *bifacial* cells by adding rear side absorption and then comparing to experiments. For a typical $\alpha = 0.3$, we find that an optimized *bifacial* IBC SHJ cell will produce 17% more power output than state-of-the-art *monofacial* IBC SHJ cells. The results encourage development of *bifacial* IBC solar cells as a next generation PV technology.

In chapter 7, the goal of this chapter is to develop a generalized analytical formula to maximize the total power output of *bifacial* CIGS solar cells. Copper Indium

Gallium DiSelenide (CIGS) has been widely used as a thin-film absorber material in photovoltaics (PV). Process improvements have pushed efficiencies to 22.8%, approaching the Shockley-Queisser limit. For further improvement, *bifacial* PV, which couples light into the absorber from both sides, has emerged as a promising approach. We will modify the previously developed equation from chapter 6 based on TCAD device modeling result of CIGS solar cells. Here, we present a generalized analytic model to design the back contact pattern of *bifacial* CIGS solar cells for maximum power output at any albedo. At the global average albedo of 30%, we find that additional 2.4 mW/cm^2 can be obtained by switching from *monofacial* to *bifacial* PERC configuration. Our results can serve as potential design guidelines for manufacturers, and to forecast the potential of *bifacial* CIGS through levelized cost of electricity (LCOE) calculations.

In chapter 8, the goal of this chapter is to present a machine learning based approach for rapid screening and automated detection of PV cell performance. Rapid screening and detection of photovoltaic device performance is an important but complex quality control process for PV manufacturers. In this chapter, we propose an automated process enabled by machine learning model to quickly evaluate and classify PV performance. We start by utilizing TCAD device modeling framework to generate training, testing and validation set. We then will invoke a neural network autoencoder to compress J-V characteristics and generate cluster patterns. The framework will be validated by comparing the reconstructed J-V curves to input J-Vs. This machine learning model, implemented by a Neural Network Autoencoder trained with J-V characteristics generated from TCAD solar simulator under various opto-electric input parameters, is validated by reconstructing input J-V characteristics through mirror Neural Network Decoder. Classification of the simulated and experimental J-V characteristics is achieved by plotting the 2-D encoded data points clustered by K-means Algorithm. The model not only benefits the manufacturers by helping to establish a standard operating procedure for the rapid screening and detection

of manufactured cell performance, but also provides insights in connecting physical input parameters to statistically classified J-V characteristics.

Finally, we will summarize the key takeaways from the thesis and forecast the future direction of PV industries in chapter 9.

2. WIDE BANDGAP GALLIUM INDIUM PHOSPHIDE SOLAR CELLS

2.1 Introduction

For the past decades, photovoltaic systems have been designed and fabricated to reach ultra-high efficiencies well above the single-junction Shockley-Queisser limit [7], requiring wide bandgap solar cells. For example, if multiple PV cells are stacked together in series, a wide bandgap cell ($>$ 2.0 eV) is needed to achieve the most efficient conversion of high energy photons [8]. Similarly, spectral splitting requires a wide bandgap cell for maximally effective conversion [9]. Photovoltaics at elevated temperatures also suffer from less degradation with a wide bandgap cell [10, 11]. Finally, for near-surface underwater PV applications of recent interest, there is a need for wide bandgap cells for efficient collection of the high energy photons that can penetrate water [12].

The state-of-the-art solution for accessing 2.1-2.2 eV bandgap range, while retaining a direct bandgap, is to increase the Al content in quaternary $(Al_xGa_{1-x})_{0.51}In_{0.49}P$, grown lattice-matched to GaAs [13]. However, it has been found that the oxygen incorporation associated with increased Al content decreases solar cell efficiency [14]. Further, a GaAs substrate is not transparent to light below the bandgap of the active junction. Another wide bandgap option is GaP, with an indirect bandgap of 2.26 eV. GaP should be a natural choice, considering the availability of high-quality bulk substrates and the commercial maturity of GaP-based light emitting diodes. However, GaP solar cells suffer from relatively poor absorption and current collection,

[0]The content of this chapter is primarily taken from a published conference proceeding: Y. Sun, K. H. Montgomery, X. Wang, S. Tomasulo, M. L. Lee, and P. Bermel, "Modeling Wide Bandgap GaInP Photovoltaic Cells For Conversion Efficiencies Up to 16.5%" *IEEE 42nd Photovoltaic Specialist Conference (PVSC)*, New Orleans, LA, (2015): pp. 1-6.

with internal quantum efficiency (IQE) values typically peaking at 50% [15, 16]; as a result, the highest efficiency for anti- reflection (AR)-coated cells in the literature is 2.9% [17].

As an alternative, direct bandgap $Ga_{1-y}In_yP$ ($0.18 < y < 0.30$) solar cells can be grown by molecular beam epitaxy (MBE) using metamorphic (MM) buffers on GaAs or GaP substrates. The direct bandgap enables stronger absorption and higher short-circuit current density, J_{SC}, than has been conventionally possible in GaP solar cells. However, the challenge in growing $Ga_{1-y}In_yP$ ($0.18 < y < 0.30$) cells is that they are lattice-mismatched to conventional substrates, as illustrated in Fig. 2.1:

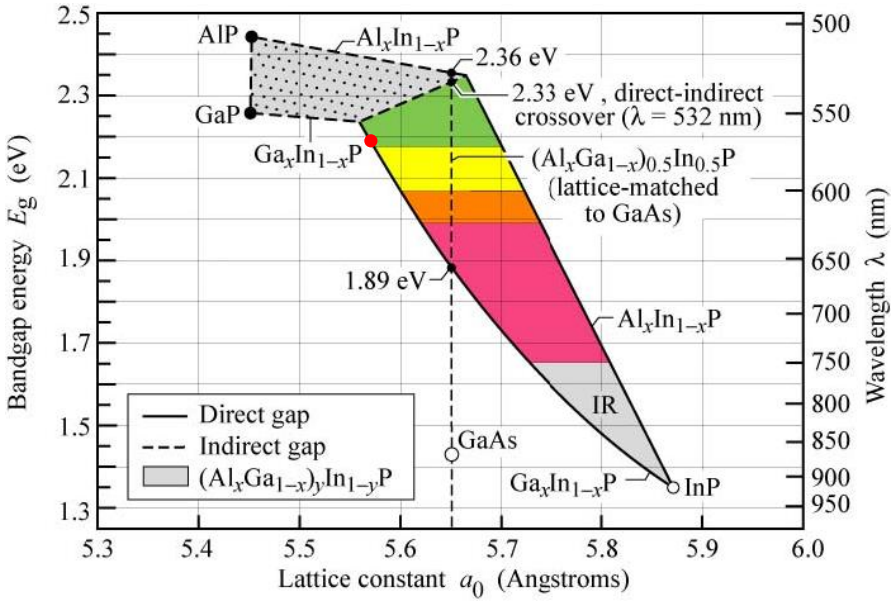

Fig. 2.1.: Bandgap energy and corresponding wavelength versus lattice constant of $(Al_xGa_{1-x})_yIn_{1-y}P$ at 300 K (adapted from [18]). Our study focuses on $Ga_{0.75}In_{0.25}P$ ($E_g = 2.19$ eV) (red dot)

The red dot highlights the bandgap energy and lattice constant of $Ga_{0.75}In_{0.25}P$ modeled in this work. To grow lattice-mismatched $Ga_{1-y}In_yP$ films with low threading dislocation densities (TDDs) and long minority carrier lifetimes, intermediate $GaAs_xP_{1-x}$ graded buffers can be used to engineer the lattice constant from that of

the GaP substrate to that of the wide bandgap $Ga_{1-y}In_yP$ solar cell. Prior work on these devices has shown an open circuit voltage, V_{OC}, of 1.42 V, J_{SC} of 3.11 mA/cm^2 (without anti-reflection coating), and a fill factor (FF) of 0.71, yielding a cell efficiency of 3.13% [19].

2.2 Modeling of Spectral Absorption Profile

Modeling the performance of such a cell design first requires an accurate model of material absorption. Since no literature data is currently available, this can be extrapolated from related III-V compounds. Fig. 2.1 also illustrates the bandgap energy transition from InP to GaP, where the black solid line shows direct bandgap transitions, and the black dashed line describes the indirect bandgap transition. The absorption data of $Ga_{0.5}In_{0.5}P$ and InP were used to extrapolate the absorption data of $Ga_{0.75}In_{0.25}P$. In order to achieve this, the band edges of the three materials mentioned above were identified. The extrapolation method employed was to horizontally shift the absorption curves of $Ga_{0.5}In_{0.5}P$ and InP towards shorter wavelengths, based on the band edge ratios. The extrapolated absorption curve of $Ga_{0.75}In_{0.25}P$ is shown in Fig. 2.2. Its implied band edge wavelength is 566 nm, which directly matches its bandgap energy of 2.19 eV. This should be a reliable way to generate the absorption data of $Ga_{0.75}In_{0.25}P$, as all materials being considered in this extrapolation are direct bandgap materials.

The simulation tool being used to model the wide-E_g GaInP cell is "A Device Emulation Program and Tool" (ADEPT) on nanoHUB.org [20]. This tool solves Poisson's equation with hole and electron continuity equations in 1 spatial dimension in compositionally non-uniform semiconductors. It was originally written to model solar cells fabricated from a wide variety of materials including a-Si, CIGS, CdTe, etc [20].

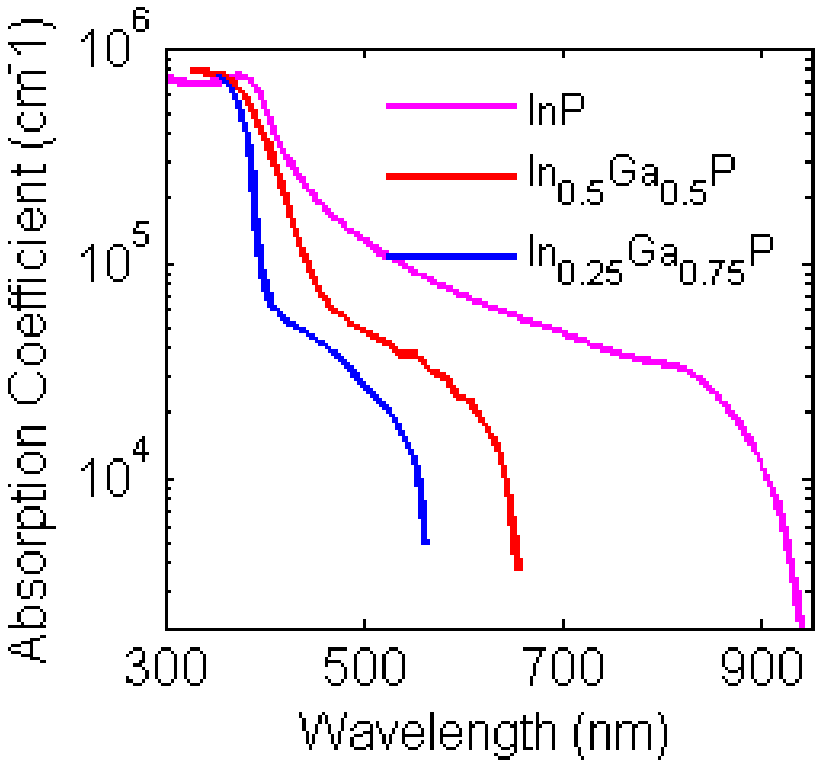

Fig. 2.2.: Extrapolated absorption curve of $Ga_{0.75}In_{0.25}P$, calculated from literature data for the absorption of InP and $Ga_{0.5}In_{0.5}P$.

2.3 Results & Discussion

The external quantum efficiency (EQE) was calculated for a cell structure consisting of a 20 nm n-AlInP window layer, 100 nm n-$Ga_{0.75}In_{0.25}P$ emitter ($N_D = 10^{18}/cm^3$), and 2 µm of p-$Ga_{0.75}In_{0.25}P$ ($N_A = 3 \times 10^{17}/cm^3$), as shown in Fig. 2.3.

Due to the fact that the window layer of this cell is made of AlInP, a heterostructure was formed at the interface between the window layer and the GaInP emitter, and the density of defects is not negligible at the interface. Thus, interface recombination also contributes to the degradation of the cell performance. The simulated EQE for various levels of recombination compared to the experimental EQE is shown in Fig. 2.4. The ideal case with high bulk lifetime (1 ms) and low window-emitter recombination (< 1 cm/s) predicts exceedingly high EQE values. Degrading

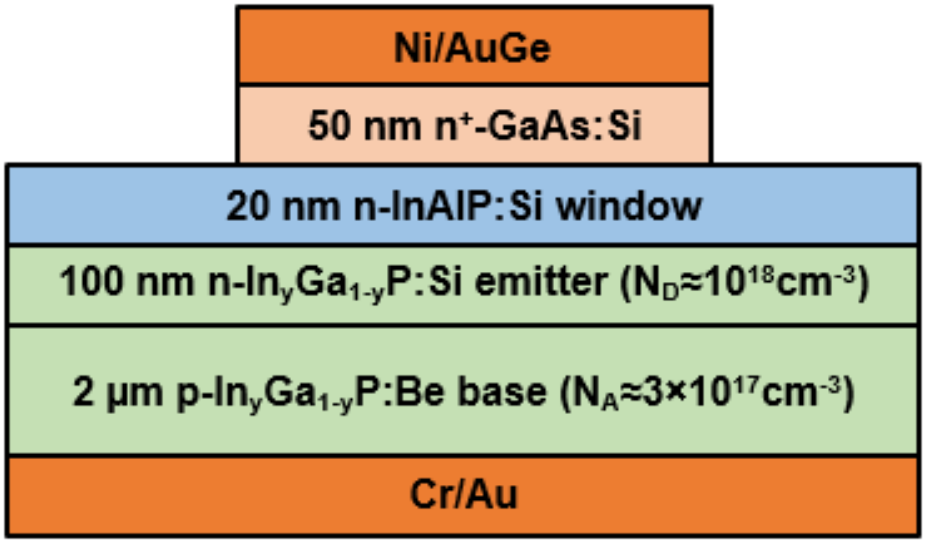

Fig. 2.3.: Cross-sectional schematic of $Ga_{1-y}In_yP$ cell structure modeled in this work (adapted from [19]).

just one of these values alone is also insufficient to account for the observed EQE. Instead, it was found that both the emitter and base minority carrier lifetime (τ_e and τ_b) must be reduced to 0.12 ns and 0.1 ns respectively, which shows some agreement to the bulk minority carrier lifetime characterized and reported in the literature [21]. At the same time, the window-emitter interface recombination velocity must increase to 9×10^5 cm/s to match the measured EQE curve (from [19]). This allows the J_{SC} from the simulation to agree closely with the J_{SC} reported in the experiment.

In order to fully capture the I-V characteristics of the cell, J_{SC} and V_{OC} were calculated as follows. First, eq. 2.1 was used to characterize the shape of the simulated I-V curve:

$$J_{SC} = \int_0^\infty d\lambda [\frac{e\lambda}{hc} \frac{dI}{d\lambda} EQE(\lambda)] \tag{2.1}$$

in which e is the unit charge; h is planck constant; λ is wavelength; c is the speed of light; and I is spectral intensity of AM 1.5G solar spectrum. J_{SC} is given as the product of the AM 1.5G solar spectrum and the EQE integrated over all wavelengths. The calculated J_{SC} is 3.16 mA/cm^2, which is slightly higher than the measured J_{SC}.

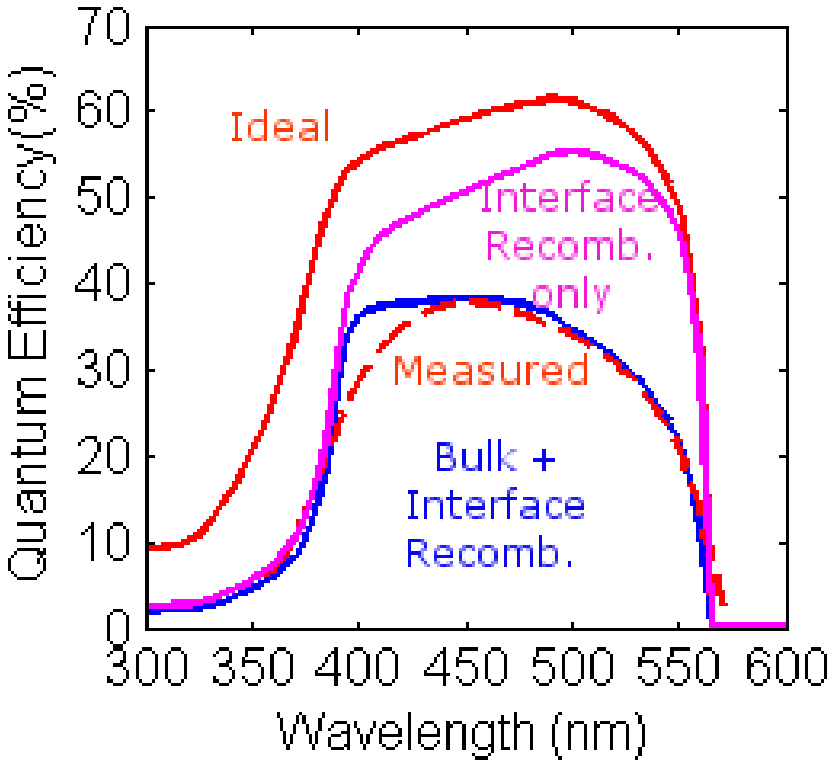

Fig. 2.4.: External quantum efficiency (EQE) versus wavelength from 300 nm to 600 nm. Experimental data (dashed red line) is from [19]. The model fit accounts for ideal (red), interface recombination only (green) and both interface and bulk recombination effects (blue).

This difference can be attributed to small deviations between simulated and measured EQE around 400 nm shown in Fig. 4. The disagreement of EQE at this wavelength range is mainly due to imperfections in the wide E_g material absorption modeling, which could be improved by considering a piecewise mathematical model of the dispersion of the imaginary part of refractive index presented in literature [22]. The open circuit voltage is obtained directly from ADEPT. The diode equation used to model the experimental data, which incorporates ideality factor, series and shunt resistance is given as Equation. 2.2:

$$J(V) = J_{SC} - J_o \exp\left[\frac{e(V + JR_s) - E_g}{nkT}\right] - \frac{V + JR_s}{R_{sh}} \tag{2.2}$$

in which J_o is the reverse saturation current; n is the ideality factor; T is the temperature; R_S and R_{sh} are series and shunt resistance respectively. The calculated ideality factor is 1.61. Finally, reasonable values of the series and shunt resistance ($20\ m\Omega - cm^2$ and $2.7\ k\Omega - cm^2$, respectively) were added to achieve the closest possible fit to experiment, as shown in Fig. 2.5, an excellent match was achieved, with an average difference between the two curves of 0.1%.

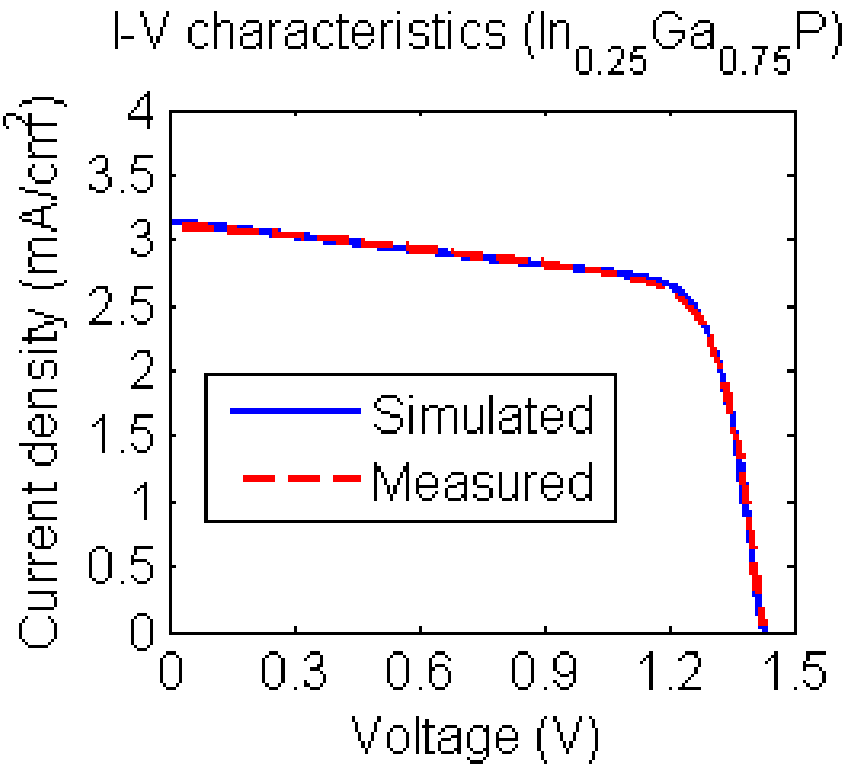

Fig. 2.5.: A comparison between measured and simulated I-V characteristics of the single junction $Ga_{0.75}In_{0.25}P$ solar cell. Very strong agreement in V_{OC} and fill factor and J_{SC} is observed, derived from the EQE in Fig. 2.2

2.4 Improvement of Cell Structure

After reproducing the measured data successfully, we consider strategies to optimize cell efficiency. Based on the extrapolated absorption curve of wide-E_g GaInP in

Fig. 2.2, it can be concluded that most photons are absorbed near the front surface. Thus, the carrier collection efficiency at the contact is very sensitive to the doping level and thickness of the emitter layer. Theoretically, low doping in the emitter leads to high minority carrier lifetimes and long diffusion lengths, which could increase the possibility of carriers reaching at the contact before recombining. However, it could also hurt the built-in potential at the junction to reduce the V_{OC}, offsetting the improvement in J_{SC}. Therefore, it is worth exploring this tradeoff to help maximize the cell efficiency. There is also a similar tradeoff in terms of emitter thickness, as it determines the location of the depletion region where a strong electric field is formed to help dissociate electron-hole pairs and sweep electrons and holes towards the metallic contact. Carrier collection is more efficient as the emitter thins out to keep the space charge region close to the surface of the cell where the majority of electron-hole pairs are generated. However, it is difficult to fabricate ultra-thin heavily doped layers with typical fabrication techniques. The correlation of cell efficiency with emitter thickness and emitter doping is depicted in Fig. 2.6. Here, the base doping and thickness are fixed to experimental values ($N_A = 3 \times 10^{17}/cm^3$; 2 μm) to create this contour plot. The carrier mobility was assumed to be constant with the variation of doping concentration. The fill factor is corrected to include the increased series resistance and reduced fill factor associated with low doping levels. As can be seen from the plot, when $N_D = 3 \times 10^{14}/cm^3$ and emitter thickness is 0.6 μm, the cell efficiency reaches 5.16%, which is higher than measured 3.13%. These results differ from previous work because of challenges in achieving the required doping profile in experiments. Although it may be difficult to fabricate lightly-doped doped layers with typical methods, improvements in both V_{OC} and J_{SC} have been identified with reduced emitter doping in the literature [23, 24]. As an alternative method for improving cell efficiency, we may consider adding an intrinsic GaInP layer between the emitter and base layer to form an n-i-p structure [25]. Despite the fact that there is a strong electric field at the depletion region of the modeled cell, the depletion width is only 30 nm. Adding an intrinsic layer could greatly expand the space charge region to

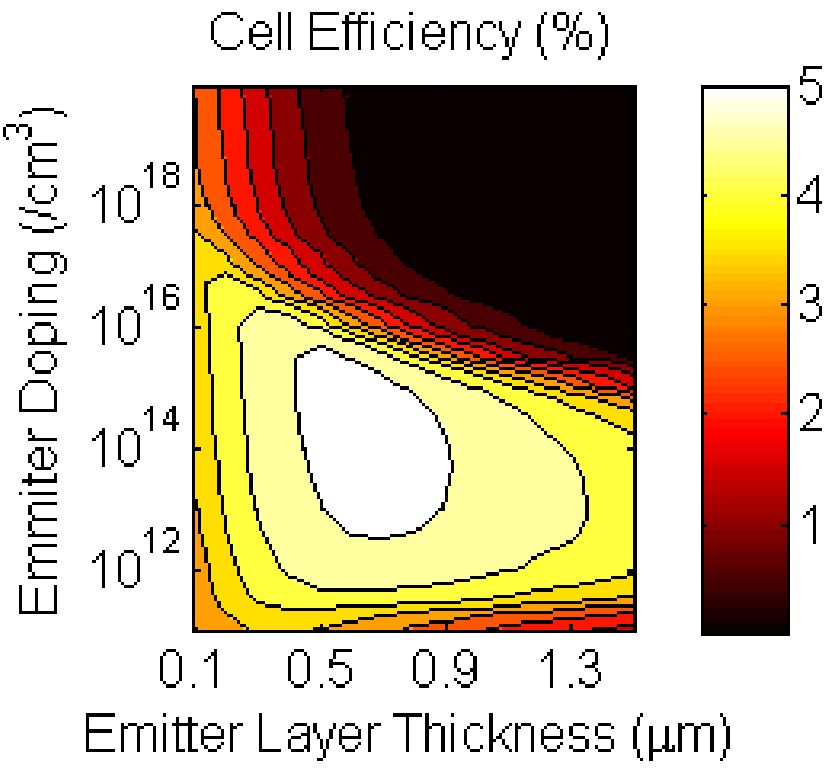

Fig. 2.6.: A contour plot optimizing the cell efficiency as a function of emitter layer parameters, specifically doping and thickness.

improve the collection of carriers excited by the absorbed photons. It is expected that the carrier collection efficiency and J_{SC} will both be improved with higher quantum efficiency over the effective wavelength range after adding the intrinsic layer. With emitter doping and thickness fixed at the experimental values ($N_D = 1 \times 10^{18}/cm^3$; 0.1 µm), cell efficiency as a function of intrinsic layer thickness and base doping is plotted and illustrated in Fig. 2.7. The cell efficiency is more sensitive to the intrinsic layer thickness than the base doping, within the region considered. With base doping constrained to be smaller than emitter doping, the highest efficiency of 6.3% is obtained at $N_A = 9 \times 10^{17}/cm^3$ and the intrinsic layer thickness t_i of 2 µm, well above the original 3.13%. Efficiency was doubled by greatly extending the space charge region to collect a broader range of generated carriers at different wavelengths. Using these results, the typical external quantum efficiency is illustrated and compared

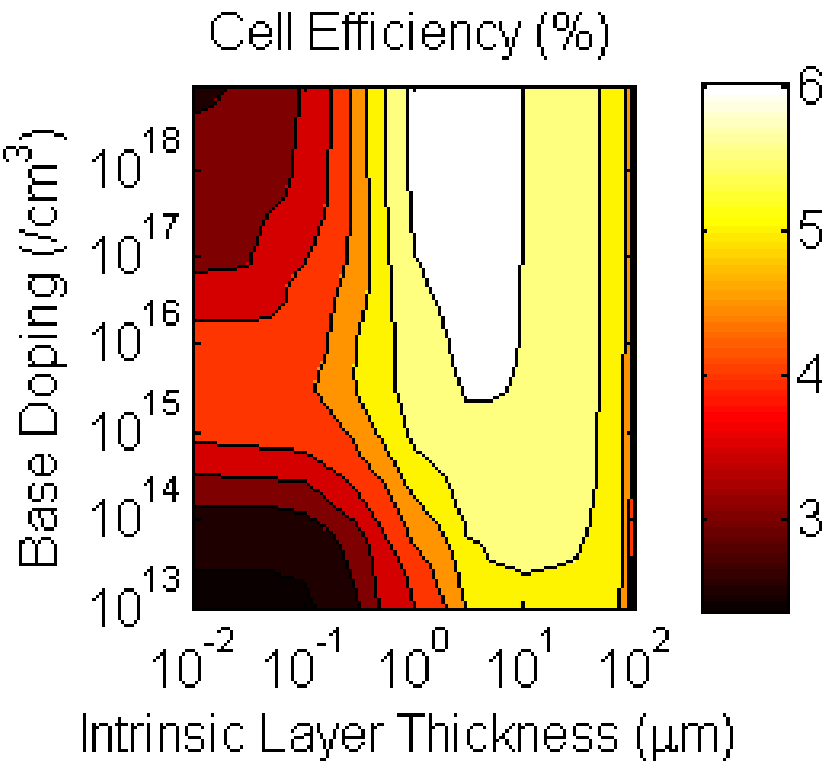

Fig. 2.7.: A contour plot optimizing the cell efficiency as a function of the intrinsic layer thickness and base doping. The highest efficiency of 6.3% is for $N_A = 9 \times 10^{17}/cm^3$ and $t_i = 2$ µm.

to our prior model result shown in Fig. 2.8. As expected, the quantum efficiency of photons with energy near the band edge increases significantly from the previous design. If this structure (shown in Fig. 2.9) were to be employed, the new J_{SC} would be 5.44 mA/cm^2, a 70% improvement over the previous design without requiring any fundamental changes in the growth process. Ion implantation may be employed to sandwich an intrinsic layer between two heavily doped layers in experiment.

2.5 Conclusion

In this work, we were able to precisely reproduce the EQE, J_{SC} and V_{OC} associated with a wide bandgap GaInP (E_g = 2.19 eV) photovoltaics cell and found that the

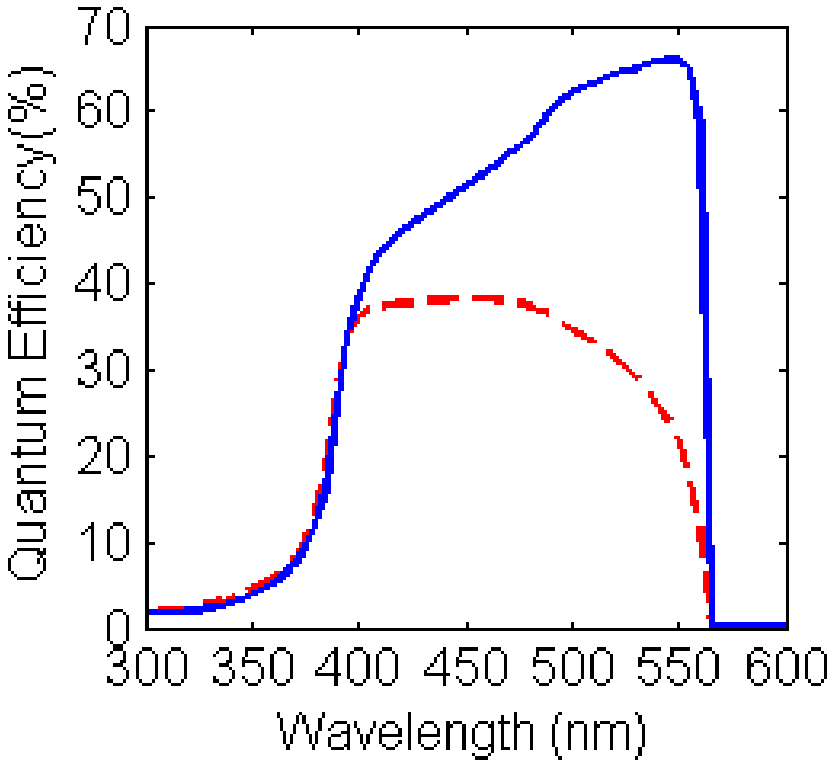

Fig. 2.8.: EQE versus wavelength from 300 nm to 600 nm before and after optimization. Modeled data (dashed red line) is the best fit curve from measured EQE [19]. The EQE of proposed n-i-p structure with intrinsic layer thickness of 2 μm accounts for all the loss mechanisms found in experiment (blue line).

emitter and base minority carrier lifetime (τ_e and τ_b) are in the order of 0.1 ns, while the window-emitter interface recombination velocity is approximately 9×10^5 cm/s. A potential improvement to the cell structure, consisting of adding an intrinsic layer within the junction to form an n-i-p structure is proposed. With intrinsic layer thickness of 2 μm, and base doping of $9 \times 10^{17}/\text{cm}^3$, this n-i-p single junction wide-E_g GaInP solar cell could achieve an efficiency of 6.3%, a 2× improvement over the n-p design. In future work, we will consider a broader range of GaInP compositions and some intermediate milestones for reduced recombination, as well as their projected benefits. This will help define a path forward to improve the performance much closer to its theoretical limits (approximately 16.5%) [26].

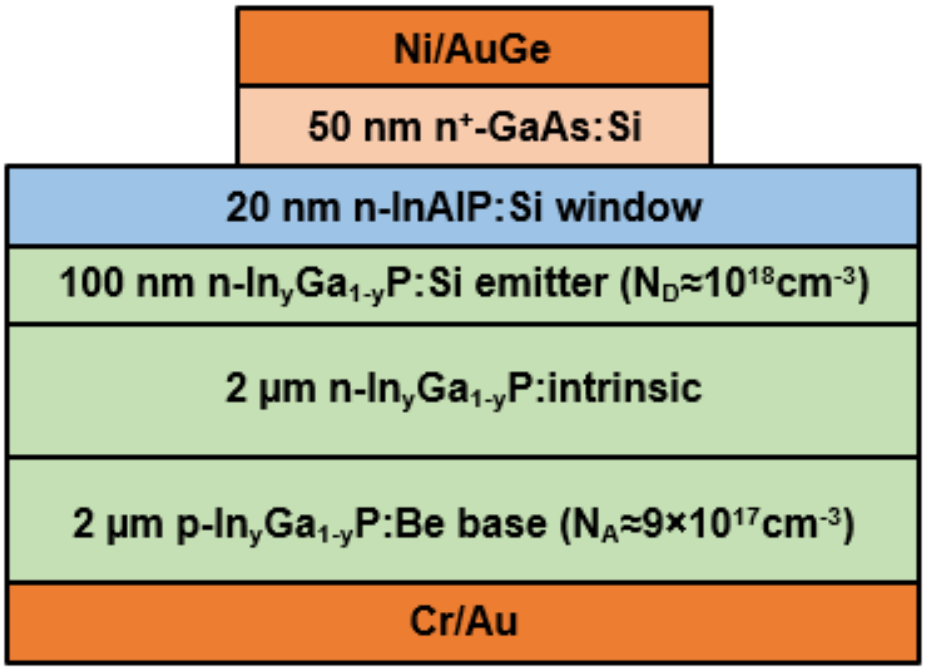

Fig. 2.9.: Cross-sectional schematic of the improved $Ga_{1-y}In_yP$ n-i-p cell structure proposed in this work.

3. NUMERICAL AND ANALYTICAL MODELING OF FRONT- AND REAR-JUNCTION GALLIUM INDIUM PHOSPHIDE PHOTOVOLTAIC DEVICES

3.1 Introduction

Since the invention of the solar cell efficiency tables in the early 1990s [27], the drive to achieve the highest possible photovoltaic cell efficiencies has often involved multijunction III-V compound semiconductor materials. They have been used in wide range of applications, including but not limited to space-based photovoltaics, concentrating photovoltaics, and thermophotovoltaics [28–32].

Within the class of III-V semiconductors, the ternary alloy $Ga_{0.5}In_{0.5}P$ (GaInP for short) with wide-E_g (~ 1.8 eV) and lattice match to Gallium Arsenide (GaAs) has long been a leading candidate for the top cell of multi-junction photovoltaics aiming for world-record efficiencies [33]. Thus, it is worthwhile to explore the optimal design of single-junction GaInP in multi-junction photovoltaics to push the device efficiency towards the Shockley-Queisser limit. The original record-efficiency GaInP solar cell was demonstrated by Takamoto et al. [34] decades ago. It employed a front-homojunction (FHJ) design for a reported efficiency of 17.4%. In 2013, Geisz et al. [35] proposed a counter-intuitive rear-heterojunction (RHJ) design, namely placing the p-n junction near back contact to boost the device efficiency up to 20.8%. The current record efficiency of single-junction GaInP solar cell tested under AM1.5G solar spectrum also utilizes a rear-heterojunction design. Manufactured by LG electronics [36], it adds an Al-graded $Al_xGa_{1-x}InP$ layer between the emitter and base to raise the efficiency

[0]The content of this chapter is primarily taken from a published paper: Y. Sun, and A. Perna and P. Bermel, "Comparing Front- and Rear-Junction GaInP Photovoltaic Devices Through Detailed Numerical and Analytical Modeling," *IEEE Journal of Photovoltaics*, vol. 9, no. 2, pp. 437-445, March 2019

from the previous record by an absolute 0.6% to 21.4%. Though this record efficiency device's fabrication details have not been explicitly revealed, it has been confirmed in the group's conference proceeding publication that an emitter heterojunction with an epitaxial lift-off process is employed in manufacturing. Although it has been claimed that the RHJ design can suppress the Sah-Noyce-Shockley (SNS) recombination [37] or equivalently the Shockley-Read-Hall (SRH) recombination in the space charge region (SCR) so as to boost cell efficiency, there is a lack of detailed explanations to quantitatively demonstrate the advantage of employing RHJ over FHJ. Additionally, the tradeoffs between traditional front-homojunction device and rear-heterojunction device have not been addressed in a more general framework in prior work. It is important to investigate fundamental origins of efficiency enhancement switching from FHJ to RHJ.

In this chapter, we investigate the fundamental origins of the efficiency boost for single-junction GaInP solar cells by setting up a simple, physics-based analytical model of the diode injection current for both FHJ and RHJ. Our model is validated with thorough benchmark against experimental performance data. We then numerically explore the tradeoff between the two junction configurations through TCAD *Sentaurus* (Synopsys) [38], a coupled Poisson & drift-diffusion solver, by varying key device parameters, such as the interface recombination velocity and the SRH minority carrier lifetime.

The rest of this chapter is organized as follows. In section 3.2, we discuss the layer-by-layer structure fabrication for both GaInP FHJs and RHJs. This is followed by the development of a simple analytic model of diode injection current for GaInP FHJ and RHJ photovoltaics in section 3.3, to highlight the most important underlying physical phenomena affecting the design configuration. Then in section 3.4, we explore and identify the tradeoff between FHJ and RHJ by assessing the key metrics of the photovoltaic device performance under various circumstances through rigorous numerical modeling in *Sentaurus* TCAD. Potential efficiency improvements from ex-

amining current will be discussed in Section 3.5. Finally, we present our conclusions and future work in Section 3.6.

3.2 Structure Details

Fabrication and assessment of the performance of wide-E_g GaInP FHJ and RHJ solar cells were previously performed at NREL and summarized in [35]. The FHJ consists of a thin AlInP window layer on top (thickness not given, but typically 20 nm) [39], covered by a MgF_2/ZnS anti-reflection coating (ARC) layer, a 100 nm thin highly n-doped GaInP emitter layer, a 1-µm-thick lightly p-doped GaInP base layer, backed by a 100-nm-thick heavily p-doped $Al_{0.25}Ga_{0.25}In_{0.5}P$ (AlGaInP) back-surface field (BSF) layer, as shown in Fig. 3.1(a) The RHJ is comprised of a 20-nm-thick AlInP window layer on top, coated by an identical ARC, a 1-µm-thick n-doped GaInP emitter layer, and finally a 100-nm-thick heavily p-doped AlGaInP BSF layer, as shown in Fig. 3.1(b).

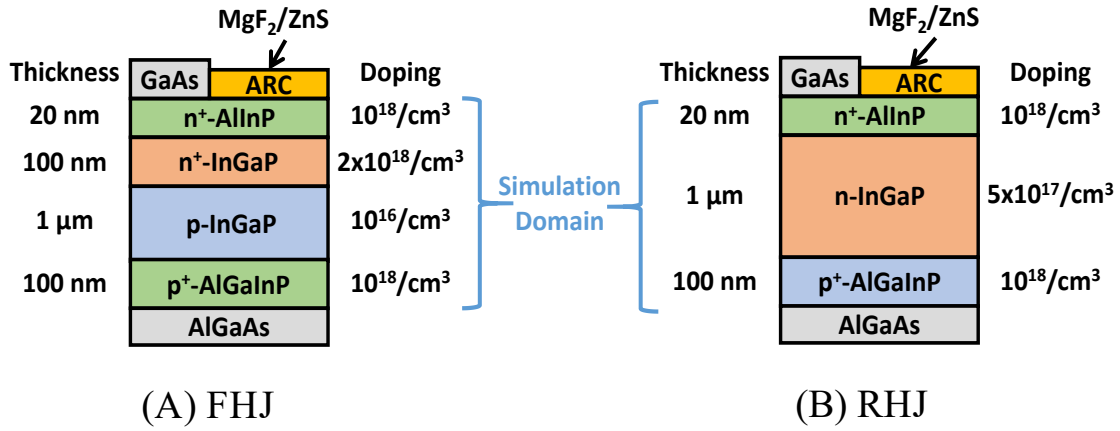

Fig. 3.1.: Schematics of cross-sectional view of two different design configuration of $Ga_{0.5}In_{0.5}P$ solar cells with doping level and layer thickness specified: (A) Front Homo-junction, (B) Rear Hetero-junction. AlGaAs and GaAs are front and back contacts, being excluded in numerical simulation.

Using a RHJ design for GaInP may seem counter-intuitive. Solar photons incident from above with the correct range of energies will generate electron-hole pairs predominantly near the top surface of the GaInP solar cells. The energy band diagrams (EBDs) of FHJ and RHJ cells under the short circuit condition are plotted in Fig. 3.2. To facilitate electron-hole separation, p-n junctions are usually placed at the front side of solar cell so that the strong electric field created can enhance charge separation. The RHJ lacks an electric field at the front to facilitate charge separation, and it also removes the moderately doped p-type base layer, using a heavily doped BSF layer as the base instead. To fully understand the conditions in which

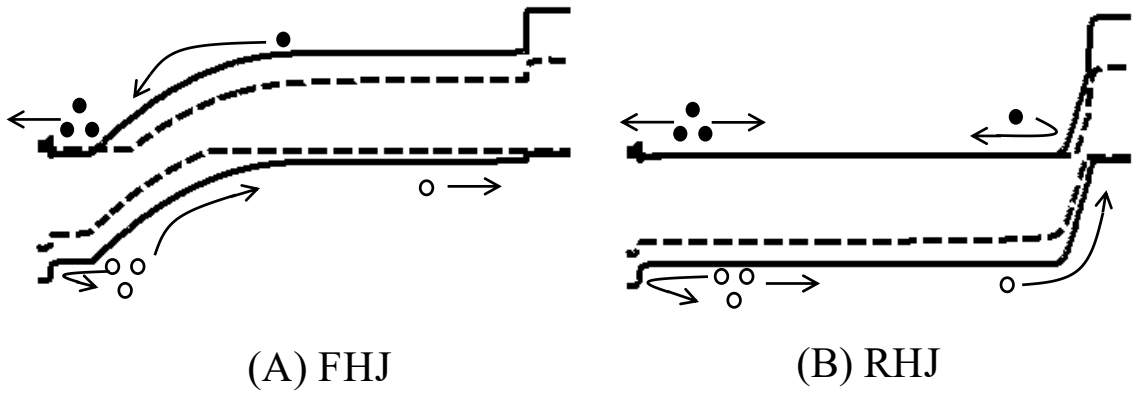

Fig. 3.2.: Schematic energy band diagrams under short circuit conditions, with solar illumination input from left to right, and sketched electrons and holes transport paths for the following structures: (A) Front Homo-junction. (B) Rear Hetero-junction.

a RHJ design would be advantageous compared to the FHJ, an analytical model of the diode injection current for both FHJ and RHJ photovoltaic cells is derived in the next section.

3.3 Analytical Model

3.3.1 Assumptions for Modeling

Superposition Principle. The terminal current of a photovoltaic device J_{tot} depends on both the carrier generation rate (G) and applied bias (V), and is given by [40]:

$$J_{tot}(G,V) = J_{photo}(G,V) - J_{inj}(G,V), \tag{3.1}$$

where J_{photo} and J_{inj} are photo-generated current and diode injection current respectively, accounting for non-idealities such as the voltage-dependent photocurrent and generation-dependent diode injection current commonly seen in thin-film chalcogenide solar cells [41–44]. The superposition principle allows direct separation of J_{tot} under illumination and in the dark, assuming that J_{photo} is voltage-independent and J_{inj} is independent of carrier generation. Thus, the general form of J_{tot} can be rewritten as follows:

$$J_{tot}(G,V) = J_{photo}(G) - J_{inj}(V) = J_{SC} - J_{dark}(V), \tag{3.2}$$

where J_{photo} only depends on carrier generation G and becomes constant short circuit current J_{SC} under given illumination condition (i.e. the AM 1.5G solar spectrum). The superposition principle often holds for high efficient, less defective solar absorbers (e.g., c-Si, GaAs, etc.) [41, 45]. The applicability of the superposition principle for both FHJ and RHJ is validated by subtracting the dark IV from the light IV. If the resulted current density remains constant from $V = 0$ to $V = V_{OC}$, one can claim that superposition holds for the device under consideration.

Radiative Recombination Coefficient B. Photon recycling is an important aspect to precisely model the performance of III-V compounds based PV devices. For various solar cell systems, the external radiative efficiency (ERE) [46–48] was introduced to assess the gap between the thermodynamic limit and practical cell performance. ERE is a figure of merit defined as the fraction of the total dark current

recombination in the device that results in radiative emission from the device [48]. To precisely predict the radiative recombination that occurs inside the solar cell, one must include the impact that photon recycling has on radiative recombination. The intrinsic radiative recombination coefficient B is a material property that is defined by the Roosbroeck-Shockley relation as follows [49]:

$$B = \frac{8\pi n^2}{n_i^2 c^2} \int_0^\infty \frac{\lambda^2 \alpha(\lambda)}{e^{hc/\lambda kT} - 1} d\lambda \tag{3.3}$$

where $\alpha(\lambda)$ is the optical absorption coefficient as a function of wavelength λ, n is the refractive index, n_i is the intrinsic carrier concentration of the absorber, k is the Boltzmann constant, c is the speed of light, and T denotes the device temperature. When one accounts for photon recycling, the number of photons reemitted from the device is no longer exclusively associated with intrinsic radiative recombination. This relationship can be explained by Fig. 3.3, which shows that that extrinsic radiative recombination can be significantly suppressed by photon recycling. More specifically,

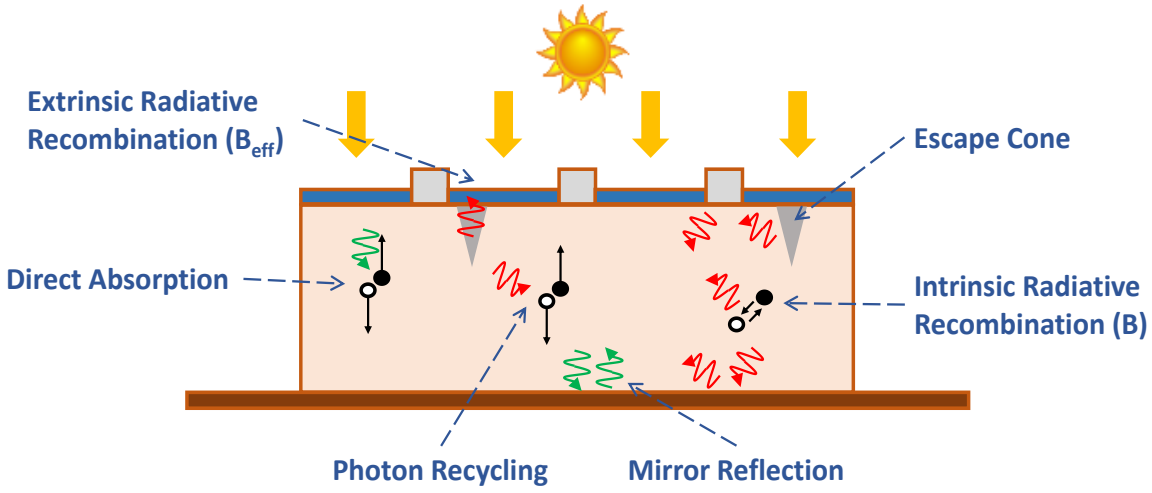

Fig. 3.3.: Schematics illustrating the relationship between intrinsic radiative recombination and extrinsic radiative recombination through photon recycling.

the photon recycling process operates as follows. After sunlight penetrates the cell and is absorbed, the associated photons can generate electron hole pairs that will either

generate electricity by being collected by contacts, dissipate as heat loss through non-radiative recombination, or radiatively recombine to generate more photons. These photons can subsequently be reabsorbed and reemitted within the cell until the photons escape at the front through the escape cone [45], or are parasitically absorbed by the substrate. This initial sequence is called photon recycling. In the end, a fraction of radiative recombined photons are absorbed during the photon recycling process and converted into electricity. Thus, photon recycling can be treated as a process that suppresses the total radiative recombination coming out of the device, allowing for replacement of the radiative recombination coefficient B by an effective radiative recombination coefficient B_{eff} corrected by photon recycling. The ratio Φ_r between B and B_{eff} is called the photon recycling factor or Asbeck coefficient [50]; and is defined as: $\Phi_r = B/B_{eff}$. Unlike B, B_{eff} is not only dependent of absorber material itself, but also it is subject to the solar cell structure including absorber layer thickness, front and back reflectivity etc. To fully address the physics of photon recycling in the modeling, one has to consider a rigorous self-consistent photon recycling module calculated by ray-tracing coupled to a drift-diffusion device simulation [45]. In our work, photon recycling is not modeled explicitly, but instead it is incorporated by defining a B_{eff}, which can be estimated from the radiative $J_{o,rad}$ given in literature [35], and is later validated by comparing to B calculated by Eq. 3.3. Since we are not modifying the optical property of structure (i.e. front & back reflectivity, layer thickness etc.) in the numerical model for exploring tradeoffs between FHJ and RHJ, defining a B_{eff} to account for photon recycling effect is sufficient to address the questions raised in this chapter.

3.3.2 Methodology

Since the superposition principle holds for both FHJ and RHJ GaInP solar cells, we can develop an analytic model that can predict the diode injection current J_{dark} to explain device performance. Although a well-developed five-parameter compact

model for solar cells may anticipate the I-V performance for both FHJ and RHJ, the underlying physics for the two configurations is beyond its scope. Thus, a simple physics based analytic model is more of necessity to help understand the superiority of RHJ design over FHJ design. The diode injection current can be treated as the sum of the radiative recombination current and the non-radiative recombination current, in which the latter term can be split into two parts: the diffusion-limited current that accounts for the SRH recombination in the quasi-neutral region and the SCR recombination current that quantifies the SRH recombination in the space charge region (SNS recombination). Hence, the diode injection current is expressed in Eq. 3.4 [51]:

$$J_{inj}(V) = J_{diff}(V) + J_{rad}(V) + J_{SCR}(V), \tag{3.4}$$

To break down each term for the FHJ and RHJ structures, we first simplify by removing their window layers and contacts. The details of the resulting structure are illustrated in Fig. 3.4. For both configurations, x_n and x_p are defined as the SCR region width along the donor and acceptor doped sides respectively; W_n and W_p represent the total layer width on the donor and acceptor doped side respectively, τ_n and τ_p are SRH minority electron and hole lifetimes respectively.

Front Homo-Junction. The FHJ structure is composed of two layers: the 0.1 μm thick heavily n-doped GaInP emitter and the 1 μm thick lightly p-doped GaInP base. The front surface recombination velocity S_f is defined to account for the interface recombination loss between AlInP/GaInP. Likewise, the heavily p-doped BSF layer at the back is also omitted, an effective back surface recombination velocity S_b is specified to monitor the rear surface recombination loss between GaInP/AlGaInP. Note that both S_f and S_b should be less than 10^7 cm/s, since two boundaries are passivated hetero-interfaces and differ from pure Ohmic contacts. The first term of Eq. 3.4, $J_{diff}(V)$, can be derived from the electron and hole minority carrier diffusion (MCDE) equation:

$$\frac{\partial \Delta n_p}{\partial t} = D_n \frac{\partial^2 \Delta n_p}{\partial^2 x^2} - \frac{\Delta n_p}{\tau_n} + G_L; \tag{3.5}$$

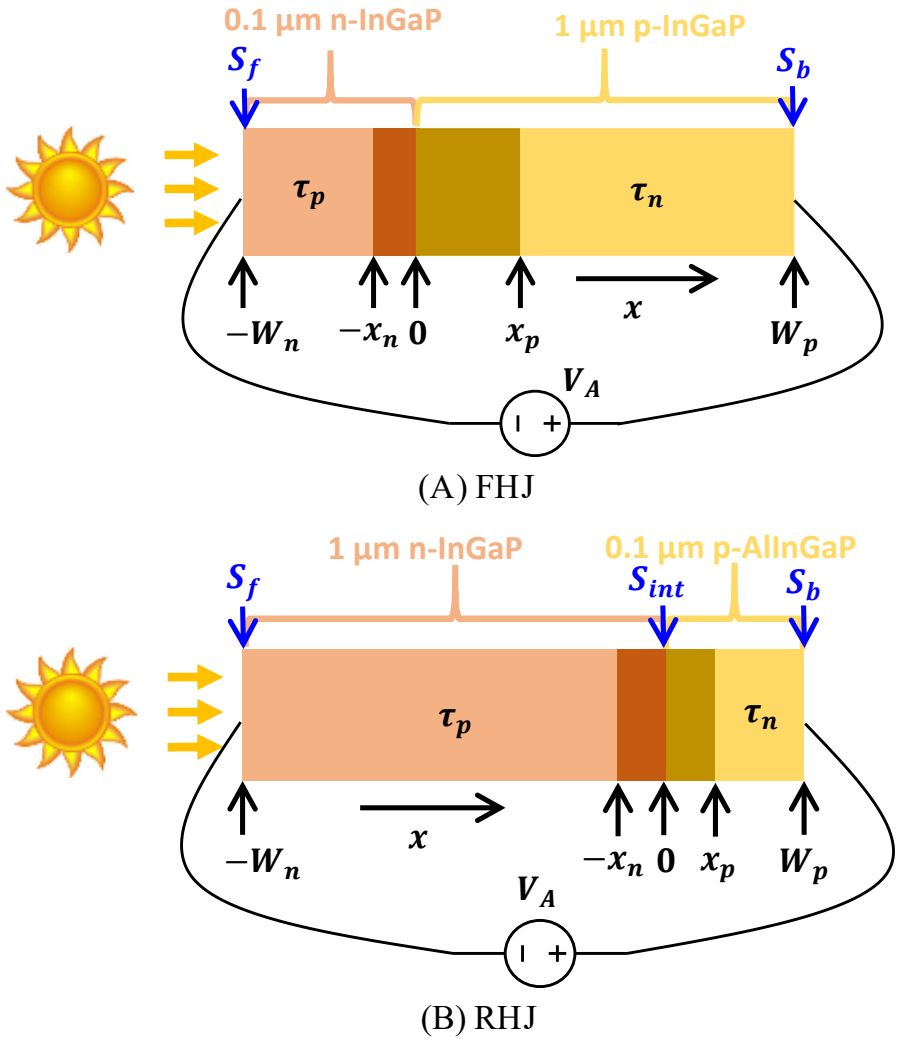

Fig. 3.4.: Schematics of the simplified $Ga_{0.5}In_{0.5}P$ p-n junction considered in the analytic model. (A) Front Homo-Junction (B) Rear Hetero-Junction.

$$\frac{\partial \Delta p_n}{\partial t} = D_p \frac{\partial^2 \Delta p_n}{\partial^2 x^2} - \frac{\Delta p_n}{\tau_p} + G_L; \tag{3.6}$$

in which D_n, D_p are electron and hole diffusivity and G_L is the light generation rate. Since the light is switched off and assuming that the minority carrier diffusion

lengths L_n and L_p are much greater than W_p and W_n, respectively, under steady state conditions, Eqs. 3.5 and 3.6 can be simplified as follows:

$$D_n \frac{\partial^2 \Delta n_p}{\partial^2 x^2} = 0; \tag{3.7}$$

$$D_p \frac{\partial^2 \Delta p_n}{\partial^2 x^2} = 0; \tag{3.8}$$

To solve Eqs. 3.7 & 3.8, we apply boundary conditions for minority carriers at the interface of quasi-neutral region and space charge region according to the law of the junction, i.e.:

$$\Delta n_p(x = x_p) = \frac{n_i^2}{N_A}(e^{\frac{qV_A}{kT}} - 1); \tag{3.9}$$

$$\Delta p_n(x = -x_n) = \frac{n_i^2}{N_D}(e^{\frac{qV_A}{kT}} - 1); \tag{3.10}$$

In the vicinity of the front and back selective contacts, minority carriers recombine with majority carriers at the rate of S_f and S_b, respectively. Assuming negligible electric field inside the quasi-neutral region, recombination current at the edge can be written as follows:

$$J_n(x = W_p) = qD_n \frac{d\Delta n_p}{dx}|_{x=W_p} = qS_b \Delta n_p(x = W_p); \tag{3.11}$$

$$J_n(x = -W_n) = -qD_p \frac{d\Delta p_n}{dx}|_{x=-W_n} = qS_f \Delta p_n(x = -W_n); \tag{3.12}$$

plugging Eqs. 3.9, 3.10, 3.11 & 3.12 into Eqs. 3.7 & 3.8, the diffusion limited recombination current $J_{diff}(V)$ is derived as shown:

$$J_{diff}(V) = q(\frac{D_n}{N_A}\frac{S_b}{S_b(W_p - x_p) + D_n} + \frac{D_p}{N_D}\frac{S_f}{S_f(W_n - x_n) + D_p})n_i^2(e^{\frac{qV}{kT}} - 1); \tag{3.13}$$

in which n_i is the intrinsic carrier concentration of GaInP. Note that the solution here is simplified from previous derivation [52,53] by dropping out the recombination term in Eqs. 3.5 & 3.6, given the short-channel assumption described above. The second

term, radiative recombination current $J_{rad}(V)$ can be computed using the effective radiative recombination coefficient B_{eff} given as follows [51]:

$$J_{rad}(V) = q(W_n + W_p)B_{eff}n_i^2(e^{\frac{qV}{kT}} - 1); \tag{3.14}$$

the last term in Eq. 3.4 can be approximated by Eq. 3.14 according to [51]: [51]:

$$J_{SCR}(V) = q\frac{(x_n + x_p)}{\sqrt{\tau_n \tau_p}}n_i(e^{\frac{qV}{2kT}} - 1); \tag{3.15}$$

where x_n and x_p in Eqs. 3.13 and 3.15 are depletion widths in the n and p-doped regions, respectively, and can be expressed as follows:

$$x_n = \sqrt{\frac{2\varepsilon_r\varepsilon_o}{q}\frac{N_A}{N_D(N_A + N_D)}(V_{bi} - V)}; \tag{3.16}$$

$$x_p = \sqrt{\frac{2\varepsilon_r\varepsilon_o}{q}\frac{N_D}{N_A(N_A + N_D)}(V_{bi} - V)}; \tag{3.17}$$

in which q is the elementary charge; ε_o is the vacuum permittivity; ε_r is the relative permittivity of GaInP; and V_{bi} is the built-in potential of the junction. Summing up Eqs. 3.13 - 3.15, we can now calculate the diode injection current $J_{inj}(V)$ for the FHJ.

Rear Hetero-Junction. The RHJ structure also consists of two crucial layers: the 1.04 μm thick n-doped GaInP emitter, and the 0.1 μm thick heavily p-doped AlGaInP BSF layer. S_f is defined identically to FHJ, as the window layer is omitted from both cases. Recall that the BSF layer is regarded as the "pseudo" base layer for RHJ, only the back contact layer is supposed to be connected with the BSF, thus $S_b = 10^7$ cm/s in RHJ at the BSF/contact surface, and S_{int} depicts the interface recombination loss between GaInP/AlGaInP which is equivalent to S_b defined in FHJ. Analogous to the derivation of $J_{diff}(V)$ in FHJ, $J_{diff}(V)$ in RHJ can also be obtained according to simplified MCDE:

$$J_{diff}(V) = q(\frac{D_n n_{i,p}^2}{N_A}\frac{S_b}{S_b(W_p - x_p) + D_n} + \frac{D_p n_{i,n}^2}{N_D}\frac{S_f}{S_f(W_n - x_n) + D_p})(e^{\frac{qV}{kT}} - 1) \tag{3.18}$$

in which $n_{i,p}$ is the intrinsic carrier concentration of AlGaInP, while $n_{i,n}$ is the intrinsic carrier concentration of GaInP. Likewise, $J_{rad}(V)$ and $J_{SCR}(V)$ are given by:

$$J_{rad}(V) = qW_n B_{eff}n_{i,n}^2(e^{\frac{qV}{kT}} - 1); \tag{3.19}$$

$$J_{SCR}(V) = q\frac{(x_n + x_p)}{\sqrt{\tau_{n,eff}\tau_{p,eff}}}\sqrt{n_{i,n}n_{i,p}}(e^{\frac{qV}{2kT}} - 1); \tag{3.20}$$

Note that contribution to $J_{rad}(V)$ from the BSF layer is omitted, because $n_{i,p}^2 W_p \ll n_{i,n}^2 W_n$. For $J_{SCR}(V)$ of RHJ, minority carrier lifetime needs to be modified to account for additional defect-assisted interface recombination in the SCR. According to [54, 55], the effective minority carrier lifetime is given as the summation of bulk SRH recombination and interface recombination activity:

$$\frac{1}{\tau_{p,eff}} = \frac{1}{\tau_p} + \frac{1}{\frac{W_n^2}{\pi^2 D_p} + \frac{W_n}{S_{int}}}; \tag{3.21}$$

As can be understood intuitively, a higher S_{int} would result in more severe recombination at GaInP/AlGaInP interface and a smaller τ_{eff}. Thus, this effect increases $J_{SCR}(V)$, in accordance with Eq. 3.20.

3.3.3 Results

The parameter values used in the analytical model for FHJ and RHJ photovoltaics are summarized in Table. 3.1 below:

Table 3.1.: Summary of Parameter Values for Analytical Model

	FHJ	RHJ
τ_p/τ_n(ns)	200/200	100/2 [39]
μ_p/μ_n(cm^2/Vs)	30/500 [56]	30/500
$S_f/S_b/S_{int}$ (cm/s)	$10^4/10^2$/NA [56]	$10^4/10^7/10^2$
B_{eff}(cm^3/s)	5×10^{-12}	5×10^{-12}

Here the mobility and interface recombination velocities were obtained from previously published literature, while minority carrier lifetimes for the absorber of FHJ and RHJ were determined by fitting to the experiment. The minority carrier lifetime for a FHJ is generally higher than that of a RHJ, according to the Scharfetter

relation [57, 58], since the absorber doping in a FHJ is one magnitude order lower, and the minority electron lifetime τ_n in the heavily doped BSF layer for a RHJ is even shorter. The electron mobility may not be very susceptible to the outcome as long as the minority carrier diffusion length is longer than the quasi-neutral region width, we assumed identical hole mobility in a RHJ compared to a FHJ by neglecting the doping-dependent mobility degradation [59, 60]. The B_{eff} is determined by solving $J_{o,rad} \cong qW_n B_{eff} n_{i,n}^2$, using the experimental value of $mathrm J_{0,rad}$ [35]. The analytical model developed above is now calibrated to the experimental data adapted from [35]. The results are shown in Fig. 3.5. As can be seen in Fig 3.5, the ma-

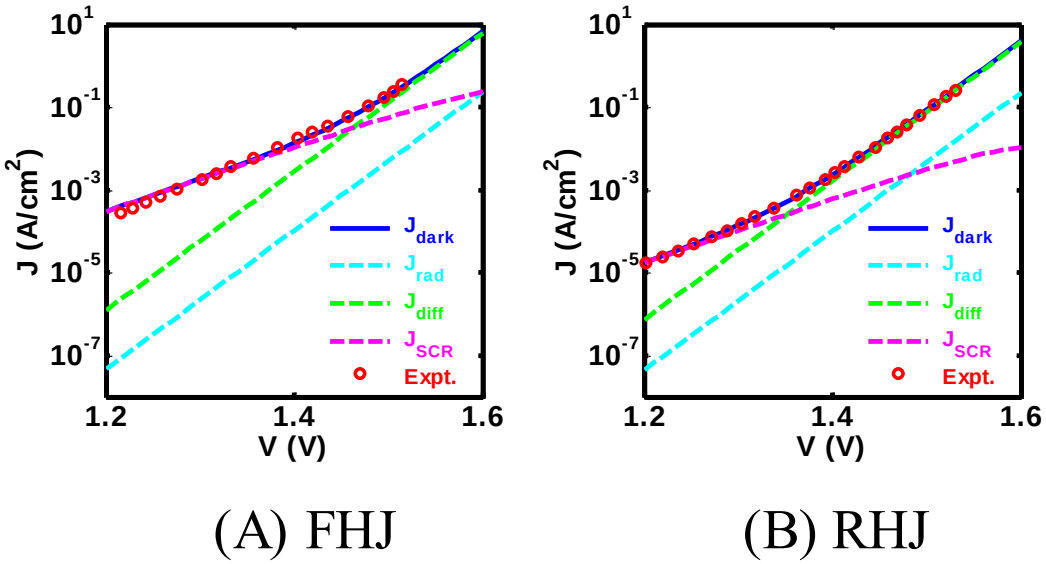

Fig. 3.5.: Schematics to calibrate the analytic model J_{dark}, which is a sum of three recombination current terms J_{SCR}, J_{diff} and J_{rad} against experimental data: (A) FHJ; (B) RHJ. In both cases, good agreement between the total predicted and experimental dark current are observed.

jor difference between J_{dark} of FHJ and RHJ at the vicinity of V_{OC} (∼1.4V) is the considerable suppression of J_{SCR} in RHJ. To fully understand the major discrepancy between two configurations, we break down the expression of J_{SCR} term-by-term near V_{OC}.

Due to the high doping in emitter and base layer of the RHJ, the effective minority carrier lifetime is much shorter, while the total depletion width $x_n + x_p$ is slightly suppressed. Still, the drop in the intrinsic carrier concentration will reduce J_{SCR} overall. For a RHJ cell, the high-E_g AlGaInP BSF layer has a much smaller intrinsic carrier concentration, given by:

$$n_{i,p} = \sqrt{N_c N_v} e^{-\frac{E_g}{2kT}}; \tag{3.22}$$

Thus, n_i can be calculated through Eq. 3.22; $n_{i,n}$ of GaInP is approximately $2 \times 10^3/cm^3$; due to the high E_g, $n_{i,p}$ of AlGaInP is approximately $0.2/cm^3$. As a result, the effective intrinsic carrier concentration $\sqrt{n_{i,n} n_{i,p}}$ is approximately two orders of magnitude smaller than that of the FHJ. Given that the suppression of J_{SCR} is a result of the high-E_g BSF layer, the potential benefit of the RHJ design becomes much more clear. To reduce the recombination loss at SCR, at least one side of the junction should have high E_g. If the high E_g material is placed in front, the absorber layer will have to give up a large fraction of absorption from the solar spectrum due to the shift of band edge. Under the RHJ, the high E_g layer is placed near the back contact so that it does not absorb sunlight, since above-E_g photons have already been absorbed in the front thick emitter layer and therefore a hole-selective layer beyond AlGaInP is not needed.

Combining Eqs. 3.20 and 3.22, we see that rising the E_g of base will suppress J_{SCR} and plateau V_{OC} until J_{SCR} is negligibly small compared to J_{diff} near the vicinity of V_{OC}. In reality, increasing the E_g of the base layer will only theoretically increase the V_{OC} by 10 mV. This is because J_{SCR} is already smaller than J_{diff} at V_{OC} in the RHJ device, which indicates that V_{OC} is dictated by J_{diff} not J_{SCR}. In fact, a good RHJ base candidate should have two major requirements: First, the base should have a relatively high E_g as derived from analytic formula. To effectively block minority electrons and transport majority holes, a wider E_g has to be fully compensated by lower electron affinity. Second, the hetero-interface formed between emitter and base must be well-passivated to ensure the low S_{int} at the rear side as addressed in Eq. 3.21. Another way to improve V_{OC} is to raise the emitter doping. However, we believe

that V_{OC} would quickly saturate with emitter doping. The reasons are as follows: first, according to Scharfetter relation [57, 58], heavy doping would degrade minority SRH lifetime of the absorber and enhance the bulk SRH recombination. On the other hand, the doping-dependent mobility model [59,60] suggests that increasing the emitter doping would also decrease the carrier mobility. Both doping-dependent SRH lifetime and doping-dependent mobility are not accounted for in the analytic model, as the corresponding parameter values for GaInP have not been presented in the literature. Moreover, doping-induced E_g narrowing effect [61] was not incorporated into the analytic expression, which also prevents V_{OC} from monotonically increasing with emitter doping. Nonetheless, the precondition of utilizing a RHJ over a FHJ for solar cell design is that minority carrier diffusion length should be longer than the absorber width [34], so that generated electron-hole pairs will not suffer severe bulk recombination in the absence of an electric field to assist in charge separation.

From the experimental perspective, it is important to decide in advance whether to fabricate solar cell devices employing a RHJ or a FHJ design. However, the analytical model is not sufficient to fully explore the tradeoffs between the two design configurations for two reasons: (1) photocurrent cannot be extracted from the dark current analytic model, which may require rigorous self-consistent device simulation to compute. (2) The minority carrier diffusion length may not always be greater than quasi-neutral region width, and superposition may fail under certain circumstances, which will revoke the validity and applicability of the simple analytic model developed above. Therefore, it is essential to set up a self-contained device simulation of both RHJ and FHJ GaInP solar cells using a drift-diffusion solver to explore the tradeoffs between the two configurations. In the next section, we will discuss how to develop and utilize this simulation framework effectively.

3.4 Numerical Model

In this section, we employ *Sentaurus* TCAD, which solves drift-diffusion equations coupled with Poisson equation for semiconductor devices, to assess the performance of FHJ and RHJ under various bulk and surface properties. The global temperature is 300K in the simulation environment.

We set up our framework using the layer thickness and doping profile within the simulation domain, as depicted in Fig. 3.1. In analogy with other III-V materials like GaAs [45], GaInP absorbs light strongly, so ray tracing is a reasonable approximation to compute the optical generation within the solar cell. With solar illumination incident on the top, shadowing and front reflection loss of ARC are not modeled explicitly, but instead a constant front side reflectivity of 7% for the GaInP solar cell is defined at the optical interface, which is consistent with the reported experimental J_{SC}. All the parameters associated with electrical transport property are summarized in Table. 3.2 below, and the SRH lifetime τ_{SRH} within the absorber is varied to explore different bulk properties.

Table 3.2.: Summary of Parameter Values for Numerical Model

	AlInP	GaInP	AlGaInP
$\varepsilon/\varepsilon_o$	11.8	11.88	11.8
μ_n, μ_p[cm^2/Vs]	100,10	500,30	100,10
E_g[eV]	2.3	1.81	2.39
N_C[cm^{-3}]	10^{20}	6.55×10^{17}	10^{20}
N_V[cm^{-3}]	10^{19}	1.39×10^{19}	10^{19}
χ[eV]	3.78	4.12	3.43
τ_{SRH}[μs]	10^{-3}	Varied	10^{-3}
B_{eff}(cm^3/s)	0	5×10^{-12}	0

Ohmic boundary condition holds at the front and rear surface, therefore surface recombination velocities are 10^7 cm/s respectively. Previous simulation work [56, 62] have shown that the front interface properties between the AlInP window and GaInP absorber layers do not substantially degrade the GaInP solar cell performance, unless the effective interface recombination velocity $S_f > 10^4$ cm/s. Thus, S_f is fixed to 10^3 cm/s. Conversely, V_{OC} is strongly correlated to the effective carrier recombination velocity S_b at GaInP/AlGaInP hetero-interface near the back, as it serves as hole selective contact for FHJ and the p-n junction for RHJ. The radiative recombination model in *Sentaurus* TCAD is based on the following Eq. 3.23:

$$R_{net} = B_{eff}(np - n_i^2); \tag{3.23}$$

in which R_{net} is net radiative recombination rate; B_{eff} is the effective radiative recombination coefficient also described in Eqs. 3.14 & 3.19. Uniform doping profiles with abrupt doping change (depletion approximation) were assumed at all interfaces. The activated recombination models are Auger, radiative and SRH recombinations for all bulk regions. Non-radiative interface recombination is also active for the AlInP/GaInP and AlGaInP/GaInP interfaces. Constant mobilities of carriers are also employed at 300K with fixed doping concentration. Effective intrinsic carrier concentration that excludes E_g narrowing effect is also specified in *Sentaurus* TCAD command file.

We then consider one set of τ_{SRH} and S_b values for the FHJ and RHJ, respectively, so that we can reproduce the measured I-V performance previously reported in experiment [35, 63]. It is found that $\tau_{SRH} = 200$ ns and $S_b = 100$ cm/s for both FHJ and RHJ best describes the measured data [35], which is consistent with independent measures of these values for high-quality GaInP layers and interfaces.

Table 3.3.: Simulation Versus Experiment

	FHJ		RHJ	
	Expt.	Sim.	Expt.	Sim.
V_{OC}[V]	1.39	1.39	1.45	1.46
J_{SC}[mA/cm^2]	15.8	15.8	15.8	15.6
FF	0.86	0.86	0.89	0.88
η[%]	18.9	18.9	20.5	20.3

While performance variation exists among devices under test (DUT), our simulation framework is accurate to within 1% on each device metric in predicting the performance of both RHJ and FHJ cells with reasonable values of τ_{SRH} and S_b (i.e., they are consistent with independent measurements in the literature).

We then aim to utilize the simulation framework to identify the performance tradeoffs between FHJ and RHJ under various τ_{SRH} and S_b. We do so by sweeping τ_{SRH} from 0.1 ns to 10 μs, and S_b from 10 cm/s to 10^7 cm/s. As can be seen from Fig. 3.6, V_{OC} is strongly dependent on both τ_{SRH} and S_b. The RHJ cell design achieves higher V_{OC} due to the suppression of SNS recombination, which has also been confirmed by the analytical model derived above. A FHJ exhibits higher J_{SC}, especially when τ_{SRH} is low, because the electric field inside SCR can help separate generated carriers, thus reducing the time minority carriers have to recombine. Conversely, in the absence of a SCR up front, a RHJ requires significantly longer diffusion lengths for minority carriers to avoid severe recombination losses before carrier collection. The J_{SC} generally has a very weak dependence on S_b, because under short circuit conditions, electron hole pair generation due to photon absorption occurs mostly near the front; it will rarely diffuse to the back surface and recombine. Both ΔJ_{SC} and $\Delta\eta$ have shown weak dependence on S_b, and as illustrated in Fig. 3.6, as we are considering a wide range of SRH lifetime (0.1 ns to 10 μs) that strongly impact the J_{SC} of the RHJ to an extent that outweighs the V_{OC} variation within that range. Therefore,

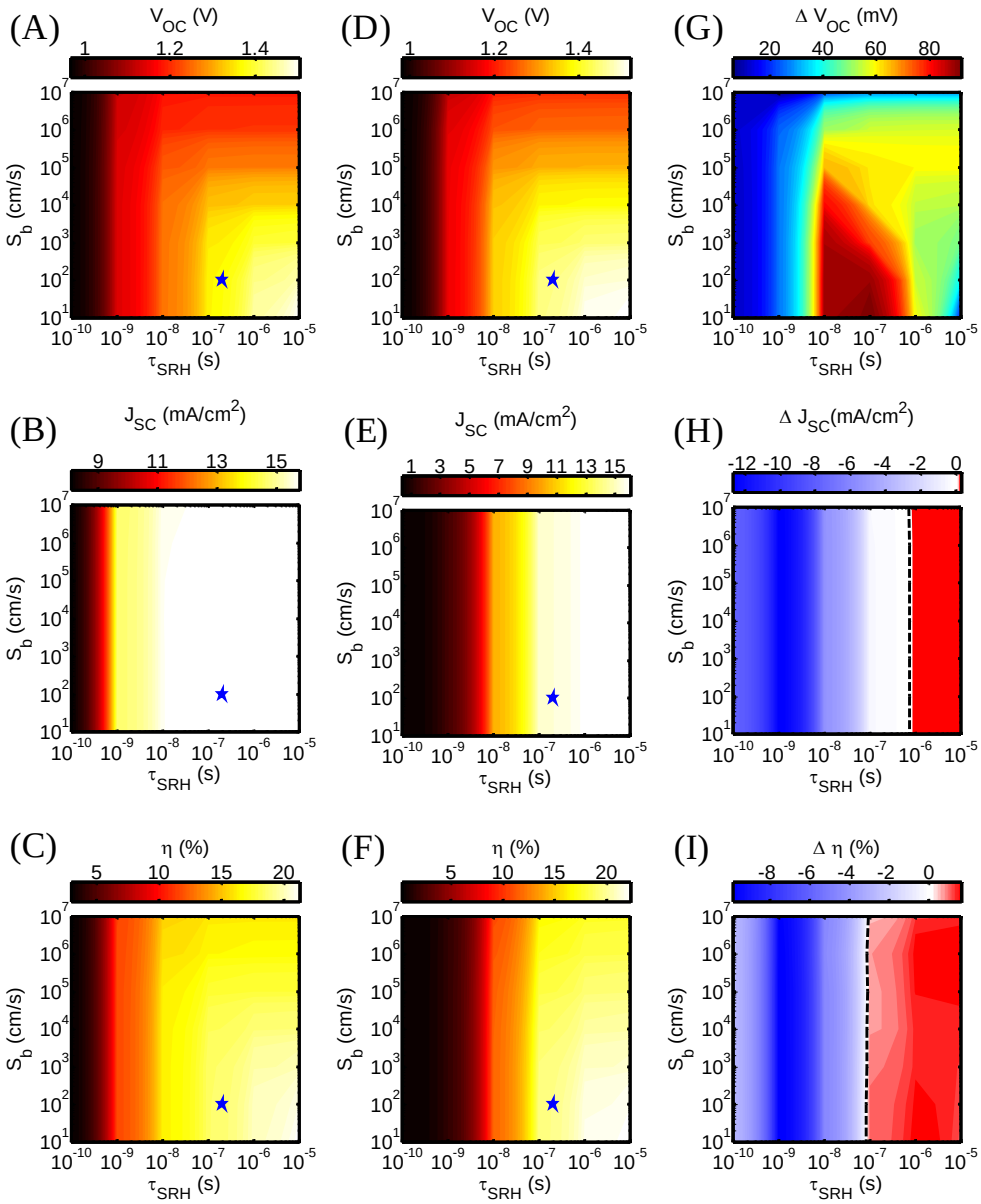

Fig. 3.6.: Contour plot of open circuit voltage V_{OC}, short circuit current J_{SC}, and GaInP cell efficiency η with various absorber SRH lifetime τ_{SRH} and GaInP-AlGaInP interface recombination velocity S_b. (A)-(C). FHJ. (D)-(F). RHJ. (G)-(I). Subtracting FHJ values from RHJ values. Blue stars in (A)-(F) mark the $\tau_{SRH} = 200$ ns and $S_b = 100$ cm/s points.

$\Delta\eta$ is mainly dictated by ΔJ_{SC} with a low S_b constraint. The performances of both design cross one another around $\tau_{SRH} = 100$ ns. This conclusion is not only consistent with our earlier model, but also the historical path towards efficiency optimization of wide-E_g GaInP solar cells. This phenomenon can be understood as follows. In 1994, Takamoto et al. [34] reported record efficiencies of wide-E_g GaInP solar cells based on FHJ designs, and reported SRH lifetimes barely exceeding 10 ns. Two decades later, the reported SRH lifetime reached $\sim$100 ns [39], and passed the efficiency tradeoff line between FHJ and RHJ, allowing the RHJ design to become a higher-performing choice for wide-E_g GaInP solar cell.

3.5 Discussion

In this chapter, we have numerically and analytically demonstrated that the efficiency of wide-E_g GaInP solar cell can improve from traditional FHJ design by using a counterintuitive RHJ design for high-quality bulk absorber (where $\tau_{SRH} \geq 100$ ns). A front heterojunction could be an alternative, where a high-E_g n-AlInP window layer would be deposited on top of the p-GaInP absorber to separate photo-generated carriers and suppress SNS recombination, according to Eq. 3.20. If we treat the top of the AlInP window layer as an Ohmic contact with $S_f = 10^7$ cm/s , J_{diff} will increase according to Eq. 3.13. Unlike the rear heterojunction configuration, a large S_f will be much more detrimental than a large S_b, since most photon absorption occurs near the front side of solar cell. In this case, a front heterojunction design may not be as good as a rear heterojunction design. If we compare to the Shockley-Queisser limits for solar cells with $E_g = 1.81$ eV, as summarized in Table. 3.4, the biggest gap with respect to state-of-the-art record wide-E_g GaInP solar cells comes from non-idealities in J_{SC}.

Table 3.4.: Rear-Heterojunction GaInP Versus S-Q Limit

	S-Q limit	RHJ GaInP	%max
V_{OC}[V]	1.54	1.45	94.2%
J_{SC}[mA/cm^2]	19.6	15.8	80.6%
FF	0.93	0.89	95.5%
η[%]	28.2	20.5	72.7%

On one hand, a fraction of the 19.4% total losses comes from an imperfect ARC (roughly 7% reflective loss) combined with parasitic absorption in the AlInP window layer. On the other hand, although GaInP is a direct bandgap semiconductor with a sharp absorption rise near its band edge λ_{E_g}, a 1 μm-thick absorber is not sufficiently thick to completely absorb the entire solar spectral range of interest ($\lambda < \lambda_{E_g}$). As illustrated in Fig. 3.7, based on the optical dispersion (n-k) data for a 1.81 eV

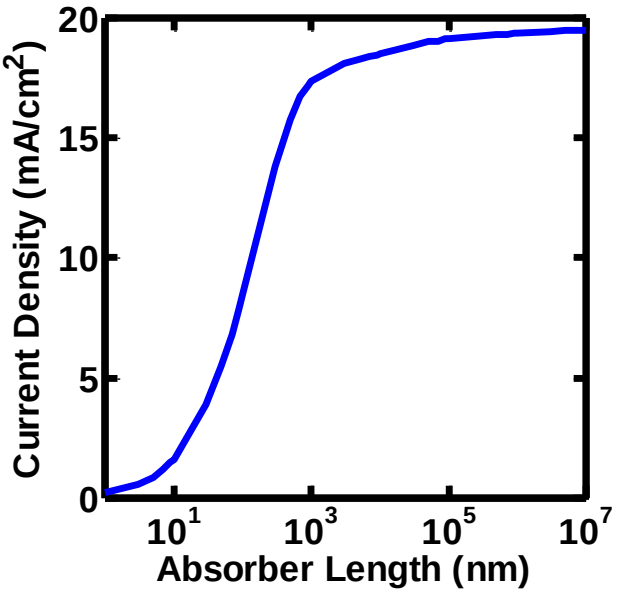

Fig. 3.7.: The current density converted by absorbed photon flux from AM1.5G solar spectrum as a function of absorber layer thickness assuming unit quantum efficiency.

wide-E_g GaInP semiconductor and assuming a perfectly transmitting surface at the front with unit quantum efficiency throughout the wavelength spectrum of interest, a 1 μm thick absorber can only yield a J_{SC} of 17.4 mA/cm^2, which is approximately 2.2 mA/cm^2 below the S-Q limit. A lossless perfect planar reflector at the back (R = 1) would double the mean path length of light propagation [64], but even with this improvement, the absorber thickness is not sufficient for complete absorption near the band edge. Simply fabricating the absorber with an order of magnitude greater layer thickness ($\sim$ 10μm) could absorb a photon flux equivalent to a J_{SC} of 18.6 mA/cm^2, but would rapidly degrade the carrier collection efficiency as the layer thickness approaches the minority carrier diffusion length within the absorber and induce a non-negligible bulk SRH recombination. Thus, we proposed a Lambertian diffusive reflector [65] or photonic light-trapping structure at the back [66] to enhance the light absorption while maintaining good electron transport properties in the absorber. These light trapping schemes have been previously investigated for absorption enhancement in indirect-bandgap materials such as Si, with very weak absorption coefficients near the optical bandgap [67–69]. It allows the incident light to scatter back into the absorber in a random direction, where the average path length of propagation can be increased by a factor up to $4n^2$ [64, 70, 71] where n is the refractive index of the absorber. In principle, certain wavelengths can be enhanced even more, but it is difficult for this effect to span the whole solar spectrum [61]. For a GaInP absorber, $n^2 \cong 10$ near the optical band edge. To assess the implementation of the Lambertian diffusive reflector in a RHJ GaInP solar cell, we mimic the lossless diffusive reflector by modifying simulation framework as follows: (1) Absorber layer thickness was extended from 1 μm to 10 μm to obtain an enhanced optical generation profile; (2) The optical generation due to the absorption of low energy photons beyond 1 μm was chopped off and uniformly distributed within 1 μm absorber to get an updated optical generation profile to mimic the effect of a diffusive reflector; (3) The updated optical generation profile was incorporated into the Poisson coupled drift-diffusion solver to calculate the updated I-V characteristics of RHJ GaInP solar cell. We constrained the

identical recombination parameter with $\tau_{SRH} = 200$ ns and $S_b = 100$ cm/s. With an updated optical generation profile due to the diffusive reflector, $J_{SC} = 16.7$ mA/cm^2, $V_{OC} = 1.47$ V, FF = 0.89 and $\eta = 21.7\%$ can be achieved, which slightly exceeds both the previously simulated η of 20.3%, as well as the state-of-the-art reported efficiency of 21.4%.

3.6 Conclusion

Optimizing the design of wide-E_g GaInP solar cell to allow their performance to approach the Shockley-Queisser Limit is of great importance in the field of high efficiency multi-junction Photovoltaics. In this work, we addressed the significance of employing RHJ and FHJ designs for wide-E_g GaInP solar cell by introducing a simple physics-based analytic model to break down each recombination loss mechanism for both RHJ and FHJ design configurations. The advantage of the RHJ design manifested itself by moving the p-n junction to the back side and suppressing the SRH recombination within depletion (SNS recombination) so as to raise its V_{OC}. We also explored the tradeoffs between RHJ and FHJ through rigorous self-consistent numerical simulation and it was concluded that regardless of the rear interface condition, a high-quality bulk property with $\tau_{SRH} = 100$ ns is the key requirement for RHJ designs to prevail. This result is consistent with the historical switch from early FHJ devices to the modern RHJ-based record GaInP photovoltaics reported in recent years. Furthermore, these findings are extremely helpful to assist experimentalists in deciding which design configuration to use, given the transport property of the absorbers they can deposit, such as the bulk SRH lifetime characterized by time-resolved photoluminescence (TRPL). Finally, we propose adding a diffusive Lambertian or photonic reflector to the back of the device to achieve optimal absorption of solar incident photons above E_g. Using a modified numerical simulation framework to mimic such an effect, we have found that the efficiency can reach as high as 21.7% with no further modifications. This prediction suggests a promising path for future optimization

for wide-E_g GaInP solar cells towards the S-Q limit. Future work may investigate potential advantages and disadvantages of introducing Lambertian reflectors in the top cell of III-V multi-junction photovoltaics devices.

4. EXPLORATION OF VAPOR-LIQUID-SOLID GROWN INDIUM PHOSPHIDE SOLAR CELLS

4.1 Introduction

Despite the fact that state-of-the-art record solar cells are made of III-V compound (e.g. GaAs for single junction and InGaP/GaAs for tandem junction) [72], c-Si remains the dominant PV material candidate in the solar cell market. High capital expense and scaling challenges have prevented III-V materials from becoming the predominant choice in the PV market. Thus, it is critical to explore more cost-effective growth methods for III-V materials.

The Vapor-Liquid-Solid (VLS) was brought to attention and has become a dominant option for nanostructure growth due to its simplicity, flexibility, and controllability [73]. The recently developed Thin-Film Vapor-Liquid-Solid (TF-VLS) growth platform presents a way of growing high quality material at significantly reduced module cost and was successfully demonstrated for InP [74–77]. InP has a E_g of 1.34 eV, which is near-optimal for a single junction solar cell [78]. However, it was identified from the I-V characteristics that VLS-grown InP solar cells show a lower V_{OC} than champion InP cells grown by traditional metal organic chemical vapor deposition technique on epitaxial substrates [79]. Hence, understanding the performance degradation of InP solar cell fabricated using VLS growth recipe is an essential intermediate step towards optimization of this cost effective growth method.

In this chapter, we consider the V_{OC} degradation from two different perspectives: (1) E_g narrowing and (2) local shunting. During TF-VLS growth, an Indium film is

[0]The content of this chapter is primarily taken from a published conference proceeding: Y. Sun, X. Sun, S. Johnston, C. M. Sutter-Fella, M. Hettick, A. Javey and P. Bermel, "V_{OC} Degradation in TF-VLS Grown InP Solar Cell" *IEEE 43rd Photovoltaic Specialists Conference (PVSC)*, Portland, OR, (2016): pp. 1934-1937.

heated in PH_3 gas and transformed to InP by diffusion of Phosphorus into the liquid Indium followed by nucleation of InP and rapid dendritic growth of thin film InP exhibiting grains (> 100 μm) much larger than the film thickness (~ 3 μm) [74, 75]. High optoelectronic quality TF-VLS InP has been demonstrated [75]. n-InP layers are doped p-type with Zinc by an ex-situ doping process before the electron selective TiO_2 contact is deposited, followed by ITO as the transparent front electrode and individual cell patterning by lithography [76].

4.2 Methodology

To fully understand and quantify the V_{OC} degradation seen in TF-VLS grown InP solar cell, we document two hypotheses from different aspects based on the characterization outcome.

4.2.1 Bandgap Narrowing

The photoluminescence (PL) image of TF-VLS InP exhibits some lateral variation in PL intensity over an area of 1.3 mm×1.3 mm as visualized in Fig. 4.1. Grain boundaries and dendritic growth pattern can be clearly seen in the millimeter scale image. In order to correlate the observed PL inhomogeneity and cell performance, a lateral 2D spatially-resolved V_{OC} distribution graph was generated, based on the PL image. It is assumed that the luminance (a.u.) is proportional to $\exp(qV_{OC}/kT)$, with the V_{OC} obtained from single-crystal hetero-junction InP solar cell used as an upper limit (0.78 V) [81], and VLS-grown cell voltages as a lower limit (0.69 V). The V_{OC} distribution color map is generated as shown in Fig. 4.1. Since the sample is divided into $m \times n$ elementary unit cells, an H-SPICE based compact model of InP network is constructed to combine I-V characteristics of elementary unit cells to reproduce the I-V characteristics of the TF-VLS grown sample.

To implement the compact model, all of the elementary unit cells are divided into two types: (1) good unit cells that have identical I-V performance with hetero-junction

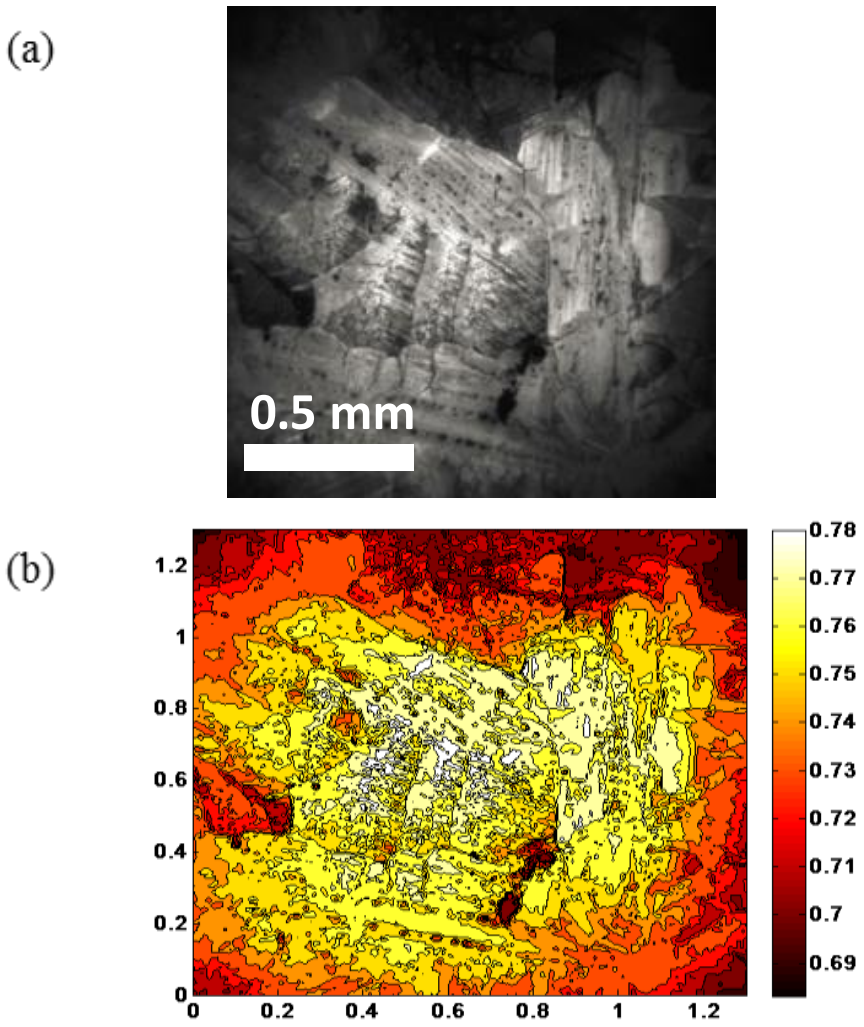

Fig. 4.1.: (a). Photoluminescence image of TF-VLS grown InP solar cell (area: 1.3 mm×1.3 mm) [80]. (b) Color map of the V_{OC} at each unit cell. Units in both lateral directions are in mm.

wafer based InP cell, and (2) bad unit cells that have degraded I-V performance, due to the E_g narrowing effect.

The E_g narrowing effect assumes some Indium rich areas caused by phosphorus deficiency on the sample so that $In_x(InP)_{1-x}$ forms presumably at the surface and along grain boundaries. Because Indium element is a metal with E_g of 0 eV, the E_g of $In_x \cdot (InP)_{1-x}$ can be modeled as $(1-x) \cdot 1.34$ eV, where 1.34 eV is the nominal

E_g of InP at room temperature (T = 300 K) and x is the compositional ratio of Indium element in local Indium rich area. The PL image suggests that some regions may have an effective E_g smaller than the expected E_g of single crystal InP at the surface of our VLS-grown InP sample. There are at least several possible explanations: (1) deviation from perfect stoichiometry; (2) laterally inhomogeneous doping distributions profile or electron affinities; or (3) deep-level defects approximately 0.3 eV above the valence band maximum (VBM). PL spectra of the Zn-doped TF-VLS grown InP sample taken at T = 8 K [76] are used to quantify the effective E_g of those degraded cells. Besides the dominant band-to-band (BB) and band-to-acceptor (BA) photoluminescence, an extra peak (BA-LO) was also identified, which is strongly correlated with E_g narrowing. The effective E_g therefore, can be extracted from our PL spectra. We expect that temperature-dependent E_g will follow the Varshni relation of for a semiconductor, which is given by [82]:

$$E_g(T) = E_g(0) - \frac{\alpha T^2}{T + \beta}; \tag{4.1}$$

where α and β are fitting parameters varied with different semiconductor materials. For InP, $\alpha = 3.63 \times 10^{-4}$ eV/K and $\beta = 162$ K. Because the BA-LO energy is 1.27 eV as indicated in [76], the phosphorous content may be reduced roughly 5% from a 1:1 ratio in this sample. To set up the H-SPICE compact model simulation framework for the InP network, threshold voltage of 0.75 V is used to split elementary unit cells in two categories. Those unit cells with local V_{OC} greater than 0.75 V are labeled as "good cells" whereas remainder unit cells are treated as "degraded cells". I-V characteristics of wafer-based hetero InP cell is modeled through *Sentaurus* TCAD as depicted in Fig. 4.2 and implemented as local I-V data for "good cells". The I-V characteristics of $InP_{0.95}$ degraded cells are generated by reducing the E_g from 1.34 eV to 1.27 eV and shifting the absorption spectra accordingly while maintaining the same recombination parameter values. Two sets of I-V data are combined in the H-SPICE compact model to reproduce the overall I-V characteristics of a TF-VLS grown InP solar cell. The energy band diagram at V_{OC} condition is also plotted in Fig. 4.2, showing that using TiO_2 as the electron selective buffer layer in the structure creates

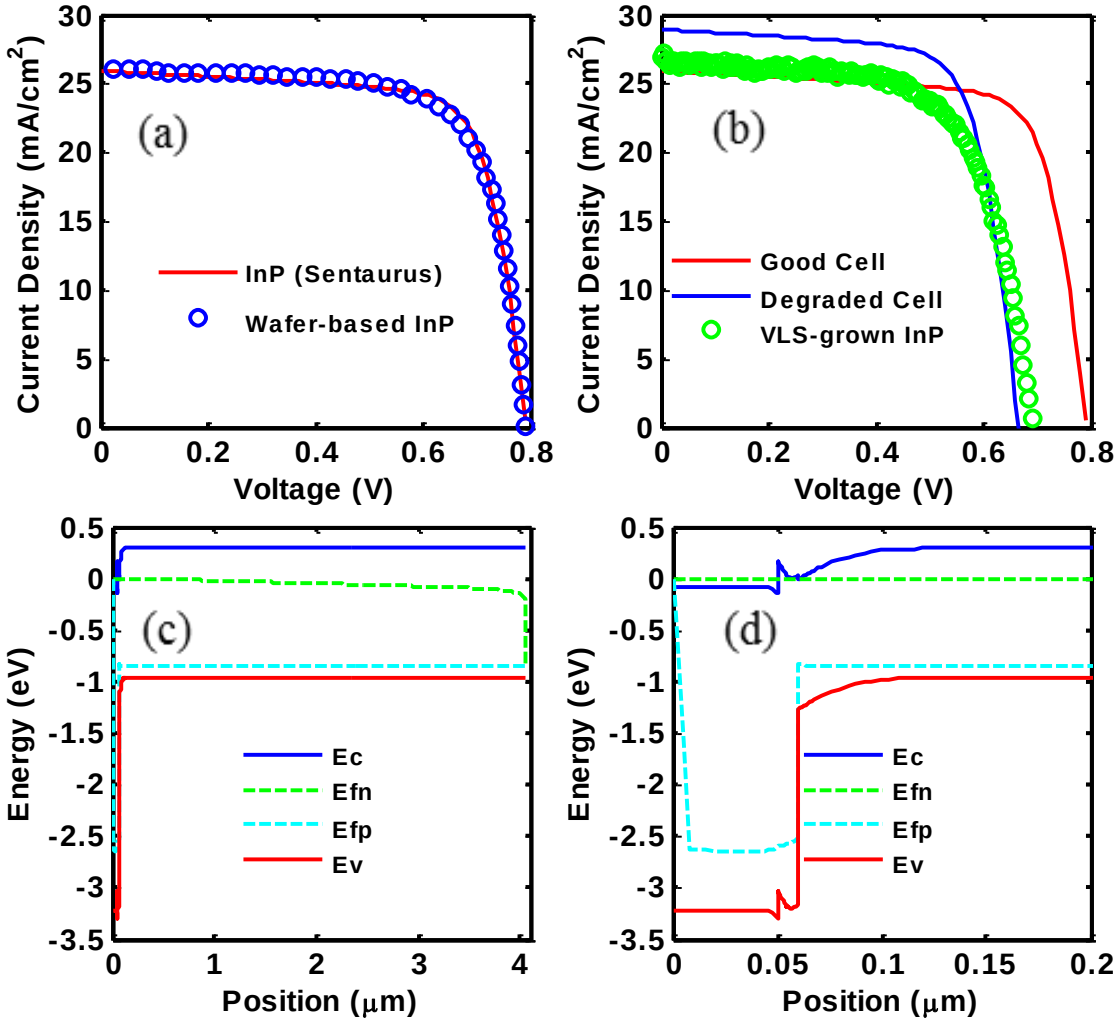

Fig. 4.2.: (a). TCAD *Sentaurus* simulated I-V characteristics of wafer-based InP solar cell. (b). I-V characteristics of wafer-based InP implemented as local I-V data for non-degraded unit cells and I-V characteristics incorporating E_g narrowing effects applied as local I-V data for degraded unit cells. (c). and (d). are overall and zoomed-in energy band diagrams of wafer-based InP solar cell plotted under V_{OC} condition with AM1.5G illumination.

a large valence band offset to block minority holes from reaching the electron contact, mitigating large SRH recombination in the space charge region of the ITO layer. The H-SPICE diode compact model of InP network presumes that $m \times n$ elementary unit

cells are connected in parallel to each other; sheet resistors (10 $\Omega/\square$) are placed at the interconnects between any two adjacent cells. Each elementary unit cell consists of a light-generated current source and a diode. The total current I in the unit cell is given by:

$$I = I_{SC} - I_o \exp(\frac{qV}{nkT}) \tag{4.2}$$

where I_{SC} is the light generated current with no applied voltage, I_o is the reverse saturation current; n is the ideality factor.

4.2.2 Local Shunting

Besides the E_g narrowing effect discussed above, elementary unit cell performance might also be degraded by low shunt resistance [83] connected in parallel with light generated current source and diode as depicted in Fig. 4.3 Temperature dependent dark I-V measurements of TF-VLS grown sample clearly exhibit shunting-dominated behavior under reverse and low forward bias condition. Note that due to some electrostatic charging and discharging effect, the dark I-V minima do not occur at the zero bias condition. The new diode equation, with shunt resistance included, is as follows:

$$I = I_{SC} - I_o \exp(\frac{qV}{nkT}) - \frac{V}{R_{sh}} \tag{4.3}$$

Putting the shunt resistance in the ideal diode model would result in degradation of I-V performance, especially in the fill factor (FF) and V_{OC}. The degradation would not be observable unless the shunt resistance were less than 1 $k\Omega - cm^2$. In order to model local shunt effects quantitatively, it was assumed that shunt resistance is added to unit cells that are categorized as "degraded cells". The H-SPICE compact model of InP network is also constructed to produce the overall I-V performance of the TF-VLS grown sample.

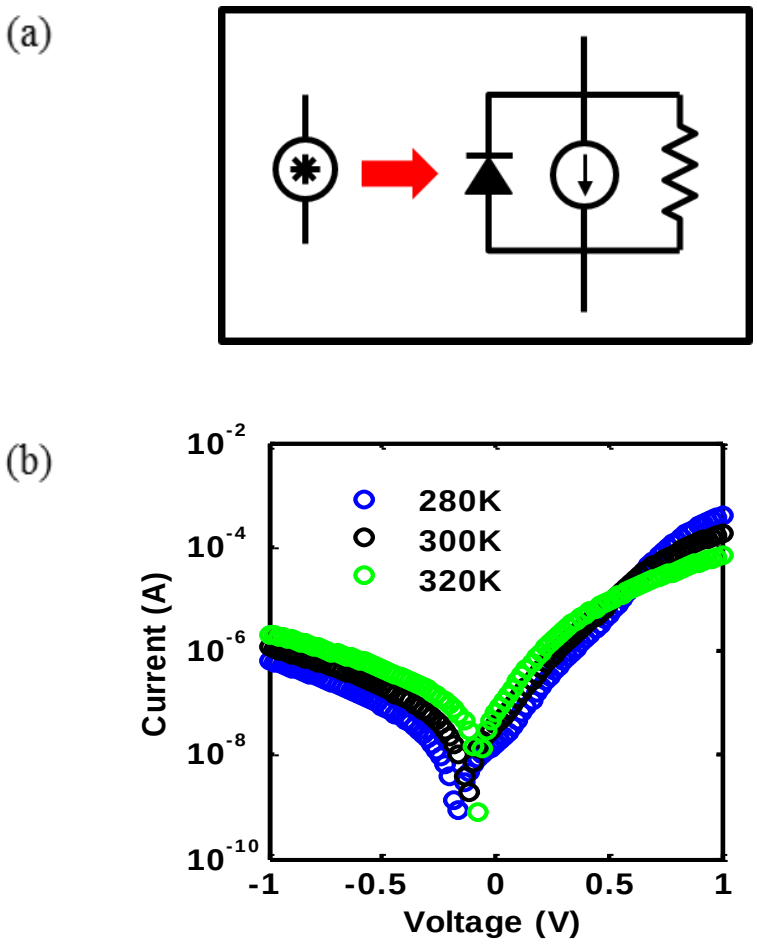

Fig. 4.3.: (a). Internal circuit structure of elementary unit cell includes shunt resistance connected in parallel. (b). Dark I-V characteristics of TF-VLS grown InP cell measured at 280 K, 300 K and 320 K.

4.3 Results & Discussion

Incorporating E_g narrowing effect in the simulation with reasonable external shunt resistance added, the resulted I-V has shown good agreement in V_{OC}, J_{SC} and FF with good curve fit to measured I-V characteristics of VLS-grown sample. The power consumptions of total unit cells are plotted under V_{OC} condition. Since unit cells are distinguished as good and degraded cells based on threshold voltage we set, while good cells are generating powers under V_{OC} condition, degraded cells start to consume

power which can be clearly seen in Fig. 4.4. The power consumption of degraded cells offsets the power generation of good cells at open circuit. The plots due to local shunting have shown that adding a shunt resistance in the elementary unit cell could be more harmful to current collections at small voltage bias than to the V_{OC}. And it turns out that E_g narrowing achieve much better fitting. The FF discrepancy in the E_g narrowing hypothesis might be as a result of the absence of shunting resistance. Therefore, adding shunt resistance to some local dark unit cells while assuming E_g narrowing for all degraded cells could optimize the I-V fitting. Local shunting in TF-VLS p-InP might arise from dopant inhomogeneities and dopant clustering of non-activated Zn atoms. A dopant activation of about 10% was extracted from comparative SIMS and C-V measurements [76]. As indicated in Fig. 4.5(a), non-ideal shunts have higher impact on voltage-dependent current density at small bias than on the reduction of V_{OC}. The observation implies that local shunting is not the primary cause of V_{OC} degradation but might be a secondary factor that contributed to it.

4.4 Conclusion

In this chapter, we considered two hypotheses to explain the V_{OC} degradation of TF-VLS grown InP solar cells. First, the E_g narrowing effect assumes slight deviations from 1:1 In:P stoichiometry may exist in the InP sample. Extracting information from various characterization results (e.g. PL image and PL spectra) and establishing H-SPICE diode compact model based InP network can then be used to predict the I-V performance of the sample. This result achieves a good match to the measured I-V of VLS sample. Second, local shunting effect was also considered by adding shunt resistance to the individual degraded cells. It is predicted that combining two hypotheses together, optimized fitting I-V curves could be produced to establish a comprehensive physics based theory to explain the V_{OC} degradation in the TF-VLS grown InP solar cell. Future work should consider modeling of the random fractal

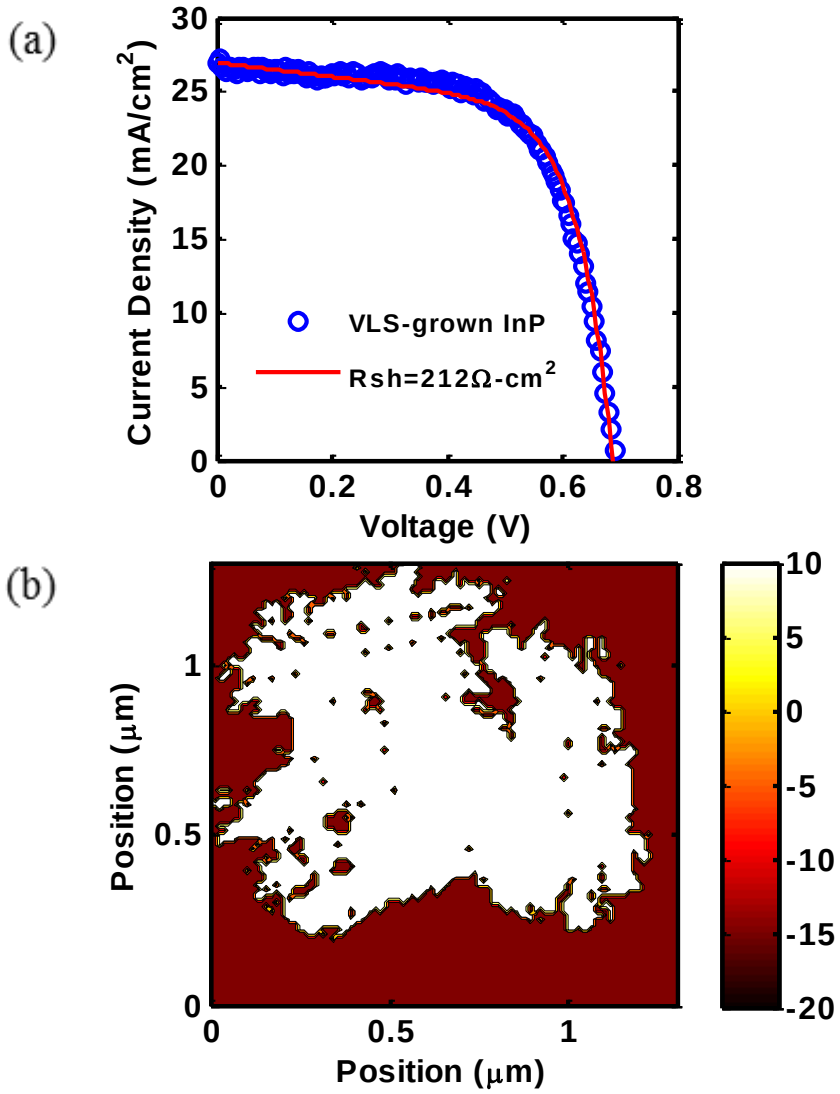

Fig. 4.4.: (a). I-V characteristics of the InP network due to E_g narrowing shows reasonable fit to measured I-V of the VLS-grown sample. (b). Power consumption and generation of good and degraded cells in the sample at V_{OC} condition under E_g narrowing.

network to mimic lateral dendritic polycrystalline growth pattern observed in TF-VLS growth process and explain the small uncertainty of measured V_{OC}. Furthermore, from the experimental perspective, an in-situ doping process is currently explored to control the doping profile better and increase the dopant activation which possibly

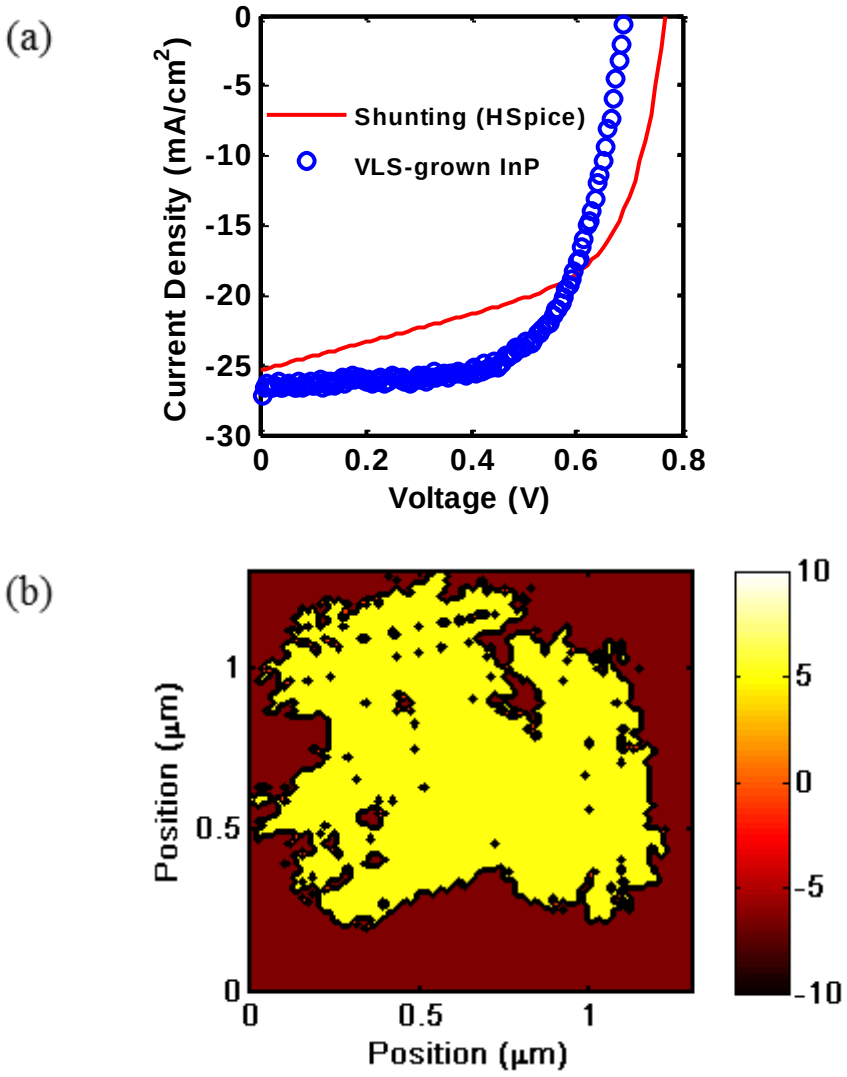

Fig. 4.5.: (a). I-V characteristics of the InP network with shunt resistance of 50 $k\Omega - cm^2$ compared to measured I-V characteristics of the VLS-grown sample. (b) Power consumption and generation of good and degraded cells in the sample at V_{OC} under local shunting.

helps eliminate local shunting in TF-VLS p-InP. Further improvement could be made by fabricating VLS-grown single crystal n-InP deposited on Molybdenum substrate to mitigate surface inhomogeneity.

5. RADIATIVE COOLING FOR SILICON CONCENTRATING PHOTOVOLTAIC SYSTEMS

5.1 Introduction

Radiative cooling is a passive cooling mechanism that dissipates heat via thermal radiation. For outdoor applications, the cold universe at 3 K can be accessed through the sky as the heat sink if the cooler has thermal emission within the wavelength range of 8-13 μm [84–86]. In this range, known as the atmospheric window, the atmosphere has high transmission allowing transmission of the radiation from the ground. The existence of the atmospheric window makes outdoor radiative cooling a unique passive cooling method that in principle can reach below-ambient temperature. The challenge is therefore to find cooler materials that have strong thermal emittance within 8-13 μm, and much lower thermal emittance outside this window. Fortunately, early works showed that natural bulk materials such as polyvinyl fluoride [85,87], silicon monoxide (SiO) [86] and silicon nitride (Si_3N_4) [88] are suitable for radiative cooling. Composite materials such as SiO_2 and SiC nanoparticles in polyethylene binder [89] were later proposed as alternative cooler materials. Recent progress in nanophotonics allows the emittance spectra of bulk materials to be tailored by photonic crystal structures [90, 91]. It has recently been demonstrated experimentally that nanophotonic coolers can reach below ambient temperatures, even under direct sunlight [92]. When placed in vacuum, such nanophotonic coolers have been shown to reach sub-freezing cooling [93]. More recently, a high-performance metamaterial based radiative cooler has been demonstrated; the researchers conducting the experiment believe that it may be a

[0]The content of this chapter is primarily taken from a published conference proceeding: Y. Sun*, Z. Zhou*, X. Jin, X. Sun, M. A. Alam, and P. Bermel, "Radiative cooling for concentrating photovoltaic systems" *Thermal Radiation Management for Energy Applications*, Vol.10369, p. 103690D, International Society for Optics and Photonics, 2017.

candidate for mass production [94]. Radiative cooling can potentially be applied to address the increasing demands of electronic device cooling. For instance, it has recently been demonstrated that a 2D photonic crystal silica cooler can effectively cool down the bare solar cell underneath [95]. For an optoelectronic device with higher heat loads, known as thermophotovoltaics, radiative cooling with low-iron soda lime 2D photonic crystal cooler was shown to be effective [96]. There are many other outdoor electronics that could benefit from radiative cooling. Thus, it is important to explore the possibility of using radiative cooling as either a major or a complementary cooling method for these applications.

In this chapter, we investigate the application of radiative cooling on high concentration photovoltaic (HCPV) systems. Due to the highly concentrated solar irradiance and strongly temperature dependent photovoltaic (PV) performance, cooling is one of the major challenges in HCPV research [97]. Operating at high temperatures not only reduces the initial solar-to-electricity conversion efficiency, but can also significantly reduce the long-term reliability, which plays a major role in determining the levelized cost of energy for these systems [98]. Most works focus on engineering the heat sink design to enhance convection cooling [99–101]. Although radiative heat transfer has been brought to increased attention recently [97], radiative cooling through the atmospheric window has not been investigated much in the context of HCPV. In this chapter, we consider HCPV systems with parabolic reflectors concentrating the sunlight, with the PV module facing toward the ground. We show that a transparent dielectric radiative cooler, referred to as the multi-layer low-iron soda lime glass cooler, on the backside of the PV module can have effective cooling without using more area than the PV module and the concentrator optics. The performance of the HCPV system with radiative cooling is assessed by a realistic calculation framework. Details of the framework will be introduced in Section 5.2. In Section 5.3, the radiative cooler design will be discussed, followed by the calculation results. The proposed cooler will then be compared with a conventional flat copper cooler. To compare the

two coolers quantitatively, we introduce a figure of merit, cooling power per weight, which captures both the capability of heat dissipation and the weight of the cooler.

5.2 Calculation Framework

To fully assess the radiative cooling effect on HCPV systems, we establish an optical-thermal-electrical coupled simulation framework based on power balance to self-consistently find the equilibrium temperature of the HCPV system. As depicted in Fig. 5.1, the entire HCPV setup consists of three major parts: a radiative cooler on top facing towards the sky, a parabolic reflector at the bottom near the ground that reflects and concentrates sunlight, and a silicon-based PV module underneath the radiative cooler that absorbs concentrated sunlight. Compared to III-V multi-junction PV modules, silicon-based PV modules may not be as efficient at high concentrations (>100 suns) because of Auger recombination [102]; thus, using models developed for the former may undervalue the value of radiative cooling. In future work, the PV model will be adjusted to predict electric output power and the resulting radiative cooling more precisely at high concentrations. Nonetheless, if we consider the radiative cooler and PV module as a whole, a power balance equation governs the heat transfer inflow and outflow of the system in steady state, which is as follows:

$$P_{in}^{PV} + P_{in}^{cool} = P_{out}^{PV} + P_{out}^{cool} + P_{non-rad}^{PV,cool}; \tag{5.1}$$

where P_{in}^{PV} is the total absorbed radiative power by the PV module; P_{in}^{cool} is the total absorbed radiative power by the radiative cooler; P_{out}^{PV} is the radiative and electrical output power from the PV module; P_{out}^{cool} is the total power radiated out from the cooler and $P_{non-rad}^{PV,cool}$ denotes non-radiative heat transfer. The power balance equation, Eq. 5.1, is similar to the one used in [96], but is modified to include double-side radiation from the cooler and a realistic silicon-based PV module.

The total absorbed radiative power by the PV module has three contributions: (1) the solar power absorbed by the PV module P_{sun}^{PV}, (2) the multiple bounces of thermal radiation from PV module and back onto PV module again P_{rad-PV}^{PV}, and (3)

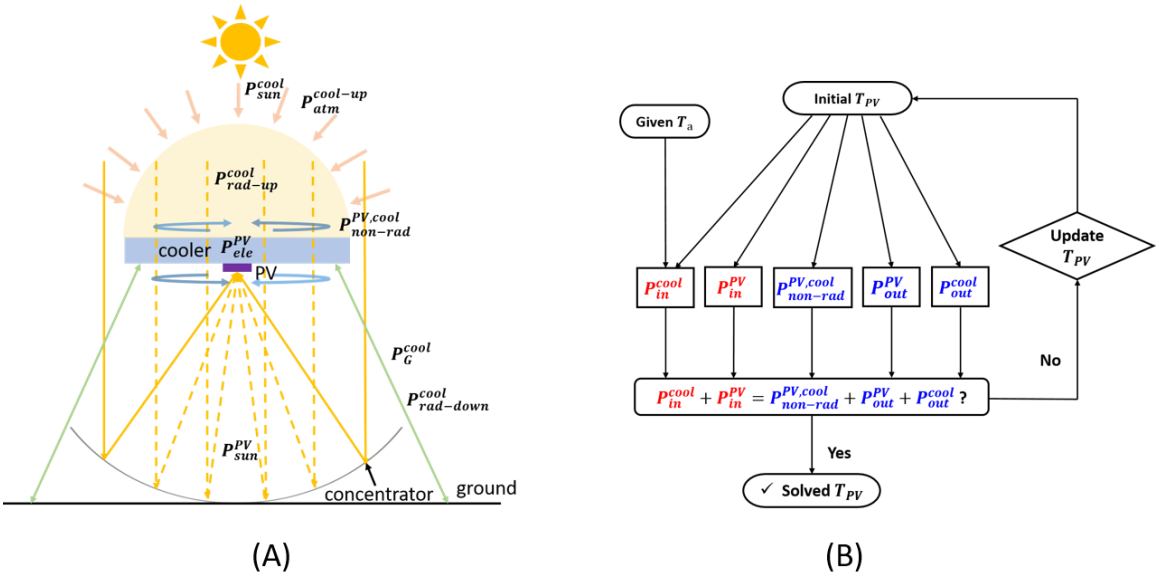

Fig. 5.1.: (A). Schematic of a high-concentration photovoltaic (HCPV) system with radiative cooling. The HCPV has a parabolic reflector as the concentrator. The radiative cooler is on the back side of the PV module and has thermal radiation on both sides. The high solar spectrum transmission of the multi-layer low-iron soda lime glass cooler allows the concentrator right beneath the cooler to collect the AM1.5D sunlight (dashed yellow lines) with little loss. The cooler and the PV module are assumed to be away from the concentrator so that the view factor from the cooler to the concentrator is 0.1. Dominant heat transfer terms are labeled and their explanations can be found in the text. (B). Overall flowchart to explain how the optical-electrical-thermal coupled simulation framework can find the equilibrium temperature of PV module precisely and self-consistently.

the emission from the parabolic reflector absorbed by the PV module P_R^{PV}. Thus, the expression of P_{in}^{PV} is given as follows:

$$P_{in}^{PV} = P_{sun}^{PV} + P_{rad-PV}^{PV} + P_R^{PV}; \tag{5.2}$$

Since the thermal radiation of PV module under the range of temperature considered in this work is low and the view factor from the reflector to the module is close to zero, the latter two terms in Eq. 5.2 are negligible. While P_{sun}^{PV} can be expressed as:

$$P_{sun}^{PV} = C \cdot \rho_R \cdot A_{PV} \cdot \int d\lambda \varepsilon_{PV}(\lambda)[\frac{A_{cool} - A_{PV}}{A_R - A_{PV}} \tau_{cool}(\lambda, 0) + \ldots \\ \ldots (1 - \frac{A_{cool} - A_{PV}}{A_R - A_{PV}})] I_{AM1.5D}(\lambda); \quad (5.3)$$

in which C is the nominal concentration factor determined by the area ratio of the concentrator footprint and the module; $\mathrm{I_{AM1.5D}}(\lambda)$ is the AM1.5D spectrum; The actual concentration factor can be derived as $C_{actual} = C \cdot \rho_R \cdot [\frac{A_{cool} - A_{PV}}{A_R - A_{PV}} \tau_{cool}(\lambda, 0) + (1 - \frac{A_{cool} - A_{PV}}{A_R - A_{PV}})]$; $\rho_R = 0.9$ is the reflectivity of the parabolic reflector; A_{cool} is the surface area of the radiative cooler; $\mathrm{A_{PV}} = 1\ \mathrm{cm}^2$ is the PV module area; A_R is the footprint area of the parabolic reflector; $\varepsilon_{PV}(\lambda)$ is the spectral dependent PV module emittance and $\tau_{cool}(\lambda, 0)$ represents the transmittance spectrum of the radiative cooler at normal incident angle.

The power output from the PV module P_{out}^{PV} is comprised of two terms P_{ele}^{PV} and P_{rad}^{PV} as Eq.5.4:

$$P_{out}^{PV} = P_{ele}^{PV} + P_{rad}^{PV}; \quad (5.4)$$

$$P_{ele}^{PV} = \eta(C_{actual}, T) \cdot C \cdot \rho_R \cdot A_{PV} \cdot \int d\lambda [\frac{A_{cool} - A_{PV}}{A_R - A_{PV}} \tau_{cool}(\lambda, 0) + \ldots \\ \ldots (1 - \frac{A_{cool} - A_{PV}}{A_R - A_{PV}})] I_{AM1.5D}(\lambda); \quad (5.5)$$

$$P_{rad}^{PV} = A_{PV} \cdot \int d\Omega \cos\theta \int d\lambda \varepsilon_{PV} I_{BB}(\lambda, T_{PV}); \quad (5.6)$$

The electrical power output is calculated by Eq. 5.5, where $\eta(C_{actual}, \mathrm{T})$ is temperature and concentration factor dependent PV module efficiency. The radiative power output term P_{rad}^{PV} is calculated by Eq. 5.6, where $I_{BB}(\lambda, T) = (2hc^2)/[\lambda^5(\exp(hc/\lambda kT) -$

1)] is the Planck's blackbody radiation function, and T_{PV} is the temperature of the PV module.

However, it is not trivial to accurately predict $\eta(C_{actual}, \mathrm{T})$ for a wide range of concentration factor ($\leq$ 900 suns) and temperature ($\leq$ 550 K). Despite that temperature coefficient of c-Si solar module has been previously reported [98] as $-0.45\%/\mathrm{K}$, the linear relation between η and T cannot hold across all temperatures. As depicted in Fig. 5.2, the η addressed by the temperature coefficient based empirical formula falls linearly with elevated temperature and becomes $\eta < 0\%$ beyond $\mathrm{T} = 520$ K. In reality, at high temperature region ($\mathrm{T} > 500$ K), η saturates with the rise of temperature and never falls beyond 0%. To capture the essential physics, $\eta(C_{actual}, \mathrm{T})$ is attained by

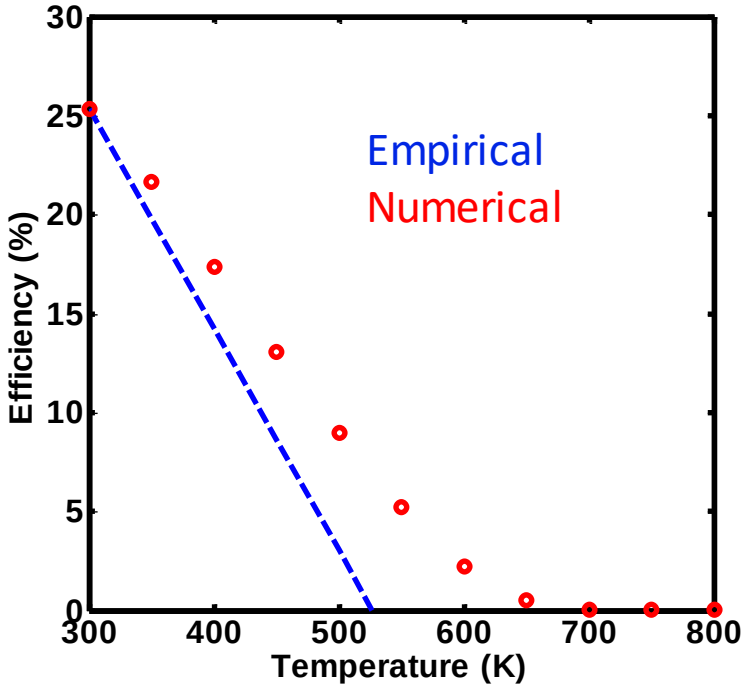

Fig. 5.2.: Schematic of $\eta - \mathrm{T}$ relation addressed by empirical relation with the assumption of constant temperature coefficient $-0.45\%/\mathrm{K}$, and by rigorous device simulation framework

establishing multi-layered device model of Silicon heterojunction with intrinsic thin layer (HIT) solar cell in physics-based drift-diffusion solver TCAD *Sentaurus*. The simulation framework is calibrated against the record efficiency of HIT solar cells at one sun under room temperature (i.e. $\eta(1\ \text{sun}, 300\ \text{K}) = 24.7\%$) [103], and then predicts $\eta(C_{actual}, \text{T})$ by varying device operating temperature and concentration factor. Results are shown in Fig. 5.3. For the radiative cooler, the total absorbed power P_{in}^{cool} can be expanded into four terms, as follows:

$$P_{in}^{cool} = P_{atm}^{cool-up} + P_{sun}^{cool} + P_{G}^{cool} + P_{rad-PV}^{cool}; \tag{5.7}$$

$$P_{atm}^{cool-up} = A_{cool} \cdot \int d\Omega \cos\theta \int d\lambda \varepsilon_{cool}(\lambda, \theta) \varepsilon_{atm}(\lambda, \theta) I_{BB}(\lambda, T_a); \tag{5.8}$$

$$P_{sun}^{cool} = A_{cool} \cdot \int d\lambda \varepsilon_{cool}(\lambda, 0) I_{AM1.5G}(\lambda); \tag{5.9}$$

$$P_{G}^{cool} = (A_{cool} - A_{PV}) \cdot F_{cool-G} \cdot \varepsilon_{G} \cdot \int d\Omega \cos\theta \int d\lambda I_{BB}(\lambda, T_a) \varepsilon_{cool}^{'}(\lambda, \theta); \tag{5.10}$$

where $P_{atm}^{cool-up}$, calculated by Eq. 5.8, is the atmospheric radiation absorbed by the top surface of the cooler, in which $\varepsilon_{cool}(\lambda, \theta)$ and $\varepsilon_{atm}(\lambda, \theta)$ are spectral and angular dependent emittance of the top surface of radiative cooler and atmosphere, respectively. $\varepsilon_{atm}(\lambda, \theta)$ is calculated by MODTRAN (Mid-latitude winter) atmospheric transmittance data $\tau_{atm}(\lambda, 0)$ with angular modulation: $\varepsilon_{atm}(\lambda, \theta) = 1 - \tau_{atm}(\lambda, 0)^{1/\cos\theta}$ [86]; $T_a = 293.15$ K is the ambient temperature [97]. P_{sun}^{cool}, calculated by Eq. 5.9, is the solar power absorption by the radiative cooler. It should be noted that the solar irradiance used for this term should be the AM1.5G spectrum. P_{G}^{cool}, calculated by Eq. 5.10, is the ground emission absorbed by the bottom surface of the radiative cooler, in which F_{cool-G} is the view factor from the radiative cooler to ground and is assumed to be 0.9; ε_G is the ground emissivity, calculated from a diffusive ground albedo presumed to be 0.1, a common value for soil [104]; $\varepsilon_{cool}^{'}(\lambda, \theta)$ is the emittance of the bottom surface of the radiative cooler. The last term in Eq. 5.7 can be neglected,

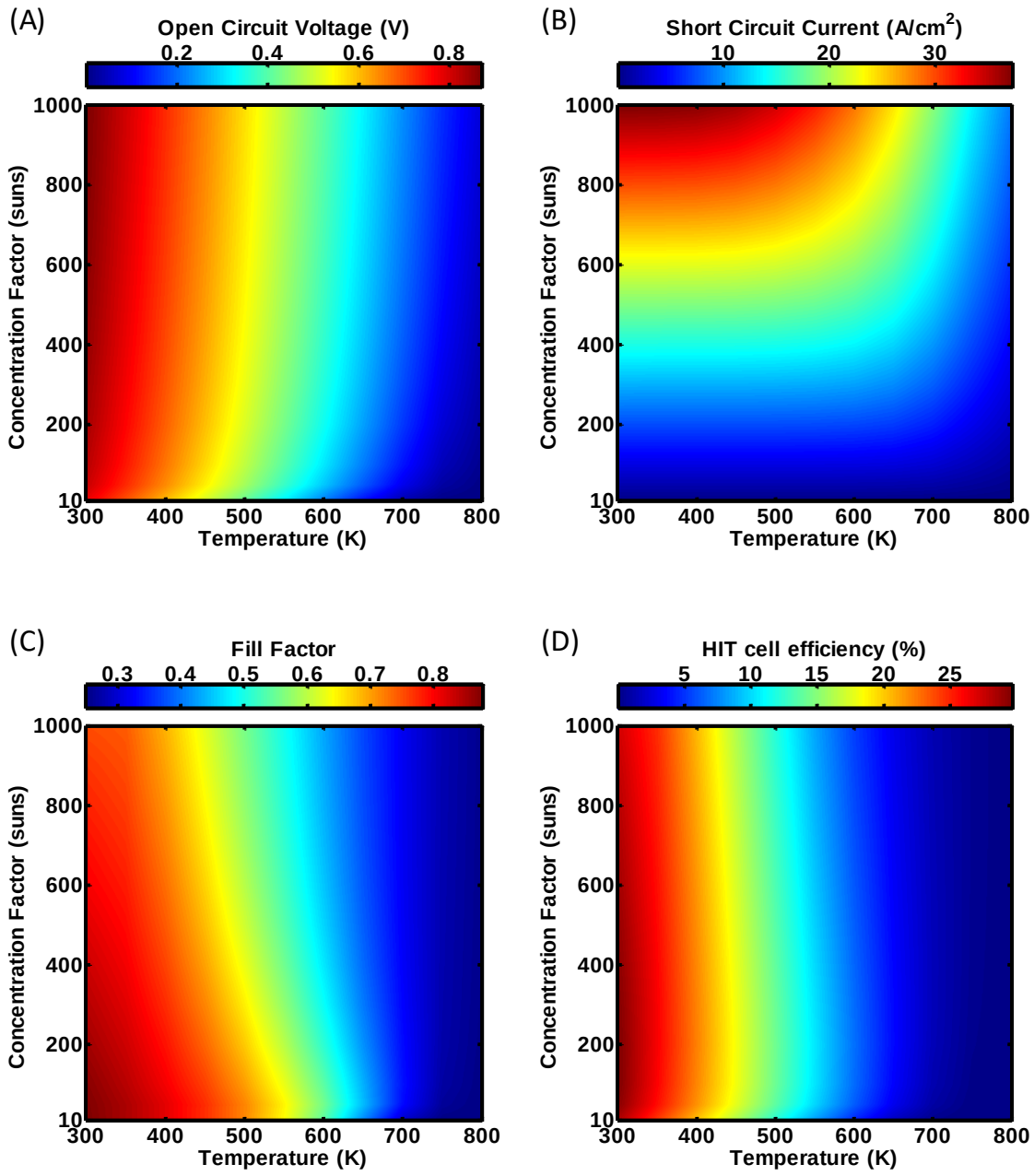

Fig. 5.3.: Schematics of temperature and concentration factor dependence for key solar cell metrics attained from device simulation: (A). Open circuit voltage; (B). Short circuit current; (C). Fill Factor; (D). HIT cell efficiency.

since the PV module and the cooler are close to thermal equilibrium.

The thermal radiation outflow from the cooler P_{out}^{cool} is composed of two terms, namely the upward and downward thermal radiation P_{rad-up}^{cool} and $P_{rad-down}^{cool}$, given below:

$$P_{out}^{cool} = P_{rad-up}^{cool} + P_{rad-down}^{cool}; \tag{5.11}$$

$$P_{rad-up}^{cool} = A_{cool} \cdot \int d\Omega \cos\theta \int d\lambda \varepsilon_{cool}(\lambda, \theta) I_{BB}(\lambda, T_{cool}); \tag{5.12}$$

$$P_{rad-down}^{cool} = (A_{cool} - A_{PV}) \cdot F_{cool-G} \cdot \varepsilon_G \cdot \int d\Omega \cos\theta \int d\lambda \varepsilon_{cool}^{'}(\lambda, \theta) I_{BB}(\lambda, T_{cool}) \tag{5.13}$$

In both equations above, T_{cool} is the cooler temperature.

The aforementioned non-radiative heat transfer term of the system $P_{non-rad}^{PV,cool}$ is simply the convective heat transfer at the top and bottom surfaces, with uniform temperature assumed between the cooler and PV modules (i.e., $T_{cool} = T_{PV}$):

$$P_{non-rad}^{PV,cool} = 2 \cdot h \cdot A_{cool}(T_{PV} - T_a); \tag{5.14}$$

where the convection coefficient $h = 5$ W/m^{2}K [97].

The overall scheme of the simulation framework is illustrated in Fig. 5.1. To solve the equilibrium temperature of the PV module, we begin by guessing the initial temperature of the PV module (T_{PV}) and calculating the power flow of each corresponding heat transfer terms to validate the power balanced equation Eq. 5.1. If not satisfied, a new T_{PV} will be assigned and tested until it self-consistently concurred with power balanced equation. The calculation framework has been benchmarked against the calculation method in [97], which is also consistent with the experiments presented in [105]. Further validation by an experiment closer to the HCPV system modeled here would be warranted.

5.3 Cooler Design & Results

5.3.1 Cooler Design

Soda lime glass has been proposed as a good radiative cooler material for different applications due to its high mid-IR emittance [96, 106]. A subclass, known as low-iron soda lime glass, has the additional benefit of high solar transmission, allowing daytime radiative cooling even with direct sunlight. However, its emittance spectrum dips near 10 μm. As shown by the green curve in Fig. 5.4, this dip in emittance overlaps with the range of the main atmospheric window from $8 - 13$ μm (shaded blue), making the heat transfer between the cooler and the cold universe suboptimal. To fully utilize the main atmospheric window, the emittance of the low-iron soda lime glass in this range should be enhanced. It has been proposed that 2D photonic crystal structures can substantially enhance the emittance within the atmospheric window close to unity [96]. In this work, similar enhancement has been achieved via a different approach. Since the dip in emittance is caused by high reflection near 10 μm, an anti-reflection (AR) coating applied on top of the low-iron soda lime glass may reduce the reflection. As shown in Fig. 5.4, a 2.28 μm thick porous low-iron soda lime glass on top serves as a broadband AR coating. The dielectric constant ϵ of the porous glass is modeled by Bruggeman approximation [107] as:

$$v_g \frac{\epsilon_g - \epsilon}{\epsilon_g + 2\epsilon} + (1 - v_g) \frac{\epsilon_a - \epsilon}{\epsilon_2 + 2\epsilon} = 0; \tag{5.15}$$

where v_g and ϵ_g are the volume fraction and the dielectric constant for a spectral range of $0.31 - 300$ μm [108] of low-iron soda lime glass, respectively; $\epsilon_a = 1$ is the dielectric constant of the air. In this work, the volume fraction of glass was optimized to be $v_g = 0.25$. Compared with photonic crystal structures, porous AR coating is more feasible for large scale production, using fabrication techniques such as chemical etching and the sol-gel method [109].

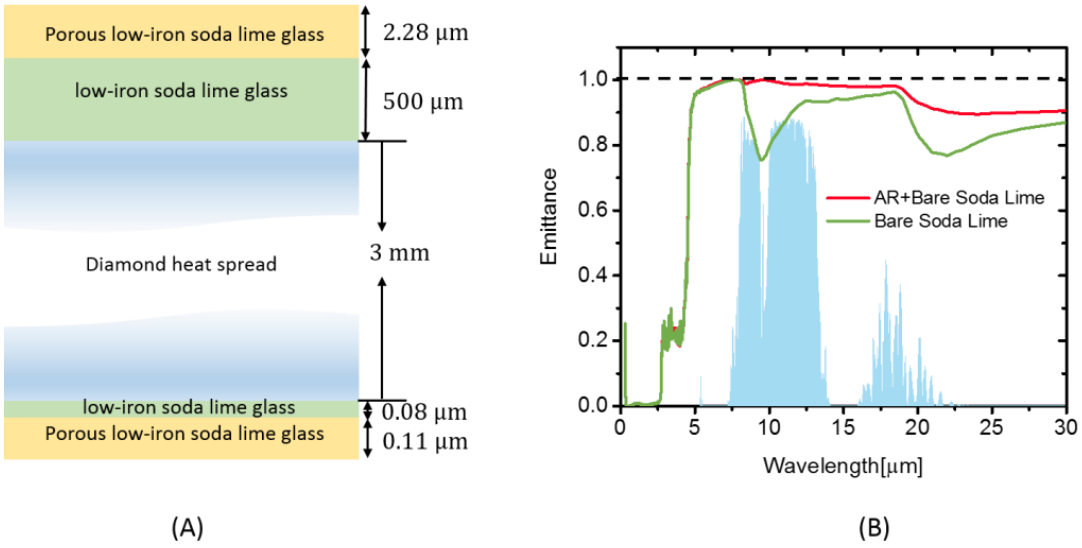

Fig. 5.4.: (A). Cross-sectional schematics of the multi-layer low-iron soda lime glass cooler. The 500 μm thick low-iron soda lime glass serves as the major cooling emitter. The 2.28 μm thick porous layer is a broadband anti-reflection (AR) coating that enhance the mid-IR emittance of the glass. The porous layer has an optimized glass volume faction of 25%. The 3 mm thick diamond layer is the transparent heat spreader that ensures both low non-uniformity in cooler temperature and high solar transmission. The two layers at the bottom is added to further increase the solar transmission of the cooler. The glass volume fraction of the bottom layer is the same as the top layer. (B). The simulated emittance spectrum of the multi-layer low-iron soda lime glass cooler (red) and the cooler without the porous layer (green). The porous low-iron soda lime glass layer can effectively enhance the emittance of the cooler within the $8-13$ μm atmospheric window (shaded blue).

Cooling with a high heat load often requires a larger cooler area than the heat source area (the PV module in HCPV). The geometry depicted in Fig. 5.1 could create non-uniform cooler temperatures over large areas. Thus, the one major assumption made in the calculation framework, $T_{cool} = T_{PV}$, may not be valid in all cases. Therefore, a 3D steady state thermal simulation using COMSOL Multiphysics was

performed to evaluate the temperature gradient of the PV module + cooler structure. As shown in Fig. 5.5, the temperature gradient between the cooler and the PV module ($T_{PV} - T_{cool-ave}$) was calculated for different heat loads ($P_{in}^{PV} - P_{out}^{PV}$) and cooler areas ($A_{cool}$). T_{PV} was directly acquired from the simulation results, and $T_{cool-ave}$ was derived from the radiative power from the cooler surface by Stefan-Boltzmann law. Across the full range of heat loads and cooler areas considered in this work (i.e. below the dashed line in Fig. 5.5), a 3 mm thick diamond layer has a maximum temperature gradient less than 7 K, and usually much less.

Based on this result, a 3 mm thick diamond heat spreader was added at the bottom of the 500 μm-thick low-iron soda lime glass layer. The diamond layer performs two functions: (1) decreasing the radial temperature gradient of the cooler; and (2) maintaining the high solar transmission of the cooler, so that even the concentrator right below the cooler can collect sunlight. The dielectric constant of diamond in the spectral range of $0.31 - 20$ μm is from [110, 111] and was extrapolated as a constant between $20 - 300$ μm to match the spectral range of low iron soda lime glass. The extrapolation may lead to an error of a few percent in the net cooling power from the cooler. It is likely that a 3 mm thick diamond layer is unrealistic for mass production. However, it could be replaced by a thicker layer of other transparent thermal conductors, such as transparent conductive oxides, which can be deposited using roll-to-roll methods, such as knife-over-edge coating, slot-die coating and screen printing [112]. Other materials, such as an optical transmissive and thermally conductive network of metallic nanowires [113], may also be good candidates. To further enhance the solar transmission, two thin layers of low-iron soda lime glass and its porous layer with thicknesses labeled in Fig. 5.4 were also added at the bottom.

The angular-dependent emittance spectra of the multi-layer low-iron soda lime glass cooler was simulated using S4 [114] across a broad range of wavelengths from 0.31 μm to 300 μm. The normal emittance spectrum of the multi-layer low-iron

soda lime glass cooler is shown in Fig. 5.4 in red. Compared with the bare low-iron soda lime cooler (green curve), the multi-layer low-iron soda lime glass cooler exhibits enhanced mid-IR emittance, especially in the atmospheric window. In tandem, the solar absorptance is designed to reach a low level, to allow radiative cooling in direct sunlight.

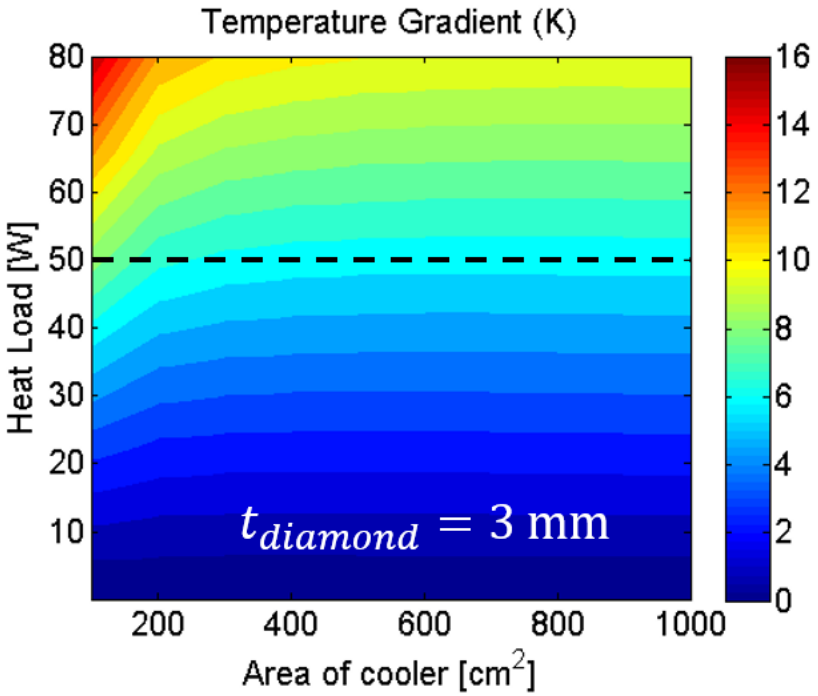

Fig. 5.5.: Steady state temperature gradient between the cooler and the PV module. The cooler temperature is the averaged value calculated from the radiated power by Stefan-Boltzmann law. For a 3 mm thick diamond heat spreader, the maximum temperature gradient is less than 7 K in the range of heat load and cooler area considered in this work (the contour below the black dashed line). Therefore, the approximation of $T_{PV} = T_{cool}$ is valid when a diamond heat spreader of 3 mm thick is used.

5.3.2 Results & Discussion

The performance of the proposed radiative cooler is examined by the calculation framework introduced in Section. 5.2. Fig. 5.6 shows the PV module temperatures are evaluated for different combinations of radiative cooler area A_{cool} and actual concentration factors C_{actual}. Two cases are considered for comparison: (1). a multi-layer low-iron soda lime glass cooler and (2). a conventional copper cooler with its polished highly reflective top surface ($\rho = 0.95$) facing towards the sky, with its emissive oxidized back surface ($\varepsilon = 0.7814$) facing the ground. The front surface of the copper cooler should not be oxidized because its strong solar absorption will more than offset the radiative cooling effect at the target temperature of 60 °C (333.15 K) [97, 115]. For any concentration factor used in the calculation, the radiative cooler is set to be smaller than the concentrator. Therefore, only the lower half of the contour in Fig. 5.6 is calculated. When multi-layer low-iron soda lime glass cooler is used, as shown in Fig. 5.6(A), the PV module temperature T_{PV} goes up as the concentration factor increases, especially when the radiative cooler area is small. However, for larger radiative cooler areas, T_{PV} can reach well below the target temperature – as low as 308 K in the best case. As shown in Fig. 5.6(B), the copper cooler has a higher temperature for the same cooler area and actual concentration factor. The lowest temperature is 322 K, 14 K higher than the multi-layer low-iron soda lime glass cooler. Considering the highest temperature reached by either cooler (indicated by the arrow towards the bottom-right corner of each contour), the multi-layer low-iron soda lime glass cooler performs better as well; the maximum T_{PV} is 73 K lower. In both cases, the target temperature of 333.15 K is highlighted by a dashed line. The better cooling effect of the multi-layer low-iron soda lime glass cooler is also reflected in the more gradual slope of the dashed line, indicating more cooling power per unit area. For concentrating photovoltaics (CPV) applications, especially HCPV, the weight of the cooler is a critical quantity, because a solar tracking system is generally needed [116]. Therefore, we proposed a figure of merit, the cooling power per weight [W/kg], by

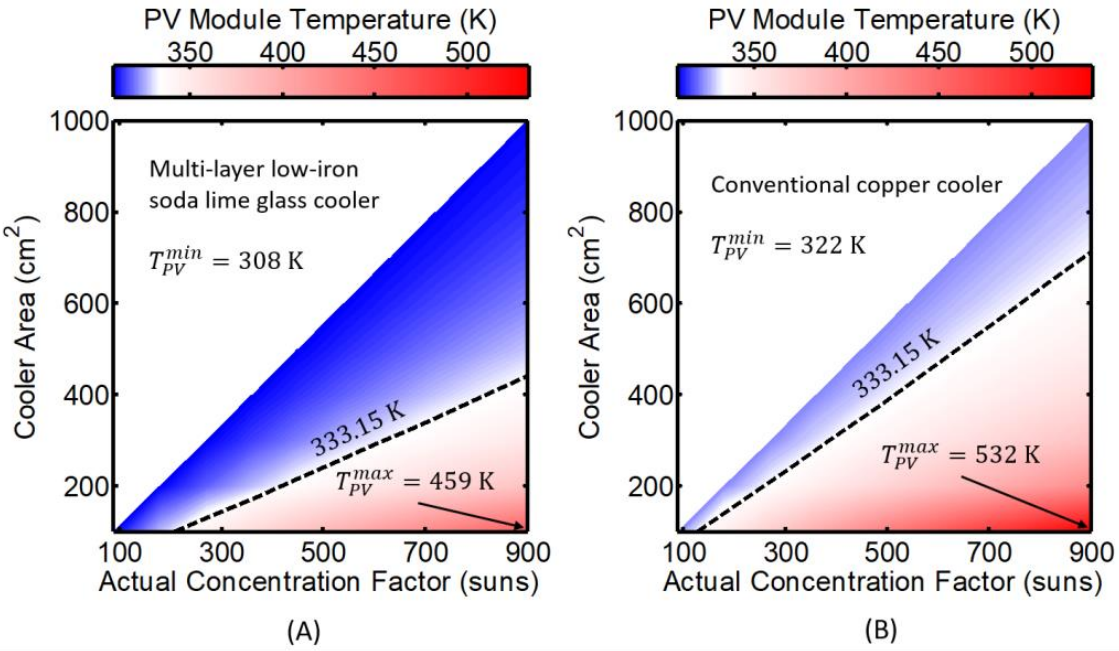

Fig. 5.6.: The simulated contour map of PV module temperature as a function of cooler area and actual concentration factor. The cooler area is always smaller than the concentrator area. (A). Multi-layer low-iron soda lime glass cooler. The minimum temperature it can reach is 308 K and the maximum 459 K. The dashed line shows the cooler area required for the target temperature of 333.15 K at different concentrations. (B). Conventional copper cooler. The minimum temperature it can reach is 322 K and the maximum 532 K. The dashed line shows the cooler area required for the target temperature of 333.15 K at different concentrations. It is obvious that the multi-layer low-iron soda lime glass cooler outperforms the copper cooler. For the same target temperature, less area of multi-layer low-iron soda lime glass cooler is required.

which different coolers can be compared quantitatively. The cooling power is the net output power from the cooler, $P_{out}^{cool} + P_{non-rad}^{PV,cool} - P_{in}^{cool}$, including radiation and convection. For the weight calculation, we assume that the copper cooler has the same

thickness (3 mm) as the diamond heat spreader. The densities of the materials are listed in Table. 5.1.

Table 5.1.: Densities of the Cooler Materials

Material Density [kg/m^3]			
Multi-layer low-iron soda lime glass cooler		Conventional Copper Cooler	
Porous low-iron soda lime glass	633		
Low-iron soda lime glass	2530	Copper	896
Diamond	3510		

For the two different coolers investigated, their weight and cooling power per weight are calculated at different actual concentration factors and PV module temperature of 333.15 K. From Fig. 5.7, it is obvious that the weight of the conventional copper cooler (orange dashed line with triangle symbol) increases faster than the multi-layer low-iron soda lime glass cooler (orange solid line with square symbol). The derived cooling power per weight of each cooler is shown by blue line in Fig. 5.7. The introduced figure of merit clearly has a weak dependence on concentration factors, allowing it to be used as a cooler index applicable for a broad range of concentration. From Fig. 5.7, the cooling power per weight of the multi-layer low-iron soda lime glass cooler (blue solid line with square symbol) is around 3.7 times higher than that of the copper cooler (blue dashed line with triangle symbol), greater than the density ratio of copper to the diamond, due to the capability of radiative cooling under direct sunlight. Therefore, for the same actual concentration factor and target temperature, less weight of the cooler will be added to the solar tracking system if the multi-layer low-iron soda lime glass cooler is used. Aluminum, as another popular material used for HCPV coolers, is in many cases more favorable due to its lower density (2700 kg/m^3) compared with copper. However, the thermal conductivity of aluminum (205 W/mK) is lower than copper as well. Therefore, a thicker aluminum cooler should be used for a flat heat sink to achieve similar temperature uniformity.

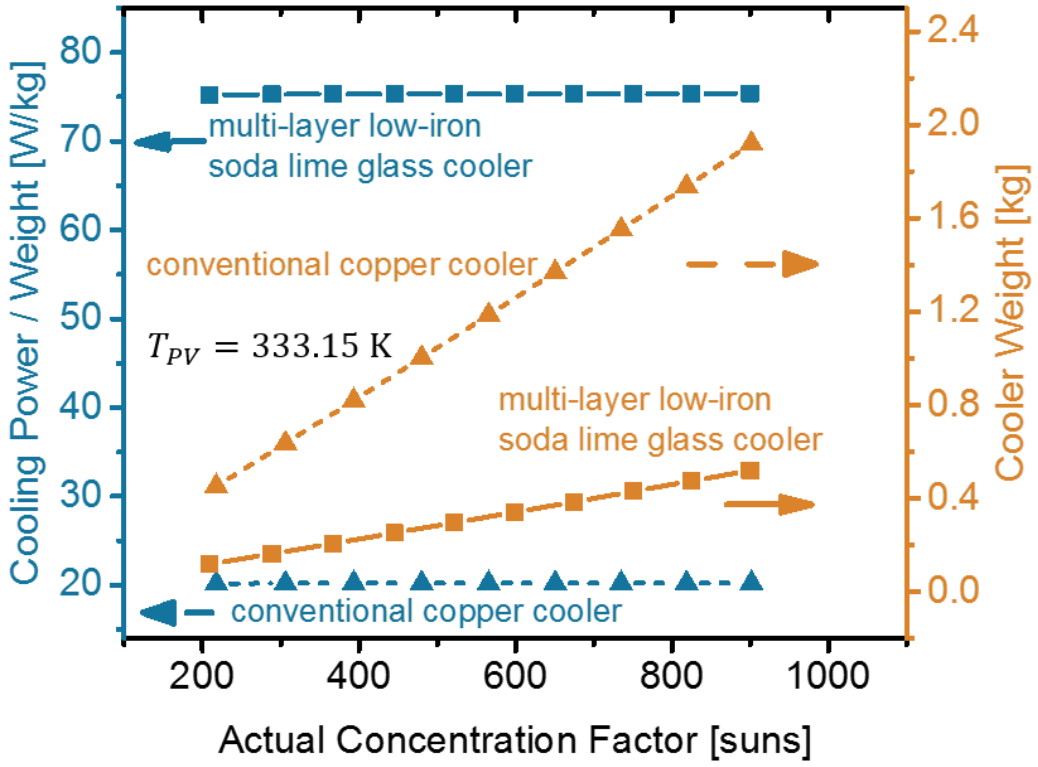

Fig. 5.7.: The figure of merit (blue lines) and cooler weight (orange lines) comparison between the multi-layer low-iron soda lime glass cooler and the conventional copper cooler. The cooling power is the net cooling power (radiation + convection) from the cooler. For copper cooler, the thickness is assumed to be 3 mm thick to match with the diamond heat spreader. The figure of merit is evaluated at the target temperature of 333.15 K [115]. The advantage of the multi-layer low-iron soda lime glass cooler (solid blue line with square symbol) is significant: the cooling power per weight is around 3.7 times higher than that of the copper cooler (dashed blue line with triangle symbol), greater than the density ratio between copper and diamond. Furthermore, much less concentrator area is needed when multi-layer low-iron soda lime glass cooler is used, because of its high solar transmission.

Considering both factors, the cooling power per weight of aluminum cooler should be higher than the copper cooler, but not as high as the multi-layer low-iron soda lime glass cooler when evaluated using the framework introduced in section. 5.2. It should be noted as well that the area of the concentrator is not considered in the figure of merit yet. The fact that copper or aluminum, unlike the multi-layer low-iron soda lime glass cooler, is not transparent to sunlight results in a larger concentrator area to achieve the same amount of actual concentration. This may lead to an even heavier HCPV system to be mounted on the solar tracker. For this work, the focus is on the cooler design. So the quantitative comparison was restricted to the cooler only. But it will be an interesting assessment if the entire HCPV system can be considered in future works.

5.4 Conclusions

The application of radiative cooling within the atmospheric window in the infrared to high-concentration photovoltaic (HCPV) systems has been investigated. Using a realistic, self-consistent simulation framework, a multi-layer low-iron soda lime glass cooler has been designed. Its porous AR coating enhances the mid-IR emittance, allowing radiative cooling under direct sunlight. Furthermore, the proposed cooler is mostly transparent, with high solar transmission. Even a large cooler area blocks very little solar irradiance for concentration. It is shown that a PV module temperature as low as 308 K (about 15 K above ambient) can be reached when the multi-layer low-iron soda lime glass cooler is used, assuming the cooler is no larger than the concentrator. When compared with a conventional copper cooler, it is found that a much smaller area of multi-layer low-iron soda lime glass cooler is now needed to reach the standard HCPV module target temperature of 333.15 K. To account for the weight of the cooler that may affect the solar tracking system, a figure of merit, cooling power per weight, is introduced to evaluate each cooler quantitatively. For all the concentration factors considered (200 to 900 suns) while operating at

the temperature of 333.15 K, the cooling power per weight of the multi-layer low-iron soda lime glass cooler is found to be around 3.7 times higher than that of the conventional copper cooler, and is also expected to be higher than an aluminum cooler. While the initial design uses diamond, there is also potential to shift to lower-cost transparent, thermally-conductive materials. Therefore, radiative cooling has a potential of being applied as a major or complementary cooling method for HCPV systems. Experimental verification would be warranted to help fully confirm the feasibility of low-cost, high performance radiative cooling enabled HCPV systems.

6. OPTIMIZATION OF HIGH-PERFORMANCE *BIFACIAL* INTERDIGITATED BACK CONTACT SILICON HETEROJUNCTION SOLAR CELLS

6.1 Introduction

The energy output of a solar cell depends on both the solar irradiance absorbed via the photovoltaic effect, as well as its efficiency in converting photo-generated carriers into electricity. Traditional *monofacial* cells accept light only from the front surface; therefore, reflection from index mismatch and/or a front-contact metallic grid reduces light coupling into cells. Texturing the front surface and/or including an anti-reflection coating addresses the challenge of index mismatch, while interdigitated back-contact cells (IBC) move both n- and p-type contacts to the back to minimize front-grid light reflection. This improved light coupling allows IBC cells to achieve particularly high power output under typical illumination. By inserting high bandgap (E_g) material between absorber and highly recombination active metal contacts, Silicon heterojunction solar cells (SHJ) [117] can provide higher efficiency ($\eta > 25\%$) and lower temperature coefficients [103] than traditional p-n junction solar cells. Today, despite the fact that recent market forecasts predict the rapid increase in *monofacial* Passivated Emitter and Rear Contact (PERC) cell production [118, 119] *monofacial* IBC-SHJ cells ranks among the very best high-performance cells, with efficiencies exceeding 26% in experiments [120].

A new solar cell architecture, called *bifacial* PV, has recently emerged as a promising technological pathway to higher output yields and lower costs [119,121–124]. The *bifacial* design accepts light from both surfaces, therefore it allows absorption of

[0]The content of this chapter is primarily taken from a published paper: Y. Sun, Z. Zhou, R. Asadpour, M. A. Alam, and P. Bermel, "Tailoring Interdigitated Back Contacts for High-performance *bifacial* Silicon Solar Cells" *Applied Physics Letters*, 114(10), 2019: 103901

ground reflected sunlight (albedo) at the rear side of solar cell. The sum of the direct sunlight and the albedo illumination increases photo-current within the cell. Unfortunately, the benefits of *bifacial* operation of an IBC-SHJ cell are not easily quantified – after all, the dense interdigitated grid in the back may only allow a fraction of the albedo (α) light to reach the cell and the excess photo-current may be lost as Joule heating in the fingers and busbars. Very little previous work has focused on assessing *bifacial* IBC-SHJ cells, which are expected to be optically superior to *bifacial* front and back contact PERC cells at any α. This work is the first to present an experimentally-verified numerical model that precisely quantifies the tradeoff between optical transmission and electrical performance in an improved *bifacial* IBC-SHJ architecture. The compact analytic formula developed in this work and validated against experiment is general enough to encompass the whole class of *bifacial* modules, projected to account of 38% of global installations by 2028 according to ITRPV [118]. It will guide experimentalists and a rapidly growing industry in exploring tradeoffs and design choices such as finger metals, and contact patterns across a range of environmental conditions. Specifically, we show that IBC-SHJ cells benefit from *bifacial* operation provided that: (a) the albedo exceeds a critical intensity, and (b) the gaps between the metal fingers are optimized.

6.2 IBC-SHJ cell Structure

To tackle the back contact design of *bifacial* IBC-SHJ cell, we begin by specifying the details of the device structure. As a reference, we consider a high-efficiency *monofacial* IBC-SHJ cell reported by Yoshikawa et al. [120] with Aluminum (Al) metal grids. Although transparent conducting oxides (TCO) are a theoretically ideal replacement, they are not considered here, since there is not yet an ideal p-type TCO electrode for solar cells [125]. Fig. 6.1(a) shows that our device has a 165 μm n-type c-Si absorber sandwiched between 10 & 20 nm thick intrinsic a-Si passivation layers at front and rear, respectively. Interdigitated p^+ a-Si emitter and n^+ a-Si back-

surface field (BSF) layers are embedded in the rear a-Si passivation layer. The BSF width W_{BSF} and emitter width W_{emit} are taken as 100 μm and 250 μm respectively because: (a). although a wide range of emitter/BSF width ratios yield acceptable power conversion efficiencies [126], *monofacial* IBC cells are typically optimized at $W_{emit} \sim 2 - 3 \times W_{BSF}$; [127–129] and (b). the lateral transport path (center-to-center distance between p^+ and n^+ regions) must be comparable to the absorber thicknesses to avoid excessive bulk recombination. Their spacing is set to $W_S = 5$ μm, because Nichiprouk et al. [129] has emphasized that proximity between the emitter and BSF layers improves device efficiencies. Therefore, the half pitch width W_P (the lateral distance between centers of adjacent metal grids), as labeled in Fig. 6.1(b), is 180 μm. Finally, Al metal grids (thickness of t_{Al}, width of W_{Al} and length of L_{Al} as labeled in Fig. 6.1(a) are pasted to the p^+ emitter and n^+ BSF to form the electrodes.

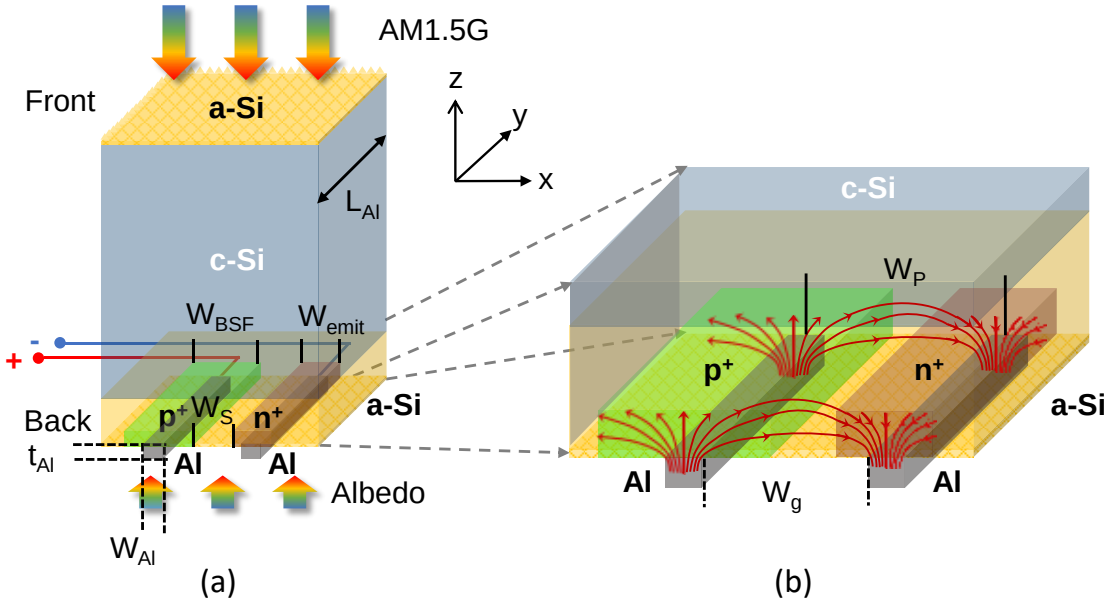

Fig. 6.1.: (a). 3D schematics of the *bifacial* IBC-SHJ solar cell design studied in this work. Key length scales are defined here. (b) Current crowding is induced near the contacts by the narrow overlap between the emitter/BSF and the Al metal grid.

The spacing (gap) between Al metal grids (W_g) is the key variable controlling efficiencies, see Fig. 6.1(b). Once albedo photons transmit through the gap in the metallic back-contact, they generate electron-hole pairs within the device. These photo-generated carriers first transport through emitter/BSF layer to reach the metal contact (intrinsic resistance) and then have to travel through metal fingers and/or busbars to reach the electrode (extrinsic resistance). As a result, thicker gridlines (i.e. narrower W_g) block albedo and reduce photo-current, but thinner lines (i.e. wider W_g) increase series resistance and reduce output power. Specifically, thinner grids (wider W_g) reduce the grid shadowing loss P_{shadow}, but increase the series resistance loss P_{resist}, since $W_{Al} = W_P - W_g$. The resulting output power (P_{OUT}) of a *bifacial* IBC-SHJ cell is given by:

$$P_{OUT}(w, \alpha) = P_{ideal}(\alpha) - P_{resist}(w, \alpha) - P_{shadow}(w, \alpha); \tag{6.1}$$

Here, the idealized intrinsic power-output P_{ideal} of the IBC-SHJ cell is reduced by the counter-balancing resistive and shadowing losses defined by the normalized gap width: $w = W_g/W_P$. Our goal in this chapter will be to calculate the normalized gap width w_{opt} that maximizes $P_{OUT}(w, \alpha)$.

6.3 Numerical Model

Light absorption in a *bifacial* IBC-SHJ cell involves a complex interplay of absorption in the bulk and multiple reflection by the randomly textured surface. Light absorption in a *bifacial* IBC-SHJ cell is calculated first to determine the spatial profile of photo-generated carriers. With texturing on both sides of the cell, ray-tracing calculation may involve complicated 3D simulations [130]. Fortunately, the fact that carrier generation has only weak lateral spatial variation allows us to simplify the optical model to 1D. The effect of a Lambertian light trapping due to random textured surface [131] can be quantified by modifying the spectral dependent optical constant of c-Si based on the empirical formula [132]. In this model, a perfect anti-reflection coating (ARC) layer is assumed. Ray tracing is utilized to compute the absorption

spectrum and spatial optical generation profile within the layered structure. Based on the spatially-resolved light absorption profile, the transport of the photo-generated electrons and holes are solved in a 2D coupled Poisson-drift-diffusion solver *Sentaurus* TCAD [133]. The electrical properties of the interfaces and bulk layers are adapted from previous work [40]. Finally, *Sentaurus* automatically accounts for the intrinsic resistance related to current crowding between the metal and heavily doped regions as illustrated in Fig. 6.1(b). For the extrinsic resistance, the schematic of the IBC back-contacts described by Desa et al. [134] can be used to calculate the corresponding finger and busbar resistances [135,136]: In practice, busbar resistance is negligible compared to finger resistance given by:

$$R_{finger} = \frac{\rho \cdot L_{Al}^2 \cdot W_P}{2 \cdot W_{Al} \cdot t_{Al}}; \tag{6.2}$$

where ρ is the Al resistivity. This extrinsic series resistance associated with Al back-contact is added to the 2D *Sentaurus* device model as an external series resistance.

Our simulation framework is validated by benchmarking against experimental results of a state-of-the-art *monofacial* IBC-SHJ cell [120]. Fig. 6.2 shows that it closely agrees with experimentally observed J-V curves and external quantum efficiency (EQE) spectra. Two non-idealities explain the remaining, small deviations observed: our non-inclusion of the imperfect ARC explains slightly higher EQE between the wavelengths of 300-400 nm, and our neglect of the series resistance explains the slightly higher fill factor (FF). The corrections are small (especially because the back-contact grids can be much wider in their *monofacial* counterparts): the overall discrepancy (in terms of power production) is below 0.5%.

Our simulation framework can now be used to optimize the design of the *bifacial* IBC-SHJ cell shown in Fig. 6.1. Several IBC-SHJ solar cells with a range of W_g values are created in *Sentaurus* and illuminated by various spectral independent albedo α. In general, albedo is wavelength dependent [137]. Nonetheless, in the spectral range where silicon solar cells absorb, a constant value of 0.3 is a good approximation for common surfaces on the earth, such as green grass and construction concrete. Next, following the optoelectronic procedure described above, the output power $P_{OUT}(w, \alpha)$

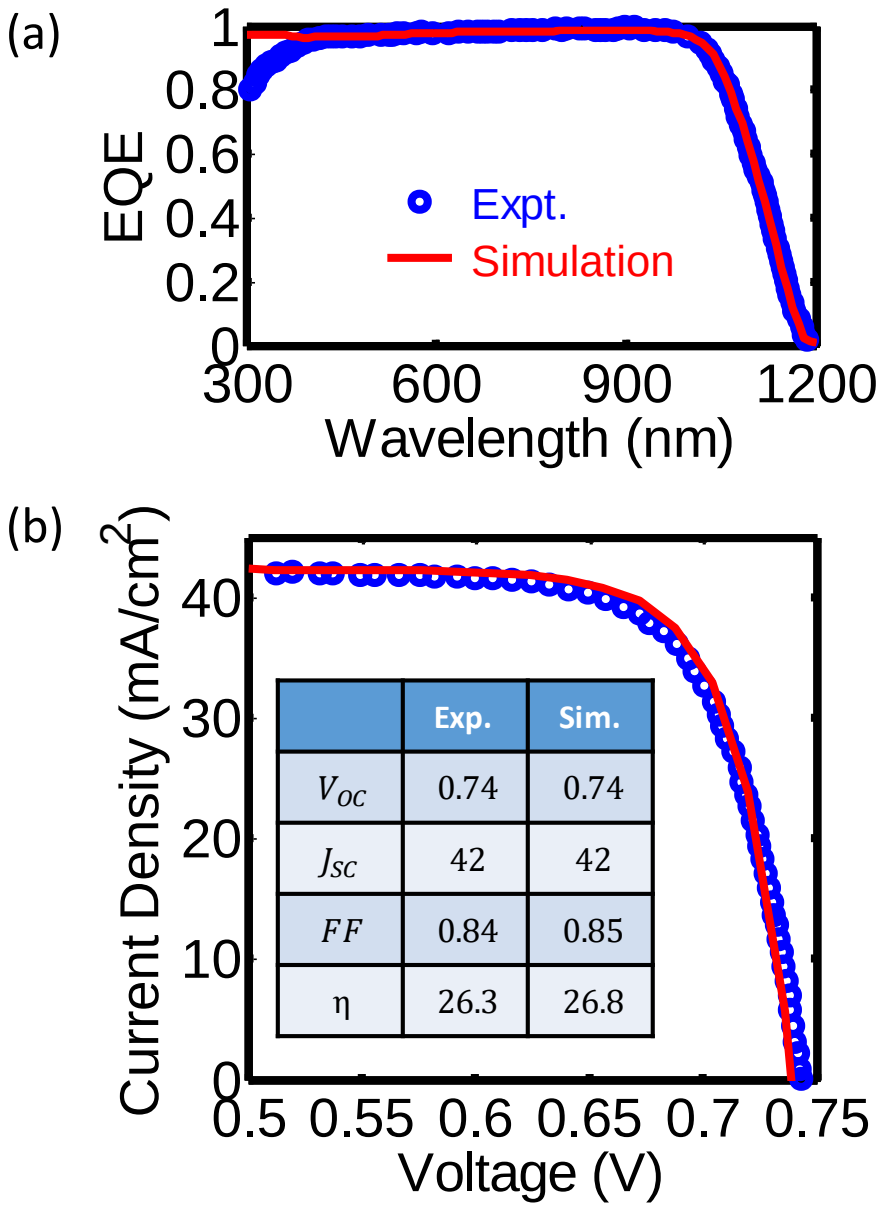

Fig. 6.2.: Our 2-D simulation framework for IBC-SHJ cells incorporating analytic Lambertian light trapping shows strong agreement with (a). spectral dependent EQE results (except for $\lambda < 400$ nm) and (b). measured I-V characteristics adapted from Yoshikawa et al. [120] (dots: experiment; line: simulation).

is calculated. Here, we assume typical finger parameters $t_{Al} = 40$ μm thick [138, 139] and $L_{Al} = 10$ cm long [120, 134]; $W_{Al} = W_P - W_g = W_P \cdot (1 - w)$ is our parameter

for performance optimization of *bifacial* IBC-SHJ solar cells. To quantify shadowing and resistive losses, the results are post-processed, such that the resistive losses due to Al fingers can be extracted from the difference between power output with and without the extrinsic resistance. By definition [51], the power output P_{OUT} of solar cell is given by:

$$P_{OUT} = V_{OC} \cdot J_{SC} \cdot FF; \tag{6.3}$$

where J_{SC} is the short circuit current; V_{OC} is the open circuit voltage; and FF is the fill factor. These four key metrics (V_{OC}, J_{SC}, FF and P_{OUT}) for assessing solar cell performance are plotted as a function of w in Fig. 6.3, J_{SC} is dictated by total amount of sunlight received from front and rear side. It increases linearly with increasing w (see Fig. 6.3(a)), as the gap between the electrodes allows larger fraction of the albedo light to enter the cell and contribute to photo-generation. The loss of FF in Fig. 6.3(b) is a consequence of increasing series resistance with increment of w. Increasing w impacts the series resistance by (1.) reducing the overlap region between metal and emitter/BSF layer to aggravate the current crowding effect; (2). narrowing W_{Al} to increase R_{finger} according to Eq. 6.1 Since V_{OC} scales logarithmically [51] with J_{SC}, the increase in V_{OC} in Fig. 6.3(c) is easily explained. V_{OC} is relatively insensitive to the variation of w, because V_{OC}, as a metric that measures how good carrier transport is within the absorber, is driven by the diffusion length of minority carriers, length of quasi-neutral region and surface defect density etc. [140], none of which is directly correlated to w between Al fingers. Since J_{SC} and FF respond inversely to w, P_{OUT} as a function of w shows a concave downward curve, as shown in Fig. 6.3(d). For increased α, the optimum w that delivers the maximum P_{OUT} shifts to larger values, as summarized in Table 6.1:

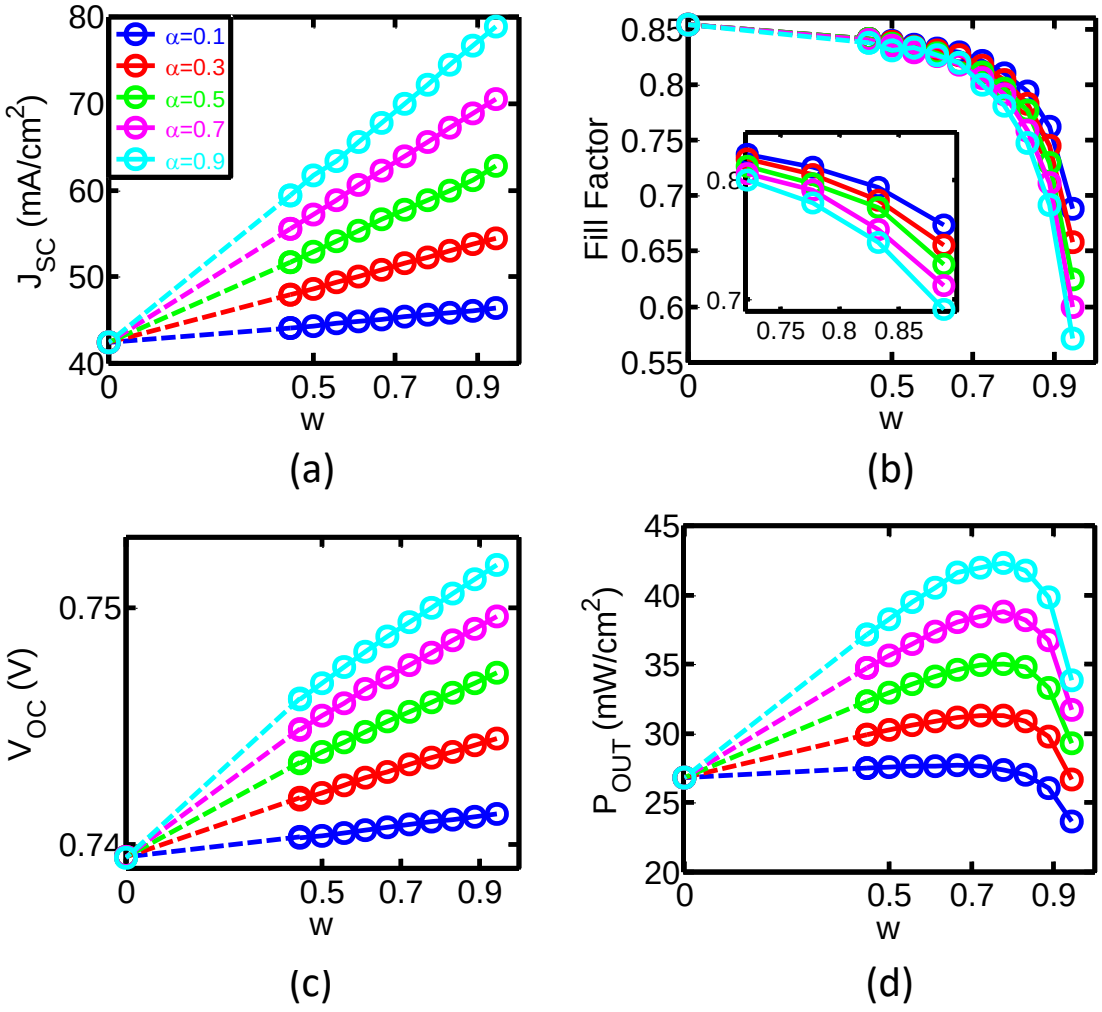

Fig. 6.3.: Performance of the *bifacial* IBC-SHJ cell structure as a function of reduced gap width w between Al metal contacts under various α. (a). short circuit current; (b). fill factor; (c). open circuit voltage; (d). power output. (dots: numerical results; dashed line: trend lines).

Table 6.1.: Optimum w to maximum power output with given α

α	0.1	0.3	0.5	0.7	0.9
w	0.67	0.72	0.78	0.78	0.78
Max. P_{OUT}(mW/cm^2)	27.7	31.3	35.0	38.8	42.3

At $\alpha = 0.3$, total resistive loss and the optical loss of shadowing limit the realistic maximum P_{OUT} at 31.3 mW/cm^2 with a w_{opt} of 0.72, which exceeds P_{OUT} of *monofacial* IBC-SHJ cell by 4.5 mW/cm^2 (17% relative increase). Although the self-shading effect in the monolithic module [141] has not been explicitly accounted for in this work, it can be captured by reducing α. In this case, the improvement of P_{OUT} from *monofacial* IBC-SHJ cell to *bifacial* IBC-SHJ cells is still substantial.

6.4 Analytical Model

The numerical optimization above was performed for a particular IBC-SHJ Al-interconnected cell. Different groups may design *bifacial* IBC cells variously, with different grid periodicity, contact and metal resistances, etc. Therefore a general solution for $w_{opt}(\alpha)$ is desired. To develop this generalization, we first carefully assess the performance of *bifacial* IBC-SHJ cell with $\alpha = 0.3$ by breaking down the loss mechanisms as depicted in Fig. 6.4.

Optical loss of shadowing increased linearly with the decrease of w as it reflects the fact that total amount of absorbed photons scaled linearly with unshaded area. The effective contact resistive loss due to current crowding effect outweighs the finger resistive loss, regardless of w. Remarkably, a generalized analytical expression captures these essential features of power output by realizing $J_{SC}(w, \alpha) \cong J_{SC}(\alpha = 0)\cdot(1+\alpha\cdot w)$. Therefore, Eq. 6.2 can be rewritten as:

$$P_{OUT}(w) \cong P_{OUT,mono} \cdot (1 + \alpha \cdot w) - \frac{1}{2} \cdot L_{Al}^2 \cdot J_{MP,mono}^2 \cdot (1 + \alpha \cdot w)^2 \cdot \frac{\rho}{(1-w) \cdot t_{Al}} \cdots \\ \cdots - J_{MP,mono}^2 \cdot (1 + \alpha \cdot w)^2 \cdot \frac{\rho_c}{(1-w)} \quad (6.4)$$

in which $P_{OUT,mono}$ is the standard output power of a *monofacial* IBC-SHJ solar cell; $J_{MP,mono}$ is the operating current of *monofacial* IBC-SHJ cell at maximum power point; and ρ_c is the contact resistivity between Al grids and heavily doped regions.

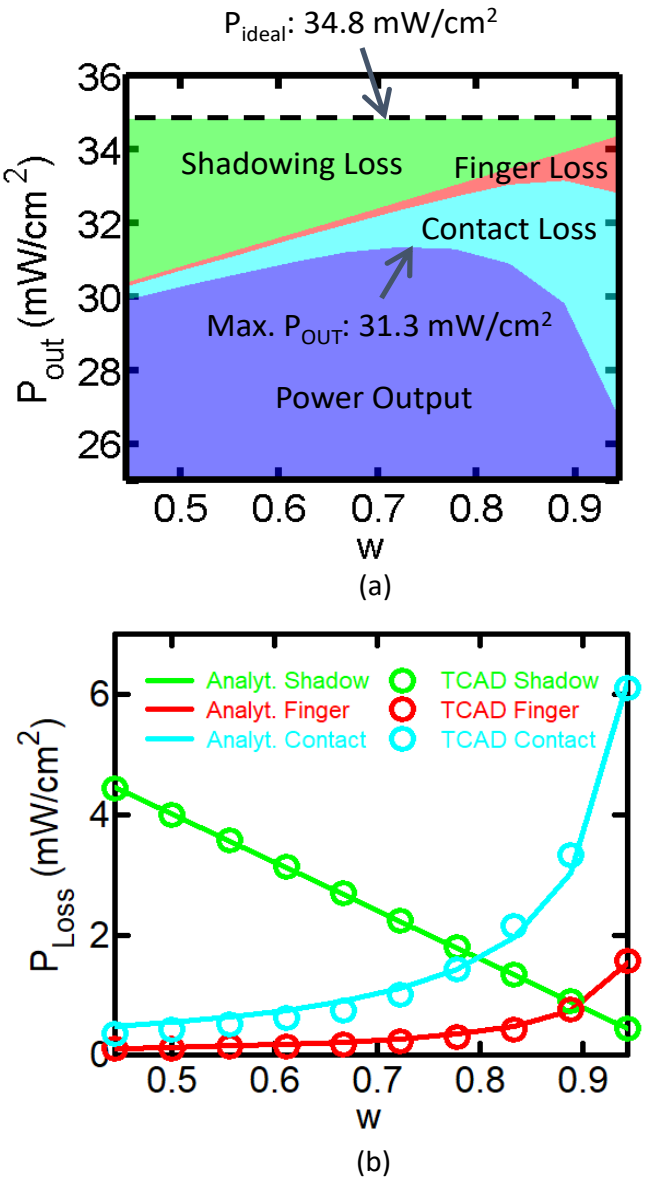

Fig. 6.4.: (a). Illustration of different loss mechanisms (optical loss of shadowing, effective contact resistance loss, finger resistance loss) under various w. (b). Our analytical model (lines) shows strong agreement with simulations (circles) for $\alpha = 0.3$.

To find the normalized gap width w that maximizes $\mathrm{P_{OUT}}$, we set $\frac{d\mathrm{P_{OUT}}}{dw}|_{w=w_{opt}} = 0$; the result for w_{opt} is given by:

$$w_{opt} \equiv \frac{\mathrm{W_g}}{\mathrm{W_P}} = 1 - (1+\alpha)(\alpha \cdot (\alpha + c))^{-\frac{1}{2}}; \tag{6.5}$$

$$c \equiv \frac{\mathrm{P_{OUT,mono}}}{\mathrm{J_{MP,mono}^2} \cdot (\frac{\mathrm{L_{Al}^2} \cdot \rho}{2 \cdot \mathrm{t_{Al}}} + \rho_\mathrm{c})} \tag{6.6}$$

where c captures the ratio of the output power density for the *monofacial* IBC-SHJ cell to the total resistive power loss density. Typically, this should greatly exceed unity in a good cell. At $\alpha = 0.3$, the analytic solution is benchmarked against simulation results. Strong agreement is observed in Fig. 6.4(b). For various α, the analytically-calculated w matches with the numerical simulation within discretization error. By inserting Eq. 6.5 & 6.6 into Eq. 6.4, the benefit of *bifacial* cell over *monofacial* cell can be quantified as a function of α and c, and further simplified for ($\alpha \ll c$) as follows:

$$\frac{\mathrm{P_{OUT}}}{\mathrm{P_{OUT,mono}}} = \frac{1+\alpha}{c} \cdot [c + 2\alpha - 2\sqrt{\alpha(\alpha + c)}] \cong (1+\alpha)(1 - 2\sqrt{\frac{\alpha}{c}}) \tag{6.7}$$

The optimum power scales linearly with albedo (i.e. $1 + \alpha$), although the geometric mean of albedo and the relative loss coefficient (i.e. $\sqrt{\alpha/c}$) suppresses some optical gain. The generalized analytic expression allows one to simply estimate the optimum w and resulting benefit of a *bifacial* cell over a *monofacial* cell in the best case. Interestingly, Eq. 6.4 also offers an insight not immediately apparent from our numerical simulations. By definition, $w \geq 0$, therefore Eq. 6.4 suggests that the albedo must exceed a critical value ($\alpha > \alpha_c$) to ensure that *bifacial* operation actually produced more power than its *monofacial* counterpart. By replacing α by α_c, and setting $w_{opt} = 0$, we find that $\alpha_c = 1/(c-2)$. Recall that for high quality solar cells, resistive power loss is a small fraction of the total power output, therefore c is much greater than 2 and α_c turns out to be very close to zero. For this specific numerical example, $w_{opt} = 0$ is reached when the critical albedo $\alpha_c \leq 0.01$, implying that this *bifacial* cell only outperforms its *monofacial* counterparts when albedo $\alpha > \alpha_c = 0.01$.

6.5 Conclusions

In summary, we have explored the optimization of back contacted design for bifacial IBC-SHJ solar cell which theoretically outperforms the fast growing PERC

technique as a pathway towards low cost of PV technologies. By incorporating a realistic series resistance model that reflects both extrinsic and intrinsic resistive losses into our well-calibrated 2D electro-optically coupled device simulation framework, we have identified the w_{opt} between Al back contacts for bifacial IBC-SHJ solar cell under various α. For a practical α of 0.3, we find that a bifacial IBC-SHJ cell outperforms monofacial IBC-SHJ cell by 4.5 mW/cm^2 in the best case. Furthermore, a generalized analytical expression addressing the balance of resistive loss and optical loss of shadowing was also derived, which shows that bifacial IBC solar cells offer a significant advantage in power production across a broad range of albedos and materials. As a result, this study may serve as a general guideline for the design and optimization of future bifacial IBC-SHJ solar cells.

7. TAILORING BACK CONTACT DESIGN OF *BIFACIAL* PERC-TYPE CIGS SOLAR CELLS

7.1 Introduction

From chapter 6, we have developed a well-calibrated analytical formula to grasp the optimum design of *bifacial* IBC-SHJ solar cell under various albedo. We now look into generalization the formula to a wide variety of solar absorbers, (i.e. thin-film solar cells). Copper Indium Gallium DiSelenide (CIGS) has been utilized to reach a world-record efficiency of 22.9% as a single junction thin-film PV absorber by Solar Frontier [142] employing a Cd-free buffer layer. Decent mini-module efficiency (18.6%) with massive power production (2 GWp) has already been achieved [143]. Combined, these results indicate that this chalcopyrite compound-based PV technology is highly efficient and scalable. However, the ultimate performance is limited by the Shockley-Queisser limit in this architecture, which is approximately 31% for the AM1.5G solar spectrum. The convergence between realized and theoretical efficiencies in traditional architectures has recently increased interest in new approaches.

To this end, *bifacial* PV recently has emerged as a promising technological pathway towards higher energy yields [119, 121–124, 143] by allowing additional rear absorption of sunlight scattered from ground (albedo). According to the International Technology Roadmap for Photovoltaics (ITRPV) [118], *bifacial* PV will gain 60% PV market share by 2029. There has been some recent research exploring *bifacial* CIGS solar cells. For the sake of allowing rear side absorption, it was initially proposed that conventional Molybdenum (Mo) back contacts should be substituted by transparent

[0]The content of this chapter is primarily taken from a published conference proceeding: Y. Sun, M. A. Alam, and P. Bermel, "A Generalized Analytic Model to Tailor Back Contact Design of *bifacial* PERC-type $Cu(In, Ga)Se_2$ solar cells" *2019 IEEE 46th Photovoltaic Specialists Conference (PVSC)*, Chicago, IL, USA, 2019, pp.3024-3027

conducting oxides (TCO) to enhance the contact transparency. Rostan et al. [144] proposed an AZO/$MoSe_2$ double layer structure as a semi-transparent conducting oxide back contact for CIGS solar cell. Nakada et al. [145] presented comparable device performance between conventional CIGS/Mo and novel CIGS/FTO, CIGS/ITO back contacts. Mazzer et al. [146] optimized deposition of CIGS/FTO and CIGS/ITO back contacts by introducing a single-stage low-temperature pulsed electron deposition (LTPED). Cavallari et al. [147] reported 11.6% efficient *bifacial* CIGS/AZO solar cells. However, extremely low (<0.4) external quantum efficiency (EQE) has been observed in the short wavelength range (400 nm - 700 nm) of measured EQE spectra under rear side illumination for the aforementioned design (CIGS/TCO). Such poor electrical transport behavior can be attributed to poor rear passivation. For conventional *monofacial* CIGS solar cells, rear surface passivation is not of great importance, since the majority of photon absorption occurs near the front side with charge separation assisted by the p-n junction-induced electric field. However, under rear illumination, majority electron-hole pairs will be generated toward the back, causing nearly immediate recombination near a poorly passivated rear surface. To mitigate this effect, a passivated emitter and rear cell (PERC) design that already presents high efficiency and low cost for silicon solar cells is introduced. With the presence of negative fixed charge at interface [148] and an observed reduction of interfacial defects, Aluminum Oxide (Al_2O_3) has been extensively studied by different research groups to demonstrate reduced surface recombination velocity and good passivation effect for p-type Silicon [149] and CIGS [150] absorber. Vermang et. al. [151] studied the application of (Al_2O_3) rear surface passivation layer with nano-scale localized Molybdenum (Mo) point contact in ultra-thin (∼240 nm) *monofacial* CIGS solar cells and quantified performance improvement.

In contrast with the conventional CIGS/TCO designs for *bifacial* CIGS, opening up gaps between Mo back contacts to allow albedo sunlight absorption from the rear side of PERC CIGS solar cell is an alternative approach. However, there has not been any previously published research modeling a *bifacial* PERC-type CIGS solar cell. In

this chapter, we aim to modify a previously-developed analytical model calibrated to TCAD electric transport solver [38] by the present authors [152] for back contact design of *bifacial* IBC-SHJ PV to optimize and forecast the performance of *bifacial* PERC CIGS solar cells.

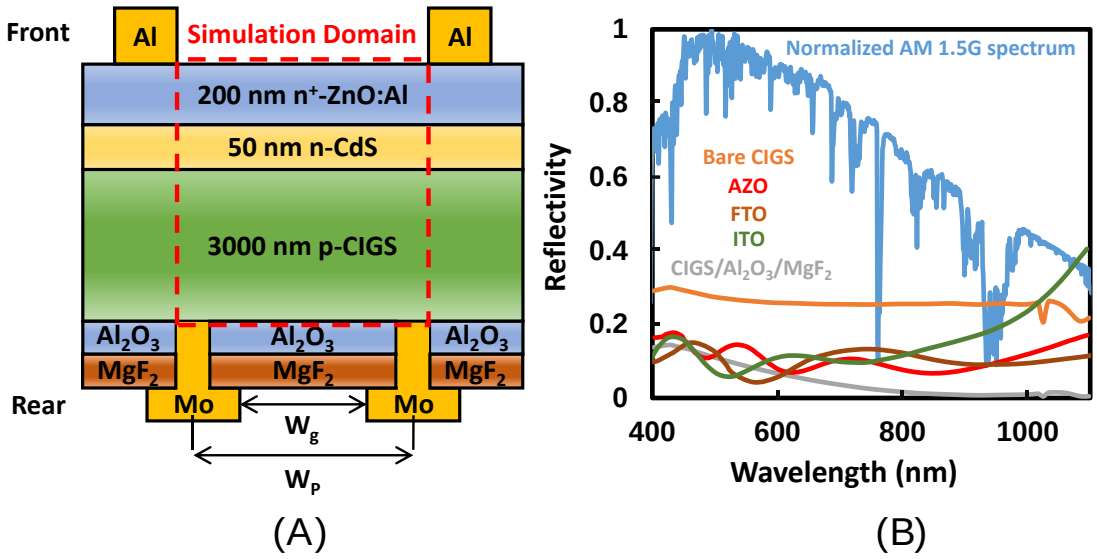

Fig. 7.1.: (A). Cross-section view of *bifacial* PERC CIGS solar cell with pitch width W_P and gap width W_g between Mo back contacts. Red dashed box labels the device simulation domain. (B). S4 optical simulation shows reduced spectral reflectivity in the solar spectrum that CIGS absorbs, by inserting Al_2O_3 passivation layer between CIGS absorber and air.

7.2 Methodology

The cross-sectional view of the standard multi-layered structure of PERC CIGS solar cell architecture is illustrated in Fig. 7.1. A 3000 nm-thick p-CIGS absorber layer is sandwiched between 50 nm n-CdS buffer layer and nano-sized Mo local point contacts surrounded by Al_2O_3/MgF_2 double layer anti-reflective coating stack. A 200 nm n^+-AZO window layer is deposited on top of the CdS buffer and serves as n-type TCO for the cell. At the bottom side of the cell, periodic Mo point contacts

are scaled up to cover larger area of the rear surface to reduce resistive losses. The distance between centers of the Mo point contacts are defined as the pitch width W_P, while the distance between the nearest edge of the Mo contacts are labeled as gap width W_g, and the ratio of these two quantities are defined as normalized gap width: $w = W_g/W_P$. For *bifacial* PV, the presence of reflective Mo at the rear surface will reflect albedo photons, whereas the shrinkage of Mo-covered area results in higher series resistance. Therefore, there exists an optimum w that minimizes the combined opto-electric losses, which has yet to be fully explored.

In Chapter. 6, we developed a generalized analytic expression of w for *bifacial* IBC SHJ solar cell under various albedo condition [152], which is given as follows:

$$P_{OUT}(w) \cong P_{OUT,mono} \cdot (1+\alpha \cdot w) - \frac{1}{2} \cdot L_M^2 \cdot J_{MP,mono}^2 \cdot (1+\alpha \cdot w)^2 \cdot \frac{\rho}{(1-w) \cdot t_M} \cdots \\ \cdots - J_{MP,mono}^2 \cdot (1+\alpha \cdot w)^2 \cdot \frac{\rho_c}{(1-w)} \quad (7.1)$$

where $P_{OUT,mono}$ is the output power for *monofacial* device; α is the albedo factor; $J_{MP,mono}$ is the operating current of *monofacial* device at maximum power point; ρ is the resistivity of metallic contact; t_M is the metallic finger thickness; L_M is the metallic finger length and ρ_c is the contact resistivity at the absorber/metal interface. Unlike IBC SHJ solar cell, this analytic expression of w cannot be simply extended to study *bifacial* PERC CIGS solar cell with following reasons: (1). the efficiency of IBC-SHJ cell under front and rear illumination scales linearly with illumination intensity (albedo factor) with identical scaling factor. Owing to the fact that IBC-SHJ solar cell has highly symmetric structure by utilizing ultrathin a-Si:H as the passivation layer for both front and rear surface, whereas the optical structure of PERC CIGS is completely asymmetric with AZO and Al_2O_3 attached to the front and rear surface respectively; (2). carrier collection in IBC SHJ cell is not very sensitive to the location of p-n junction since the minority carrier diffusion length in crystalline Silicon absorber is magnitude orders greater than the absorber thickness. On the contrary, minority electron diffusion length in p-CIGS is typically very comparable to the CIGS layer thickness. It implies that carrier collection under rear illumination

is not as efficient as that of under front illumination due to the fact that p-n junction is usually placed near the front side. Essentially, Eq. 7.1 has to account for the two aforementioned factors before it can be used to assess *bifacial* PERC CIGS cell performance. We introduced a normalized albedo factor α' to substitute the nominal α that appears in Eq. 7.1 to quantify additional optical and electrical losses arising from rear illumination:

$$\alpha' = \alpha \cdot \eta_{elec} \cdot \eta_{opt} \tag{7.2}$$

in which η_{opt} describes the additional optical loss for light beams entering the Al_2O_3 passivation layer; η_{elec} depicts the electrical loss associated with presence of p-n junction far away from the location where majority optical generation occurs under rear illumination.

Extraction of optical loss parameter η_{opt}. We extract the spectral dispersion relation of CIGS from [153] and establish air/MgF_2/Al_2O_3/CIGS triplet stack in rigorous coupled wave solver S4 [114] to generate spectral reflectivity of this multi-layer structure. Bare CIGS is also studied to show that inclusion of Al_2O_3 layer not only electrically serves as surface passivation layer but also optically superior to common TCOs (i.e. ITO, AZO, FTO etc.) in suppressing the reflection loss, see Fig. 7.1(B).

Extraction of electrical loss parameter η_{elec}. The extraction of η_{opt} requires detailed 1-D device level simulation that can be performed by TCAD drift-diffusion electron transport solver *Sentaurus* TCAD [38] under front and rear illumination condition. As highlighted in red dashed box of Fig. 7.1(A), the electrical simulation domain excludes the MgF_2/Al_2O_3 stack while its passivation effect can be reflected by setting the electron rear surface recombination velocity to a smaller value (i.e. $S_b = 10^3$ cm/s). The electrical properties of AZO/CdS/CIGS within the simulation domain are adapted from [154]. Grain boundary effect [155] in poly-crystalline CIGS solar cell is not considered here. To decouple optical loss quantity η_{opt} from the electrical loss quantity η_{elec} in the optic-electric coupled simulation, front and rear surface are enforced to be perfectly anti-reflective ($R_b = R_f = 0\%$).

7.3 Results & Discussion

The optical loss parameter η_{opt} can be extracted by calculating the spectral weighted average reflectivity (SWR) of CIGS/Al_2O_3/MgF_2/Air multilayer stack from Fig. 7.1(B) over the solar spectrum CIGS solar cell absorbs, given by Eq. 7.3:

$$SWR = \frac{\int_0^{\lambda_{E_g}} I_{AM1.5G}(\lambda) R(\lambda) d\lambda}{\int_0^{\lambda_{E_g}} I_{AM1.5G}(\lambda) d\lambda} \tag{7.3}$$

in which $\lambda_{\text{E}_\text{g}}$ is the wavelength corresponds to the band edge of CIGS absorber; R(λ) is the spectral reflectivity of the CIGS/Al_2O_3/MgF_2/Air multi-layer stack. It is found that 4.6% of incoming light is reflected; thus, η_{opt} is 0.954. On the other hand, extracting the electrical loss parameter η_{elec} is slightly complicated. With aforementioned electrical properties and optical boundary condition, we calculated a 20% efficient CIGS solar cell could be achieved under front side 1-sun illumination. Various illumination intensities were tweaked from 0.1 suns to 1 sun under both front and rear illumination to ensure η_{elec} is independent of illumination condition, see Fig. 7.2(A)-(B).

Finally, η_{elec} is found to be approximately 0.83. Plugging η_{opt} and η_{elec} back into Eq. 7.2, we are able to calculate respective α' for nominal α between 0 and 1. Substituting α by α' in Eq. 7.1, and assuming high quality *monofacial* cell performance with efficiency of 22.3% [156], we can project the *bifacial* $\text{P}_{\text{OUT}}(w)$ for any arbitrary nominal albedo α as shown in Fig. 7.3(A):

We find that the *bifacial* cell efficiency plateaus at a specific w and quickly diminishes as w increases. We find that for a common $\alpha = 0.3$ (i.e. green grass or construction concrete [137]) *bifacial* cell produces 2.4 mW/cm^2 more (relatively 11%) power output than its *monofacial* counterpart when $w = 0.72$. On the other hand, we also investigate the variation of contact resistivity ρ_c that reflects the current crowding effect near the vicinity of Mo point contact. As can be seen from Fig. 7.3(B), if the contact resistivity exceeds 1 $\Omega - \text{cm}^2$, severe current crowding issues will quickly offsets enhancement of the device performance as w increases – thus obviating the benefit of creating a *bifacial* architecture. This finding is consis-

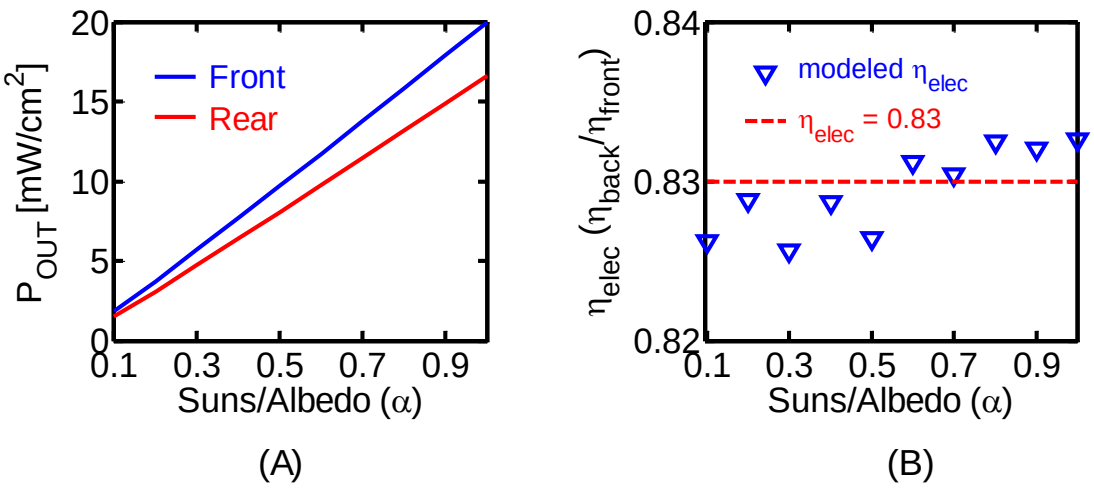

Fig. 7.2.: (A). CIGS cell performance under various front and rear illumination intensities, both efficiencies scale linearly with intensity and rear illumination suffers more from electrical transport loss and thus has a flatter slope (B). Electrical loss parameter η_{elec} is defined as the fraction ratio of rear efficiency to front efficiency and shows weak dependence of illumination intensity.

tent with the experimentally reported range of reasonable contact resistivity values (about $0.08 - 0.2\ \Omega - \text{cm}^2$) [157].

Despite the promising power output gain anticipated by employing the PERC-type *bifacial* CIGS design, this design cannot be immediately commercialized for large scale production from the manufacturing perspective. The gap between Mo back contacts cannot exceed the minority electron diffusion length in p-CIGS absorber (∼1 μm) to maintain good carrier collection efficiency, therefore conventional screen-printed metal deposition technique cannot be implemented here, and instead patterning with expensive photolithography is needed, which may diminish the power output gain for CIGS transitioning from *monofacial* to *bifacial* absorption.

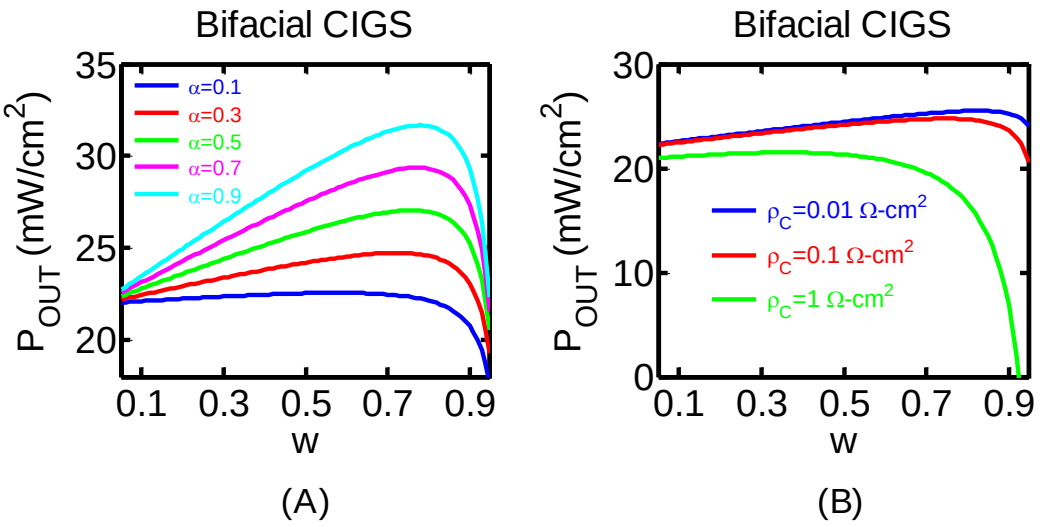

Fig. 7.3.: (A) *bifacial* PERC CIGS cell performance under various nominal α; for a global average $\alpha = 0.3$, *bifacial* cell produces 2.4 mW/cm^2 (relative 11%) more power output than its *monofacial* counterpart; (B) *bifacial* PERC CIGS cell performance under various contact resistivity (ρ_c) which reflects the current crowding near the vicinity of Mo point contacts.

7.4 Conclusions

In this work, we report an alternative approach for *bifacial* CIGS solar cell using a PERC design configuration, rather than the conventional CIGS/TCO design. Through rigorous optical and electrical simulation, we showed that Al_2O_3 can not only passivate the CIGS rear surface, but also suppress reflective loss from rear side illumination. Using a well-calibrated analytic model with nominal albedo α replaced by corrected albedo α' that accounts for additional fractional optical and electrical loss switching from front to rear illumination, we are able to project an additional power output of 2.4 mW/cm^2 for *bifacial* cell above the *monofacial* record efficiency cell, for a normalized gap width w = 0.72 under common albedo $\alpha = 0.3$. Our results can translate to design guidelines for manufacturers to optimize gap/pitch ratio (w) for maximal power output as a function of albedo illumination. Despite the complex-

ity of back contact patterning introduced with the proposed *bifacial* PERC CIGS design, Our results can also be used as an intermediate step to project the levelized cost of energy (LCOE) for *bifacial* CIGS solar cells.

8. REALIZATION OF RAPID SCREENING OF PHOTOVOLTAIC DEVICE PERFORMANCE VIA AN UNSUPERVISED NEURAL NETWORK AUTOENCODER

8.1 Introduction

According to the International Renewable Energy Agency (IRENA), global installed photovoltaics (PV) capacity has steadily risen to 480 GWp (Giga Watt Peak) by the end of 2018 [158], 12 times the installed PV capacity in 2010. With the recent expansion of PV manufacturing and installation, rapid screening and automated detection of PV device performance has become essential to capture quality variations in manufactured PV devices. While this screening can be performed manually, the process can be labor intensive and expensive. As a result, researchers have recently aimed to automatically screen the quality of silicon wafers for their suitability for PV modules [159]. Still, there is a significant scope for more automated tools to further improve quality and reduce costs.

Machine learning, as a subset of artificial intelligence, is a powerful tool with a broad range of applications, which include PV. There are currently three types of PV applications being researched: optimization, prediction and fault detection. For instance, optimization of the performance of PV system through maximum power point (MPP) tracking is achieved using machine-learning based approach [160–163]; Ren et al. [164] demonstrated a Bayesian network approach that optimizes PV device performance by linking the process variables to material descriptors and performance parameters; Cao et al. [165] couples design of experiment and machine learning to demonstrate the process variables optimization for organic photovoltaic devices. Sec-

[0]By the time of thesis deposition, the content of this chapter is primarily taken from an unpublished paper that is currently under review.

ond, machine learning can predict future trends in data through statistical analysis of historical data. Li et al. [166] used Hidden Markov Model and Support-Vector Machine (SVM) to precisely predict short-term future solar irradiance under various weather conditions; Assouline et al. [167] combined SVM and geographic information system to estimate rooftop solar PV potentials in the urban area at the commune level in Switzerland. Third, given large amount of data for training, machine learning can serve as a powerful statistical fault detection tool for PV devices. Buratti, et al. [168] extracted defect parameters using random forest a statistical regression technique to inverse the Shockley-Read-Hall (SRH) equation; Garoudja et al. [169] proposed a probabilistic neural network classifier to detect and diagnose the direct current (DC) side of PV system; and Dhimish et al. [170] attempted to detect and locate different types of PV system faults such as module failures and partial shading through artificial neural network and fuzzy logic systems interfaces. Despite the wide range of applications for machine learning in PV, an automated screening technique for J-V characteristics of manufactured PV devices under standard illumination that leverages new machine learning capabilities has not yet been developed and deployed commercially.

As a new subset of machine-learning based fault detection and characterization, in this chapter, we propose an unsupervised Neural Network Autoencoder (NNA) with K-means clustering to meet the demand of rapid screening and automated detection from PV manufacturers. The neural network autoencoder consists of encoder and decoder that encodes and decodes J-V curves for clustering and validation. J-V curves are encoded in a 2D latent space that serves as a compressed representation of original curves. The K-means algorithm [171], as an unsupervised classification algorithm, with elbow method are utilized to determine the number of clusters and generate the clustering patterns for encoded data in the 2D latent space. The emphasis of this work is on quickness and accuracy of classifying PV cells based on reported J-V characteristics rather than focusing on the process optimization of PV devices [164]. This framework could not only serve as a quality control procedure for PV cells, but

also help create a revised standard operating procedure (SOP) for PV cell quality detection. Moreover, the classification results are tied to specific material descriptors, which could provide PV manufacturers with potential directions for improvement of "failed" PV devices.

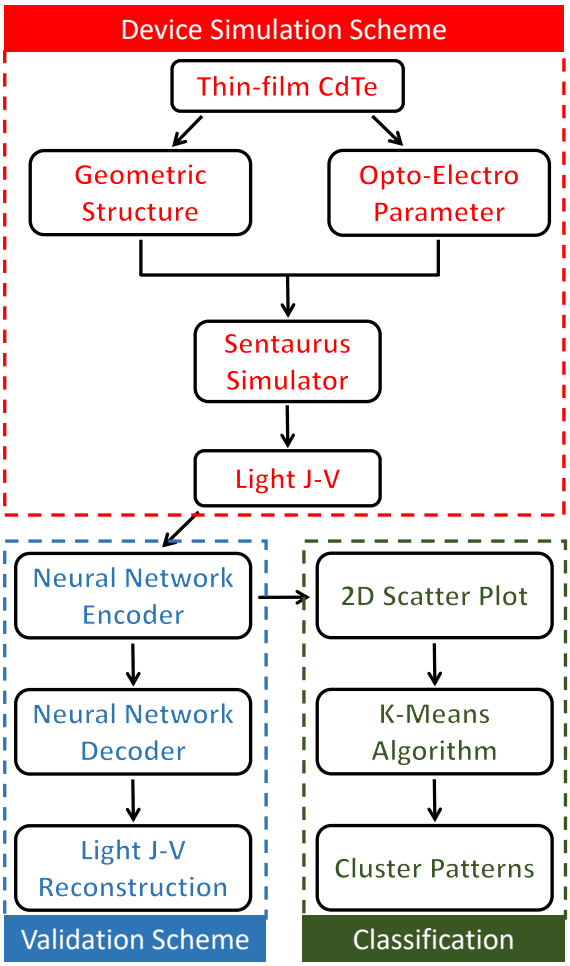

Fig. 8.1.: The computational framework consists of three main components: 1). a device simulation scheme that generates J-V characteristics for validation and classification; 2). a validation scheme that encodes the light J-V in a compressed dimension and decodes to reconstruct the input; and 3). a classification scheme that uses the K-means algorithm to classify clusters for compressed representation of J-V characteristics.

8.2 Methodology

In order to realize the automated quick detection and classification of manufactured PV cells, a machine-learning based framework consisting of three major components is illustrated in Fig. 8.1. The first component, a device simulation scheme, is an important aspect of this framework, since it provides large quantities of light J-V data sets based on varied structural and opto-electric parameters for training, validation and testing. In this case, we consider standard 1-D TCO/CdS/CdTe thin-film solar cells as an example. Baseline layer-by-layer parameters are incorporated from [154]. The thicknesses of the SnO and CdTe absorber layers are fixed at 150 nm and 4 μm, respectively. Variations in the structural and opto-electric parameters are summarized in Table 8.1 below:

Table 8.1.: Summary of Input Parameter Values

T_{CdS} (nm)	N_A (cm^{-3})	ΔE_C (eV)	Φ_B (eV)	FSRV (cm/s)	R_S ($\Omega - cm^2$)	τ_n (ns)
50,	10^{14},	−0.2,	0.1,	10^3,	1,	0.1,
80,	10^{15},	0.2;	0.2,	10^4,	5,	1,
100,	10^{16};		0.3,	10^5;	10;	10,
120,			0.4,			100;
150;			0.5,			
			0.6;			

where T_{CdS} is the CdS layer thickness; N_A is the acceptor doping density of CdTe absorber layer (fully ionized); ΔE_C is the conduction band offset at CdS/CdTe interface [172]; Φ_B is the Schottky barrier height between CdTe and back contact; FSRV is the front CdS/CdTe interface recombination velocity; R_S is the series resistance and τ_n is the minority electron lifetime of CdTe absorber. The device simulation is carried out using *Sentaurus* TCAD [133], a coupled Poisson and drift-diffusion

solver for carrier transport in optoelectronic devices. In accordance with total number of simulated parameter sets, we have a total of 6480 generated J-V curves, out of which 70% are randomly selected as the training set; 20% are categorized as the validation set to provide unbiased evaluation of the model fit on training set; while the remaining 10% are the test dataset. To prove that the framework is practically useful, 31 experimentally reported J-V curves [173–182] of thin film CdTe solar cells are extracted and appended to test dataset.

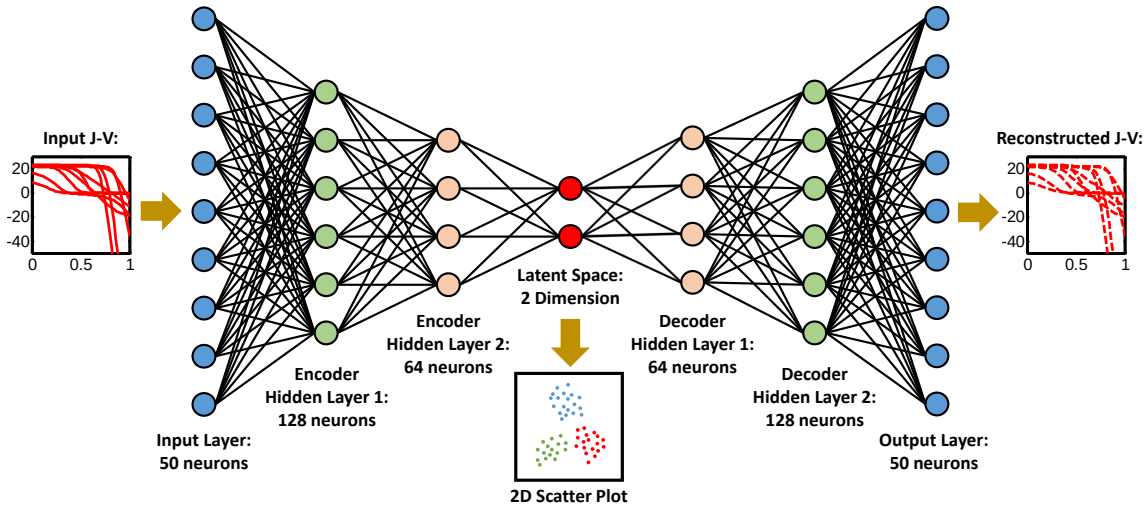

Fig. 8.2.: Schematics of Neural Network Autoencoder (encoder and decoder) for J-V reconstruction and clustering pattern generation. The input J-V characteristics are mapped into the input layer with 50 features (neurons), and encoded in a 2-D latent space. A schematic illustration of the scatter in the latent space is shown as the middle inset. The decoder then decodes the compressed representation in the latent space and reconstruct J-Vs through mirror Neural Network.

The training set is then sent to the Neural Network Autoencoder (NNA) for data compression (encoder) and validation (decoder). The NNA framework is built upon Keras [183], an open-source neural network library written in Python, with core commands adapted and modified from the Keras Blog[1]. As shown in Fig. 8.2,

[1]https://blog.keras.io/building-autoencoders-in-keras.html

the NNA consists of an encoder that compresses input J-V curves into data points of a 2-D latent variable space, and a decoder that is a mirror of the encoder and reconstructs J-V curves from latent space data points. Both the encoder and decoder are composed of two hidden layers with 128 and 64 neurons respectively, activated by "ReLU" (Rectifying Linear Unit), with final output layer activated by "Linear" (Linear Regression). The voltage bias of input J-V curves is confined between 0 and 1 V with an increment step of 0.02 V, thus each training example (J-V curve) has 51 data points (features). The loss of reconstruction is defined as the "mse" (mean squared error) between reconstructed J-Vs and input J-Vs, and is minimized during training through Adaptive Moment Estimation known as "ADAM" [184] - a gradient descent algorithm that computes adaptive learning rate for each parameter.

Before training the NNA, there are two concerns that need to be addressed: 1). Assuming that the operational region of solar cells is in the first quadrant, light J-V curves decrease non-strictly monotonically with increases in the voltage bias. The NNA is not aware of the non-strict monotonicity of trained J-V curves, and as such, it may produce an unphysical J-V reconstruction at the output layer. To mitigate this effect, instead of direct training of the input J-V curves, we trained the current density difference between adjacent biases as shown in Eq. 8.1:

$$\Delta J_i^m = J_i^m - J_{i+1}^m, \tag{8.1}$$

in which i is an integer between 1 and 50 representing the i^{th} feature in the training set, m is the index number of training examples and $\mathrm{J_i^m}$ is the current density of the m^{th} J-V curve at the voltage bias of $(i-1)\cdot 0.02$ V. Since the input training matrix contains none-negative elements in it, no negative elements in the reconstructed matrix are also expected; 2). Another aspect of the training set is that $\Delta\mathrm{J_i^m}$ spans over a wide range of positive values as $\Delta\mathrm{J_i^m}$ remains small near $\mathrm{J_{SC}^m}$, while increasing drastically near $\mathrm{V_{OC}^m}$ for fractional J-V curves. Thus, feature scaling of ΔJ-V is essential to

ensure faster convergence of the gradient descent algorithm. Max-min normalization is applied in this case to scale ΔJ in the range of $[0, 1]$:

$$\Delta J_i^{m\prime} = \frac{\Delta J_i^m - min(\Delta J_i)}{max(\Delta J_i) - min(\Delta J_i)} \tag{8.2}$$

where $\min(\Delta J_i)$ and $\max(\Delta J_i)$ are the global minima and maxima of ΔJ_i across all training examples.

Once the NNA is trained, testing dataset (648 simulated J-Vs + 31 experimental J-Vs) are thrown into the framework to generate 2-D compressed representations of the input. To realize the rapid screening and classification, the elbow method [185] is utilized to determine the optimal number of clusters (K value) for 2-D scattered data in latent space. After K is chosen, K-means algorithm [171] is implemented to select the cluster that each data point belongs to. To clearly distinguish between the J-Vs in each clusters, cluster centroids are computed and processed in decoder to generate respective ΔJ'-Vs. Reconstruction of centroid-based J-Vs can be completed following Eq. 8.3:

$$\begin{cases} J_i = \frac{\sum_{k=1}^{n} J_1^{(k)}}{n}; & (i = 1) \\ J_i = J_1 - \sum_{k=1}^{i-1} \Delta J_k{}' \cdot [max(\Delta J_k) - min(\Delta J_k)] + min(\Delta J_k); & (i \geq 2) \end{cases}, \tag{8.3}$$

where n denotes the total number of data points in the latent space that belong to one cluster. Since the reconstruction at the output layer only predicts ΔJ, J_1 (equivalently J_{SC}) of centroid-based J-V is computed by averaging over the J_1 of J-V curves in the same cluster. Each subsequent current density at non-zero voltage bias can be obtained by subtracting the summation of ΔJ between adjacent voltage biases from J_1. To bridge the connection between the NNA generated clustering patterns and input parameters of solar device simulation, the color map of the data points in 2-D intermediate latent space generated from simulated J-V curves is developed, in which color code labels various parameter values.

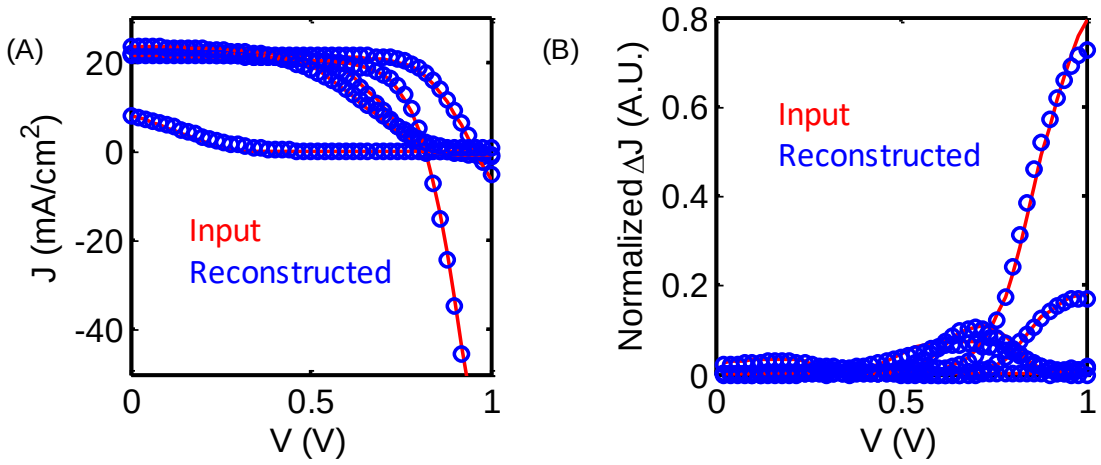

Fig. 8.3.: Reconstruction of J-V characteristics randomly selected from the neural network autoencoder: (A). Reconstructed J-Vs (blue dots) show good agreement with the original J-Vs (red lines) across a wide range of values; (B). Reconstruction of the normalized $\Delta J'$ between adjacent voltage bias points ($\Delta V = 0.02$ V).

8.3 Results & Discussion

The reconstructed test J-Vs from the trained NNA framework are benchmarked against input test J-Vs to validate the training outcome. For the sake of clarity and simplicity, instead of plotting full set of test J-Vs, five J-Vs are randomly selected out of the 648 simulated test J-Vs for demonstration. As shown in Figs. 8.3(A)&(B), reconstructed J-Vs show good agreement with input J-Vs despite that selected J-Vs vary substantially due to different input parameter values.

With the validation of trained NNA framework, 2-D scatter plot of encoded representation of test J-Vs can be retrieved with clustering pattern highlighted by the color code. As illustrated in Fig. 8.4(A), the total number of clusters is found to be K = 3 according to the elbow method, and each test J-V is plotted as a single circular data point in the graph with the colors red, blue, and green reflecting which cluster each data point falls into. Crosses represent the centroids of each cluster. The vast majority of data points fall into the lower left-hand corner, which is classified

further into the red and blue clusters, while the few data points that are identified in the green cluster span the remaining areas. 2-D scatter plots of encoded simulated test J-Vs with color codes indicating different R_S and Φ_B values in Figs. 8.4(B)&(C), respectively.

All simulated J-Vs with R_S values of 5 $\Omega - cm^2$ and 10 $\Omega - cm^2$ fall into the lower left corner, while J-Vs with R_S of 1 $\Omega - cm^2$ are spread across different clusters. Similarly, majority J-Vs with large Φ_B values are categorized in the red cluster indicates some correlation between Φ_B values and clustering patterns. Experimental test J-Vs are projected in Fig. 8.4(D) as black crosses. Among 31 literature-reported J-Vs, 19 belong to red cluster, 11 belong to blue cluster and only 1 belongs to green cluster. To understand the rationale of the clustering patterns, J-Vs of the centroids of red, blue and green clusters are reconstructed through combining the centroids-decoded $\Delta J' - Vs$ with Eq. 8.3. Reconstructed J-Vs of cluster centroids are plotted in Fig. 8.5(A), the color of each curve matches the color code of cluster patterns in Fig. 8.4(A). Three J-Vs have substantial distinctions especially for J in large voltage bias region (V > 0.8 V), with typical rollovers beyond V_{OC} can be observed in the red centroid. Both green and blue curves have no significant roll-over effect beyond V_{OC} indicating that R_S is not the performance limiting factor in both cases. Thirty one experimental J-Vs are also plotted in Fig. 8.5(B), with color indicating the automated classification of each test case. J-Vs in green cluster exhibit greater negative current density at V = 1V and smaller V_{OC} compared to J-Vs of blue cluster.

To set up the correlation between input parameters with physical meanings and clustering patterns generated from statistical approach, the breakdown of test J-Vs are plotted with various R_S and Φ_B respectively. Intuitively, the aforementioned two parameters are the key driving forces for roll-over effects beyond V_{OC}. The influence of R_S on J can be explained using ideal diode equation of solar cells shown in Eq. 8.4:

$$J = J_L - J_o \exp\left(\frac{q(V + JR_S)}{nkT}\right) \tag{8.4}$$

in which J is the operating current density; J_L is light generated current density; J_o is the reverse saturation current density; n is the ideality factor; k is the Boltzmann

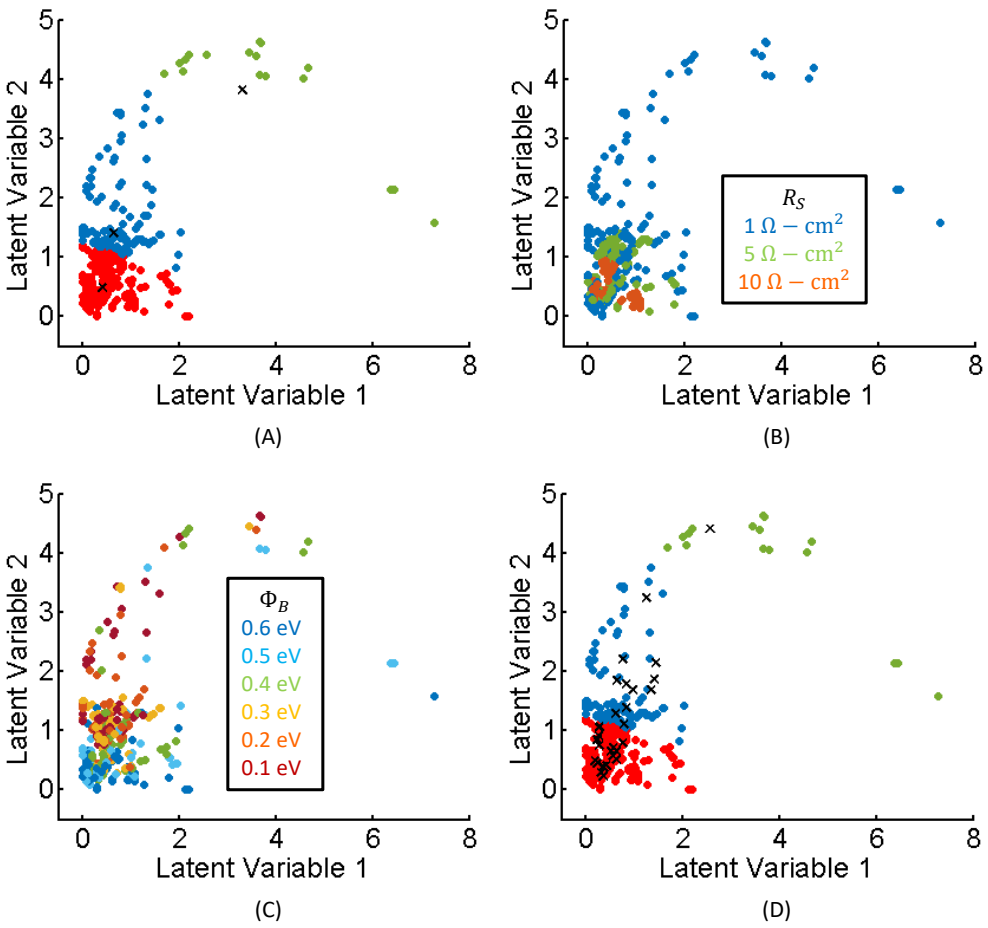

Fig. 8.4.: 2D Scatter Data in latent variable axes defined by the autoencoder: (A) categorized by three clusters generated from K-means algorithm, with each member coded as red, blue and green circles, and cluster centroids highlighted by black crosses; (B). 2D Scatter Data categorized by various series resistance R_S values ($10\ \Omega - cm^2$ in orange circles, $5\ \Omega - cm^2$ in green circles and $1\ \Omega - cm^2$ in blue circles); (C). 2D Scatter Data categorized by various Schottky barrier height Φ_B values from 0.1 eV to 0.6 eV (dark red to dark blue); (D). 2D Scatter plot of three clusters based on purely simulated testing J-Vs and experimental testing J-Vs are highlighted in black cross which are distributed in all three clusters.

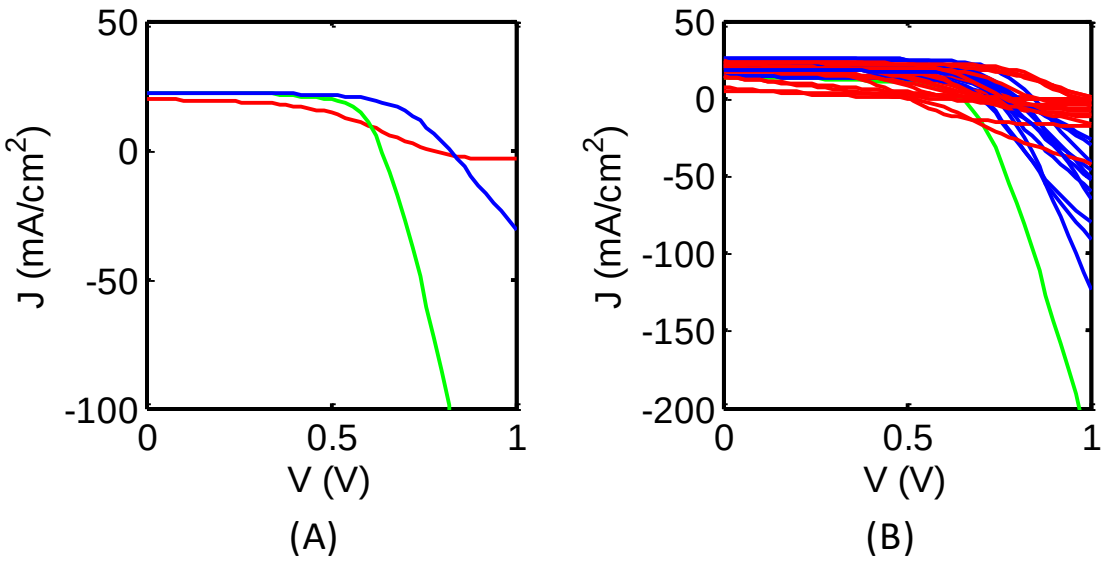

Fig. 8.5.: (A). Reconstructed J-V characteristics from the centroid points of three different clusters showing substantial distinctions. (B). Classification of 31 experimental J-Vs reported in literature for three different clusters.

constant and T is temperature. For $V > V_{OC}$, J flips its sign with respect to the photo-generated current J_L and becomes negative current density. For a fixed bias V and J, increasing R_S would cause the exponential term to be smaller and with self-consistent solving procedure, J would be less negative. On the other hand, Φ_B is a measure of Schottky Barrier height near the back contact, which is often modeled as a diode in series with the solar diode but with opposite orientation in the circuit model [178]. When Φ_B is large, superimposing the J-V curves of two diodes will induce J-V rollover beyond V_{OC}. As shown in Fig. 8.6, despite the fact that majority J-Vs are categorized in red cluster, several observations and conclusions can be drawn from the plots of simulated J-Vs breakdown. 1). For $R_S = 10\ \Omega - cm^2$, all the corresponding J-Vs are labeled as "red cluster", indicating that extraordinarily large R_S outweighs the impact of other parameters and keeps J as a small negative value near the vicinity of $V = 1V$. In contrast, $R_S = 1\ \Omega - cm^2$ is a prerequisite for J to remain largely negative and J-Vs to be classified in the green cluster. However, the classification of

clustering pattern does not solely depend on one parameter. Moderately small R_S $(1,5\ \Omega - cm^2)$ is necessary but not sufficient to exclude J-Vs from the red cluster; 2). The Schottky Barrier height Φ_B is the second most influential parameter to classification of the clustering patterns besides R_S. The probability of simulated J-Vs to be classified as blue clusters generally increase as Φ_B decreases, which is consistent with the awareness that increasing Φ_B will lead to likelihood of J-Vs rollover and smaller negative current density at V = 1V.

To fully understand the rationale of the K-means generated clustering patterns, the performance distribution of test samples within each cluster is assessed. For visualization, two performance metrics (V_{OC}, η) of whole test dataset are plotted in Fig. 8.7 with cluster classification highlighted by identical color code to Fig. 4(A). It is apparent that V_{OC} of red cluster J-Vs span over wide range (0.4 V $\sim$ 1 V), with majority of cell performance not exceeding 10% efficiency (degraded cells). In contrast, blue cluster J-Vs on average exhibit higher V_{OC} (0.8 V) and higher efficiency ($\sim$15%).

While our trained NNA framework with the K-means clustering approach has shown good correlation between selected input physical parameters (i.e. Φ_B and R_S) and clustering patterns, the model is still inadequate and has room for improvement. Standard plot of light J-V starts at V = 0 V and terminates at $V = V_{OC}$. Reported V_{OC} values in the literature rarely exceed 1 V [174], with typical V_{OC} values of CdTe solar cells falling between $0.8 - 0.9$ V. We can retain the J-V characteristics beyond V_{OC} by confining the voltage bias range from 0 V to 1 V with a step size of 0.02 V. The variance is then easily defined as the summation of ΔJ among J-V curves under the same bias. The fixed range and step size of voltage not only simplifies the definition of variance and loss function, but also provides additional information of the light J-V characteristics beyond V_{OC} that has been commonly excluded from the standard light J-V analysis. Nonetheless, fixed range of voltage can also induce uneven contribution to variance at respective bias. According to Fig. 8.5(B), the classification of clusters mainly depends on $J|_{V=1V}$ where J varies

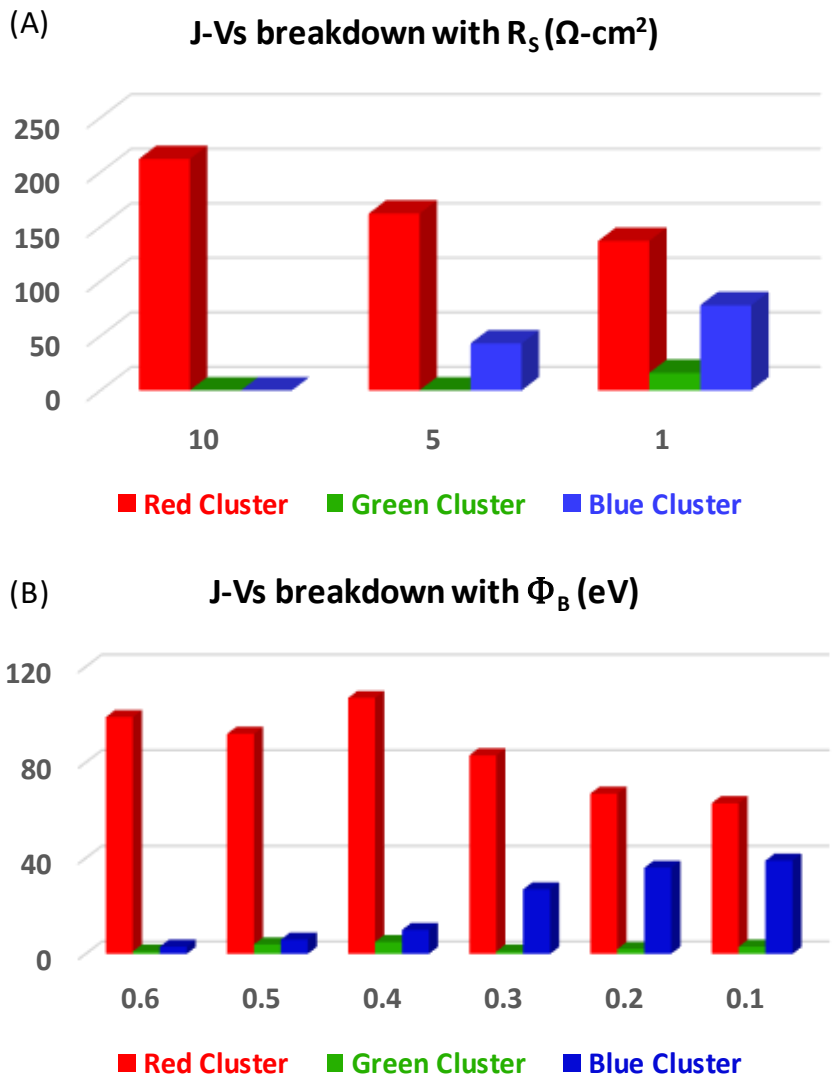

Fig. 8.6.: (A). Count of cluster classified J-Vs with various series resistance R_S; (B). Count of cluster classified J-Vs with various Schottky Barrier height Φ_B.

by substantial amount of current density ($\sim$ 200 mA/cm^2) for respective J-V curves, while $J|_{V=0V} = J_{SC}$ varies by less than 30 mA/cm^2. Thus, the classification outcome is not very susceptible to the current density variation near J_{SC} and cannot be linked to J_{SC} sensitive input parameter such as T_{CdS}, which impacts J_{SC} by varying the thickness for different levels of parasitic absorptions. Another possible shortcoming is that V_{OC} is not closely tied to the classification outcome. Although J-Vs of the

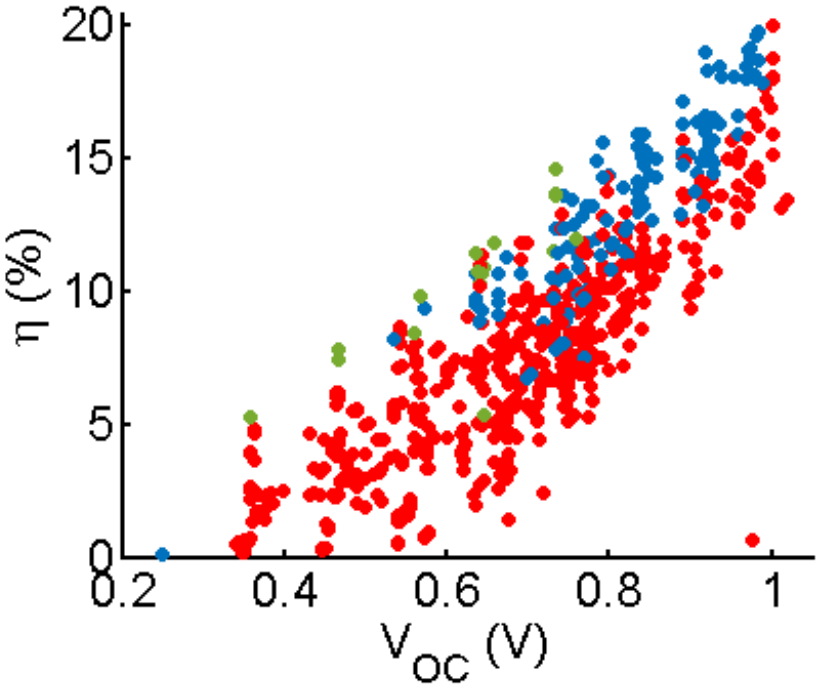

Fig. 8.7.: The open circuit voltage and cell efficiency of test sets (648 simulated + 31 literature reported) are extracted and displayed here as x-y plot. Color code of each datapoint is consistent with color code of clustering in Fig. 8.4(A)

blue cluster generally exhibit greater V_{OC} and η than those of green cluster and red cluster, the classification via unsupervised learning does not guarantee the clear cutoff for clusters in terms of cell performance. The V_{OC} of J-Vs in red cluster spans over a wide range from $\leq$ 0.5 V to 1 V. The reason is that a small negative J near the vicinity of 1V, as a signature of the "red cluster", is not sufficient to determine the exact V_{OC}.

There are several potential model improvements that may enhance the quality of J-V screening and detection. Firstly, as mentioned above, current clustering result is largely driven by the large variation of current density J near 1V. Adding fractional coefficients to reduce the impact of large variation of J near 1V and to emphasize the variation of J near 0V could result in more balanced contribution from

both the small and large bias regions. An alternative way to realize it is to replace the global normalization procedure with local normalization at each individual bias, then the variation of J becomes a fraction of $(J_{max}(V) - J_{min}(V))$ at each bias V. Secondly, although K = 3 is recommended through standard elbow method as the optimum number of clusters for J-Vs screening from the statistical perspective, it may not be directly tied into the underlying physical phenomena. Third, besides the unsupervised learning algorithm with K-means clustering proposed in this paper, supervised learning models such as support-vector machines (SVM) can also be utilized for backward extraction of physical input parameters from input J-V curves. This can be done by labeling each training J-V that contains high-dimensional features with a low dimensional (7 dimensions in this case) vector of which each element within is a measure of respective input parameter values. Trained SVMs with kernel [186] can reconstruct test J-Vs by implicitly mapping the low-dimensional vector into high dimensional feature space, and extracting the input parameter values by reading the elements in the low dimensional vector. Nonetheless, in comparison with the physics-based five parameter (5-D) compact model for light J-V characteristics, the Neural Network Autoencoder appears to be a more powerful tool that only need 2-D latent space for data compression with fairly accurate J-V reconstructions.

8.4 Conclusions

In this chapter, a rapid screening and automated classification of light J-V characteristics of photovoltaic devices has been realized, demonstrated, and validated against experimental data. An unsupervised deep learning Neural Network Autoencoder consists of multi-layer encoder and decoder is designed to encode light J-Vs in 2-D latent space for clustering and decode light J-Vs for reconstruction and validation. TCAD 1-D device modeling of CdS−CdTe solar cell was implemented with a list of sweeping parameters in drift-diffusion solver *Sentaurus* TCAD to generate sufficient amount of light J-V characteristics for training, validation and testing of

the autoencoder. Clustering number K and patterns of the J-V encoded data points in 2-D latent space are computed through elbow method and K-means algorithm respectively. The universality of the NNA framework manifest itself in reconstructing both simulated and experimental J-Vs. Among sweeping parameters in the device model, R_S and Φ_B are found to be the highest contributing parameters to the formation of clustering patterns. Specifically it is found that all that J-V curves belong to green cluster has $R_S = 1\ \Omega - cm^2$ and J-V curves with $R_S = 10\ \Omega - cm^2$ are classified in red cluster. This framework paves the way for combining statistical machine learning models with physics-based device models to realize automated detection and rapid screening of J-V characteristics of photovoltaic devices, which is considered as a promising technique to help establish a new standard operating procedure (SOP) for quality control in the large-scale production of PV panels.

9. SUMMARY & FUTURE WORK

9.1 Thesis Summary

In this thesis, we developed a comprehensive multi-physics based framework to solve various PV-related problems. Specifically, we established an opto-electro coupled framework that self-consistently solves the optical generation and carrier transport within the solar cell structure through Technology Computer Aided Design (TCAD) softare *Sentaurus* as the baseline modeling platform to provide physical insights and detailed analysis in both Silicon and thin-film solar cells. The major accomplishments of the thesis include:

1. exploration of novel rear-heterojunction design of wide-E_g GaInP solar cell as a transitional stage towards improvement of high efficiency multijunction solar cells;

2. discovery of temperature and illumination effect on Silicon heterojunction solar cell and coupling optical, thermal and electrical energy transfer for assessing the radiative cooling effect on concentrating photovoltaic devices;

3. derivation of analytical formula that is well calibrated to rigorous optic-electric coupled device simulation for optimal design of back contact pattern in bifacial solar cells;

4. construction of neural network autoencoder that compress and restore J-V characteristics of thin film solar cells to quantitatively classify manufactured cells and realize rapid screening.

9.1.1 Summary of chapter 2: Modeling wide-E_g GaInP solar cell

Development of wide-E_g (> 2.0 eV) solar cell is essential to form multijunction (junction number ≥ 4) photovoltaic devices that achieve ultra high efficiency ($> 40\%$). State-of-the-art Molecular Beam Epitaxial (MBE) grown wide-E_g GaInP only delivers efficiency of 3.1%, which is substantially lower than theoretical maximum efficiency. To tackle this problem, we have made the following contributions:

1. Establish the device modeling framework that successfully reproduce the experimental I-V characteristics;

2. Identify the major cause of the performance degradation in wide-E_g solar cell: the poor quality AlInP/GaInP interface and relatively low minority carrier lifetime in absorber;

3. Propose n-i-p structure to enhance the carrier collection efficiency with the presence of electric field, optimize the structure by tweaking the doping concentration and thickness of absorber.

9.1.2 Summary of chapter 3: Exploring Novel Rear Heterojunction Design for GaInP solar cell

$Ga_{0.5}In_{0.5}P$ (GaInP) with bandgap of 1.89 eV is lattice-matched to GaAs and is ideally the leading candidate for top cell for the monolithic mutltijunction photovoltaics. Recent advance of efficiency enhancement for GaInP solar cell relies on shifting the conventional front homojunction (FHJ) design to rear heterojunction (RHJ) design. Despite the efficency boost, there is a lack of physics-based explanation of how the RHJ prevails over FHJ. To clarify it, we have made the following contributions:

1. Derive the analytical model of dark recombination current for both design and quantify the suppression of recombination current within space charge region for RHJ;

2. Perform the numerical device model with variation of rear surface recombination velocity and minority carrier lifetime to identify the critical parameter values for both design;

3. Propose diffusive back reflector as future direction of improvement to enhance the optical absorption (thus J_{SC}) near the rear side of RHJ GaInP solar cell.

9.1.3 Summary of chapter 4: Discovery of V_{OC} degradation in Thin-Film Vapor Liquid Solid grown InP solar cell

Indium Phosiphide (InP) has a bandgap of 1.4 eV similar to GaAs, is close to the optimum E_g for PV applications according to spectral Shockley-Queisser Limit chart. The major obstacle that prevents it from commercialization is the expensive vacuum based MBE growth technique involved. Vapor Liquid Solid (VLS) growth technique is proposed to lower the process cost but suffers from V_{OC} degradation. To explain the origin of this phenomenon, we made the following contribution:

1. Based on the exponential relation between applied bias and illumination intensity, quantitatively correlate the photoluminescence (PL) image with spatial distribution map of V_{OC};

2. Examine two hypotheses local shunting and bandgap narrowing for degradation by establishing spice circuit model for InP gridline network and reproduce the degraded I-V characteristics observed in VLS grown samples.

9.1.4 Summary of chapter 5: Radiative Cooling Effect in Concentrating Photovoltaics Systems

With the presence of 8-13 μm atmospheric transmission window, radiative cooling has emerged as a promising passive cooling technique for solar device operation with high heat load. We made the following contributions to quantify the effect:

1. Set up rigorous device modeling framework to quantify the efficiency of Silicon heterojuncion solar cell under various illumination intensity and temperature;

2. Propose the porous soda-lime glass with near ideal spectral emissivity profile as radiative cooler for concentrating photovoltaic devices;

3. Create opto-thermal-electric coupled framework that self-consistently solve the energy balance equation and equilibrium temperature for the operational device employing different passive cooling techniques;

4. Demonstrate the advantage of radiative cooler over passive finned copper cooler through newly-introduced figure of merit "cooling power per weight".

9.1.5 Summary of chapter 6: Tailor Back Contact Design of *bifacial* IBC Silicon Heterojunction Solar Cell

Bifacial solar cells that allow the absorption of sunlight from both front and rear side have become increasingly important with projected 60% of total PV market share by 2029. Combining bifaciality with commercialized Silicon heoterjunction solar cell can boost power output for fixed footprint. There was yet study to find out optimum back contact pattern that minimize the sum of optical shadow loss and electrical resistive loss. To combat this challenge, we made the following contribution:

1. The benchmark of experimental I-V characteristics and spectral external quantum efficiency profile of record *monofacial* IBC-SHJ solar cell with developed opto-electric device model for validation;

2. Introduce rear side illumination into the simulation setup and modify the back contact length scale to explore the optimum contact/gap ratio that maximize the total power output of bifacial IBC-SHJ solar cells;

3. Develop generalized analytical formula for power output as a function of gap ratio and albedo factor, which is well-calibrated to simulation results.

9.1.6 Summary of chapter 7: Tailor Back Contact Design of *bifacial* CIGS Solar Cell

The importance of switching from *monofacial* to *bifacial* photovoltaics is addressed in Chapter 6. It is worthwhile generalizing the *bifacial* analytical model of Copper Indium Gallium DiSelenide (CIGS), which is considered as the leading thin film PV technology with highest state-of-the-art efficiency. Direct application of previously develoepd analytical model for CIGS is not feasible since carrier transport within CIGS absorber depends heavily on the position of electric field. To come up with the alternative analytical model for thin-film technology, we made the following contribution:

1. Decouple the front and rear illumination in CIGS solar cell, and introduce fractional optical and electrical losses for device performance after switching from front to rear illumination;

2. Modify the generalized analytical model for IBC-SHJ solar cell to account for additional losses in CIGS with electric field away from the absorbing surface under rear illuminations;

3. Use the modified analytical model to predict the fractional power output enhancement under global average albedo factor of 0.3.

9.1.7 Summary of chapter 8: Rapid Screening and Automated Detection of PV cell Performance via an unsupervised Autoencoder Neural Network

With global installed PV capacity expanding rapidly over past decades, rapid screening and automated detection of manufactured PV cell performance is essential for speedy and precise quality control. To meet this demand, we utilized autoencoder machine learning package for data processing and classification. We made the following contribution:

1. Invent new approach to treat light J-V characteristics with multiple biases analogous to training, testing and validation examples with multiple features;

2. Construct autoencoder neural network to compress J-Vs in 2-D latent space and validate the framework through reconstruction of J-Vs by decoding the compressed data from latent space;

3. Employ elbow method and K-means algorithm to classify the encoded data in 2-D latent space to achieve automated classification of input J-Vs;

4. Corrlate clustering patterns with input strucutural and electrical parameters to find out series resistance R_S and schottky barrier height Φ_B are the leading factors in determining clustering result.

9.2 Future Work

9.2.1 Tunnel IBC-SHJ solar cell

As silicon-based PV cell efficiencies approach the S-Q limit using interdigitated back contacted architecture, the complex fabrication procedure involving intermediate photolithographic patterning steps makes it currently unsuitable for low-cost commercialization. There has been great efforts in seeking for low-complexity fabrication process for IBC Silicon-based solar cells. Tunnel-IBC was developed to allow full-area deposition of p-type $a-Si:H$ film at that rear side as a blanket layer without patterning. In this way, p-type $a-Si:H$ thin film directly contacts to intrinsic $a-Si:H$ film and forms the hole collector in the area devoid of n-type $a-Si:H$; while the electron collector is composed of intrinsic $a-Si:H$, n-type $a-Si:H$ and p-type $a-Si:H$ a triple layer stack that characterizes an interband tunnel junction for carrier transport. Despite the simplicity of the fabrication process, tunnel-IBC Silicon solar cell exhibits $> 22.5\%$ efficiency which is approx. 4% below that of a conventional IBC Silicon cell. It is invaluable to investigate the source of this discrepancy and propose advancement plans for this growth process to help IBC technology

maintain high efficiency, become more cost effective and take over the market share of PV industry.

9.2.2 *Bifacial* Tandem Perovskite/IBC-SHJ solar cell

Reduction of levelized cost of energy(LCOE) is the key goal that PV community needs to focus on to keep up with other clean energy sources. One way to realize it is to maximize the power ouput for fixed footprint. Besides the rapid expansion of bifacial single junction technology, tandem solar cells were proposed long ago as an alternative pathway to realization by reducing the thermalization loss arisen from high-E_g photon absorption. Recent advances in perovskite solar cells led it to be considered a highly-promising top cell candidate with tunable bandgap and cost effective roll-to-roll process. Recent work indicates that bifacial Perovskite/Silicon tandem solar cells can theoretically achieve a normalized output efficiency of 33% at practical albedos with insensitive design constraints to Perovskite layer thickness. Nonetheless, state-of-the-art record monolithic Perovksite/Silicon tandem solar cells exhibits 29.1% power conversion efficiency, which is well below the theoretically projected efficiency. In this regards, potential future work may involve 1). exploration of the origin of efficiency gap; 2). investigation of different tandem or triple junction designs (monolithic versus separate, involving a range of contacting schemes); and 3). improvement of reliability of perovskite top cells and overall mean time to failure.

REFERENCES

REFERENCES

[1] L. Capuano, "International energy outlook 2018 (ieo2018)," *US Energy Information Administration (EIA): Washington, DC, USA*, vol. 2018, p. 21, 2018.

[2] IRENA International Renewable Energy Agency, "Renewable capacity highlights," no. March, p. 2, 2018. [Online]. Available: http://www.irena.org/DocumentDownloads/Publications/RE{_}stats{_}highlights{_}2017.pdf

[3] I. IRENA, "Renewable power generation costs in 2017," *Report, International Renewable Energy Agency, Abu Dhabi*, 2018.

[4] K. Hwang, Y.-S. Jung, Y.-J. Heo, F. H. Scholes, S. E. Watkins, J. Subbiah, D. J. Jones, D.-Y. Kim, and D. Vak, "Toward large scale roll-to-roll production of fully printed perovskite solar cells," *Advanced materials*, vol. 27, no. 7, pp. 1241–1247, 2015.

[5] R. Asadpour, R. V. Chavali, M. Ryyan Khan, and M. A. Alam, "Bifacial si heterojunction-perovskite organic-inorganic tandem to produce highly efficient (η t* 33%) solar cell," *Applied Physics Letters*, vol. 106, no. 24, p. 243902, 2015.

[6] A. Magomedov, E. Kasparavičius, K. Rakstys, S. Paek, N. Gasilova, K. Genevičius, G. Juška, T. Malinauskas, M. K. Nazeeruddin, and V. Getautis, "Pyridination of hole transporting material in perovskite solar cells questions the long-term stability," *Journal of Materials Chemistry C*, vol. 6, no. 33, pp. 8874–8878, 2018.

[7] W. Shockley and H. J. Queisser, "Detailed balance limit of efficiency of p-n junction solar cells," *Journal of applied physics*, vol. 32, no. 3, pp. 510–519, 1961.

[8] V. Ganapati, C.-S. Ho, and E. Yablonovitch, "Air gaps as intermediate selective reflectors to reach theoretical efficiency limits of multibandgap solar cells," *IEEE Journal of Photovoltaics*, vol. 5, no. 1, pp. 410–417, 2014.

[9] E. D. Kosten, J. Lloyd, E. Warmann, and H. A. Atwater, "Spectrum splitting photovoltaics: light trapping filtered concentrator for ultrahigh photovoltaic efficiency," in *2013 IEEE 39th Photovoltaic Specialists Conference (PVSC)*. IEEE, 2013, pp. 3053–3057.

[10] J. J. Wysocki and P. Rappaport, "Effect of temperature on photovoltaic solar energy conversion," *Journal of applied physics*, vol. 31, no. 3, pp. 571–578, 1960.

[11] K. H. Montgomery, C. Heredia, and J. M. Woodall, "Design and modeling of a high efficiency hybrid photovoltaic-photothermal concentrator (pvptc) system," in *2013 IEEE 39th Photovoltaic Specialists Conference (PVSC)*. IEEE, 2013, pp. 1755–1760.

[12] P. P. Jenkins, S. Messenger, K. M. Trautz, S. I. Maximenko, D. Goldstein, D. Scheiman, R. Hoheisel, and R. J. Walters, "High-bandgap solar cells for underwater photovoltaic applications," *IEEE Journal of Photovoltaics*, vol. 4, no. 1, pp. 202–207, 2013.

[13] M. Yamaguchi, T. Takamoto, K. Araki, and N. Ekins-Daukes, "Multi-junction iii–v solar cells: current status and future potential," *Solar Energy*, vol. 79, no. 1, pp. 78–85, 2005.

[14] R. King, D. Bhusari, A. Boca, D. Larrabee, X.-Q. Liu, W. Hong, C. Fetzer, D. Law, and N. Karam, "Band gap-voltage offset and energy production in next-generation multijunction solar cells," *Progress in Photovoltaics: Research and Applications*, vol. 19, no. 7, pp. 797–812, 2011.

[15] C. Allen, J. Woodall, and J.-H. Jeon, "Results of a gallium phosphide photovoltaic junction with an ar coating under concentration of natural sunlight," *Solar energy materials and solar cells*, vol. 95, no. 9, pp. 2655–2658, 2011.

[16] M. Vaisman, S. Tomasulo, T. Masuda, J. Lang, J. Faucher, and M. L. Lee, "Effects of growth temperature and device structure on gap solar cells grown by molecular beam epitaxy," *Applied Physics Letters*, vol. 106, no. 6, p. 063903, 2015.

[17] X. Lu, R. Hao, M. Diaz, R. L. Opila, and A. Barnett, "Improving gap solar cell performance by passivating the surface using alxga1-xp epi-layer," *IEEE Journal of the Electron Devices Society*, vol. 1, no. 5, pp. 111–116, 2013.

[18] E. F. Schubert, T. Gessmann, and J. K. Kim, "Light emitting diodes," *Kirk-Othmer Encyclopedia of Chemical Technology*, 2000.

[19] S. Tomasulo, J. Faucher, J. R. Lang, K. N. Yaung, and M. L. Lee, "2.19 ev ingap solar cells on gap substrates," in *2013 IEEE 39th Photovoltaic Specialists Conference (PVSC)*. IEEE, 2013, pp. 3324–3328.

[20] J. Gray, X. Wang, R. V. K. Chavali, X. Sun, A. Kanti, and J. R. Wilcox, "Adept 2.1," Mar 2011. [Online]. Available: https://nanohub.org/resources/adeptnpt

[21] K. Park, C. Park, S. Ravindran, S. Kang, H. Hwang, Y. Jho, Y. Jo, B. Kim, and Y. Lee, "Enhancement of minority carrier lifetime of gainp with lateral composition modulation structure grown by molecular beam epitaxy," *Journal of Applied Physics*, vol. 116, no. 4, p. 043516, 2014.

[22] P. Bermel, M. Ghebrebrhan, W. Chan, Y. X. Yeng, M. Araghchini, R. Hamam, C. H. Marton, K. F. Jensen, M. Soljačić, J. D. Joannopoulos *et al.*, "Design and global optimization of high-efficiency thermophotovoltaic systems," *Optics express*, vol. 18, no. 103, pp. A314–A334, 2010.

[23] A. Blakers and M. Green, "20% efficiency silicon solar cells," *Applied physics letters*, vol. 48, no. 3, pp. 215–217, 1986.

[24] M. Wanlass, G. Horner, T. Gessert, T. Coutts, and I. Weinberg, "Epitaxial inp and related iii-v compounds applied to solar cells," in *1st Intl Conf on Indium Phosphide and Related Materials for Advanced Electronic and Optical Devices*, vol. 1144. International Society for Optics and Photonics, 1989, pp. 445–458.

[25] W. Cheah, W. Fan, S. Yoon, D. Zhang, B. Ng, W. Loke, R. Liu, and A. Wee, "Gaas-based heterojunction pin photodetectors using pentanary ingaasnsb as the intrinsic layer," *IEEE photonics technology letters*, vol. 17, no. 9, pp. 1932–1934, 2005.

[26] A. Shalav, B. Richards, and M. Green, "Luminescent layers for enhanced silicon solar cell performance: Up-conversion," *Solar energy materials and solar cells*, vol. 91, no. 9, pp. 829–842, 2007.

[27] M. A. Green and K. Emery, "Solar cell efficiency tables," *Progress in Photovoltaics: Research and Applications*, vol. 1, no. 1, pp. 25–29, jan 1993.

[28] A. Bett, F. Dimroth, G. Stollwerck, and O. Sulima, "III-V compounds for solar cell applications," *Applied Physics A: Materials Science & Processing*, vol. 69, no. 2, pp. 119–129, 1999.

[29] H. Cotal, C. Fetzer, J. Boisvert, G. Kinsey, R. King, P. Hebert, H. Yoon, and N. Karam, "III–V multijunction solar cells for concentrating photovoltaics," *Energy Environ. Sci.*, vol. 2, no. 2, pp. 174–192, 2009. [Online]. Available: http://xlink.rsc.org/?DOI=B809257E

[30] R. M. France, J. F. Geisz, W. E. Mcmahon, M. A. Steiner, S. Johnston, and D. J. Friedman, "Metamorphic III – V Solar Cells:Recent Progress and Potential," *IEEE Journal of Photovoltaics*, vol. 6, no. 1, pp. 366–373, 2016.

[31] K. Tanabe, "A review of ultrahigh efficiency III-V semiconductor compound solar cells: Multijunction tandem, lower dimensional, photonic up/down conversion and plasmonic nanometallic structures," *Energies*, vol. 2, no. 3, pp. 504–530, 2009.

[32] M. Yamaguchi, T. Takamoto, K. Araki, and N. Ekins-Daukes, "Multi-junction III-V solar cells: Current status and future potential," *Solar Energy*, vol. 79, no. 1, pp. 78–85, 2005.

[33] M. A. Green, Y. Hishikawa, E. D. Dunlop, D. H. Levi, J. Hohl-Ebinger, and A. W. Ho-Baillie, "Solar cell efficiency tables (version 51)," *Progress in Photovoltaics: Research and Applications*, vol. 26, no. 1, pp. 3–12, 2018.

[34] T. Takamoto, E. Ikeda, H. Kurita, and M. O, "Structural optimization for single junction InGaP solar cells," *Solar Energy Materials and Solar Cells*, vol. 35, pp. 25–31, 1994.

[35] J. F. Geisz, M. a. Steiner, I. García, S. R. Kurtz, and D. J. Friedman, "Enhanced external radiative efficiency for 20.8% efficient single-junction GaInP solar cells," *Applied Physics Letters*, vol. 103, no. 4, pp. 2011–2016, 2013.

[36] S. Kim, S.-T. Hwang, W. Yoon, and H.-M. Lee, "High Performance GaAs Solar Cell Using Heterojunction Emitter And Its Further Improvement By ELO Technique," in *32nd European Photovoltaic Solar Energy Conference and Exhibition*, 2016, pp. 1424–1427.

[37] C. T. Sah, R. N. Noyce, and W. Shockley, "Carrier Generation and Recombination in P-N Junctions and P-N Junction Characteristics," *Proceedings of the IRE*, vol. 45, no. 9, pp. 1228–1243, 1957.

[38] Synopsys Inc, "Sentaurus Device," p. Ver. L, 2016. [Online]. Available: https://www.synopsys.com/silicon/tcad/device-simulation/sentaurus-device.html

[39] E. E. Perl, D. Kuciauskas, J. Simon, D. J. Friedman, and M. A. Steiner, "Identification of the limiting factors for high-temperature GaAs, GaInP, and AlGaInP solar cells from device and carrier lifetime analysis," *Journal of Applied Physics*, vol. 122, no. 23, 2017.

[40] R. V. K. Chavali, S. Khatavkar, C. Kannan, V. Kumar, P. R. Nair, J. L. Gray, and M. A. Alam, "Multiprobe characterization of inversion charge for self-consistent parameterization of hit cells," *IEEE Journal of Photovoltaics*, vol. 5, no. 3, pp. 725–735, 2015.

[41] J. E. Moore, S. Dongaonkar, R. V. K. Chavali, M. A. Alam, and M. S. Lundstrom, "Correlation of Built-In Potential and I – V Crossover in Thin-Film Solar Cells," *IEEE Journal of Photovoltaics*, vol. 4, no. 4, pp. 1138–1148, 2014.

[42] M. Gloeckler, A. Fahrenbruch, and J. Sites, "Numerical modeling of CIGS and CdTe solar cells: setting the baseline," *3rd World Conference onPhotovoltaic Energy Conversion, 2003. Proceedings of*, vol. 1, pp. 491–494, 2003.

[43] S. Hegedus, D. Desai, and C. Thompson, "Voltage Dependent Photocurrent Collection in CdTe/CdS Solar Cells," *Progress in Photovoltaics: Research and Applications*, vol. 15, no. 7, pp. 587–602, 2007.

[44] M. Burgelman, P. Nollet, S. Degrave, and J. Beier, "Modeling the cross-over of the I-V characteristics of thin film CDTE solar cells," *Conference Record of the IEEE Photovoltaic Specialists Conference*, vol. 2000-Janua, pp. 551–554, 2000.

[45] X. Wang, M. R. Khan, J. L. Gray, A. Alam, and M. S. Lundstrom, "Design of GaAs Solar Cells Operating Close to the Shockley-Quiesser Limit," *Journal of Photovoltaics*, vol. 3, no. 2, pp. 737–744, 2013.

[46] U. Rau, "Reciprocity relation between photovoltaic quantum efficiency and electroluminescent emission of solar cells," *Physical Review B*, vol. 76, no. 8, p. 085303, 2007.

[47] X. Wang and M. Lundstrom, "On the Use of Rau's Reciprocity to Deduce External Radiative Efficiency in Solar Cells," *Journal of photovoltaics*, vol. 3, no. 4, pp. 1348–1353, 2013.

[48] M. A. Green, "Radiative efficiency of state-of-the-art photovoltaic cells," *Progress in Photovoltaics: Research and Applications*, vol. 20, no. 4, pp. 472–476, 2012.

[49] W. Van Roosbroeck and W. Shockley, "Photon-Radiative Recombination of Electrons and Holes in Germanium," *Physical Review*, vol. 94, no. 6, pp. 1558–1560, 1954.

[50] P. Asbeck, "Self-absorption effects on the radiative lifetime in GaAs-GaAlAs double heterostructures," *Journal of Applied Physics*, vol. 48, no. 2, pp. 820–822, 1977.

[51] J. Nelson, *The Physics of Solar Cells*. Imperial College Press.

[52] H. J. Hovel, *Solar Cells*. Academic Press, 1975.

[53] A. Fahrenbruch and R. Bube, *Fundamentals of solar cells: photovoltaic solar energy conversion*. Elsevier, 2012.

[54] M. Boulou and D. Bois, "Cathodoluminescence measurements of the minority-carrier lifetime in semiconductors," *Journal of Applied Physics*, vol. 48, no. 11, pp. 4713–4721, 1977.

[55] R. King, J. Ermer, and D. Joslin, "Double heterostructures for characterization of bulk lifetime and interface recombination velocity in III-V multijunction solar cells," *2nd World Conference on Photovoltaic Solar Energy Conversion, Vienna, Austria, 6-10 July*, pp. 86–90, 1998. [Online]. Available: http://www.spectrolab.com/pv/support/R.Kingetal.,WCPEC1998, DoubleheterostructuresinIII-VMJcells.pdf

[56] A. S. Gudovskikh, N. A. Kaluzhniy, V. M. Lantratov, S. A. Mintairov, M. Z. Shvarts, and V. M. Andreev, "Numerical modelling of GaInP solar cells with AlInP and AlGaAs windows," *Thin Solid Films*, vol. 516, no. 20, pp. 6739–6743, 2008.

[57] J. G. Fossum and D. S. Lee, "A physical model for the dependence of carrier lifetime on doping density in nondegenerate silicon," *Solid State Electronics*, vol. 25, no. 8, pp. 741–747, 1982.

[58] J. Fossum, R. Mertens, D. Lee, and J. Nijs, "Carrier recombination and lifetime in highly doped silicon," *Solid-State Electronics*, vol. 26, no. 6, pp. 569–576, 1983. [Online]. Available: http://www.sciencedirect.com/science/article/pii/0038110183901739

[59] N. D. Arora, J. R. Hauser, and D. J. Roulston, "Electron and Hole Mobilities in Silicon as a Function of Concentration and Temperature," *IEEE Transactions on Electron Devices*, vol. 29, no. 2, pp. 292–295, 1982.

[60] G. Masetti and S. Solmi, "Modeling of Carrier Mobility Against Carrier Concentration in Arsenic-, Phosphorus-, and Boron-Doped Silicon," *IEEE Transactions on Electron Devices*, vol. 30, no. No. 7, pp. 764–769, 1983.

[61] S. C. Jain and D. J. Roulston, "A simple expression for band gap narrowing ({BNG}) in heavily doped {Si, Ge, GaAs and Ge_{x}Si_{1-x}} strained layers," *Solid–State Electronics*, vol. 34, no. 5, pp. 453–465, 1991.

[62] A. S. Gudovskikh, J. P. Kleider, N. A. Kalyuzhnyy, V. M. Lantratov, and S. A. Mintairov, "Solar Energy Materials & Solar Cells Band structure at heterojunction interfaces of GaInP solar cells," *Solar Energy Materials and Solar Cells*, vol. 94, no. 11, pp. 1953–1958, 2010. [Online]. Available: http://dx.doi.org/10.1016/j.solmat.2010.06.027

[63] J. F. Geisz, M. A. Steiner, R. M. France, D. J. Friedman, and S. R. Kurtz, "Implications of Redesigned, High-Radiative-Efficiency GaInP Junctions on III-V Multijunction Concentrator Solar Cells," *Journal of Photovoltaics*, vol. 5, no. 1, pp. 418–424, 2015.

[64] T. Tiedje, E. Yablonovitch, G. Cody, and B. Brooks, "Limiting efficiency of silicon solar cells," *IEEE Transactions on Electron Devices*, vol. 31, no. 5, pp. 711–716, 1984. [Online]. Available: http://ieeexplore.ieee.org/xpls/abs{_}all.jsp?arnumber=1483879{%}5Cnhttp://ieeexplore.ieee.org/lpdocs/epic03/wrapper.htm?arnumber=1483879{%}5Cnhttp://ieeexplore.ieee.org/lpdocs/epic03/wrapper.htm?arnumber=1483879

[65] C. Barugkin, F. J. Beck, and K. R. Catchpole, "Diffuse reflectors for improving light management in solar cells : a review and outlook," *Journal of Optics*, vol. 19, no. 1, 2017.

[66] H. Chung, K.-Y. Jung, and P. Bermel, "Flexible flux plane simulations of parasitic absorption in nanoplasmonic thin-film silicon solar cells," *Optical Materials Express*, vol. 5, no. 9, p. 2054, aug 2015.

[67] P. Campbell and M. A. Green, "Light trapping properties of pyramidally textured surfaces," *Journal of Applied Physics*, vol. 62, no. 1, pp. 243–249, 1987.

[68] R. Brendel, M. Hirsch, R. Plieninger, and J. H. Werner, "Ouantum Efficiencv Analvsis of Thin-Layer Silicon Solar Cells," *IEEE Transactions on Electron Devices*, vol. 43, no. 7, pp. 1104–1113, 1996. [Online]. Available: http://ieeexplore.ieee.org/lpdocs/epic03/wrapper.htm?arnumber=502422

[69] P. Bermel, C. Luo, L. Zeng, L. C. Kimerling, and J. D. Joannopoulos, "Improving thin-film crystalline silicon solar cell efficiencies with photonic crystals," *Optics Express*, vol. 15, no. 25, pp. 16 986–17 000, 2007. [Online]. Available: http://www.opticsinfobase.org/abstract.cfm?URI=oe-15-25-16986

[70] P. Sheng, "Optical Absorption of Thin Film on a Lambertian Reflector Substrate," *IEEE Transactions on Electron Devices*, vol. 31, no. 5, pp. 634–636, 1984.

[71] E. Yablonovitch and G. D. Cody, "Intensity Enhancement in Textured Optical Sheets for Solar Cells," *IEEE Transactions on Electron Devices*, vol. 29, no. 2, pp. 300–305, 1986.

[72] K. Emery, Y. Hishikawa, W. Warta, E. Dunlop, D. Levi, and A. Ho-Baillie, "Solar cell efficiency tables (version 46)," in *Mat. Res. Soc*, vol. 2, no. 3, 2015, pp. 231–234.

[73] L. Chen, W. Lu, and C. M. Lieber, "Semiconductor nanowire growth and integration," 2014.

[74] R. Kapadia, Z. Yu, M. Hettick, J. Xu, M. S. Zheng, C.-Y. Chen, A. D. Balan, D. C. Chrzan, and A. Javey, "Deterministic nucleation of inp on metal foils with the thin-film vapor–liquid–solid growth mode," *Chemistry of Materials*, vol. 26, no. 3, pp. 1340–1344, 2014.

[75] R. Kapadia, Z. Yu, H.-H. H. Wang, M. Zheng, C. Battaglia, M. Hettick, D. Kiriya, K. Takei, P. Lobaccaro, J. W. Beeman *et al.*, "A direct thin-film path towards low-cost large-area iii-v photovoltaics," *Scientific reports*, vol. 3, p. 2275, 2013.

[76] M. Zheng, H.-P. Wang, C. M. Sutter-Fella, C. Battaglia, S. Aloni, X. Wang, J. Moore, J. W. Beeman, M. Hettick, M. Amani *et al.*, "Thin-film solar cells with inp absorber layers directly grown on nonepitaxial metal substrates," *Advanced Energy Materials*, vol. 5, no. 22, p. 1501337, 2015.

[77] M. Zheng, K. Horowitz, M. Woodhouse, C. Battaglia, R. Kapadia, and A. Javey, "Iii-vs at scale: a pv manufacturing cost analysis of the thin film vapor–liquid–solid growth mode," *Progress in Photovoltaics: Research and Applications*, vol. 24, no. 6, pp. 871–878, 2016.

[78] L. C. Hirst and N. J. Ekins-Daukes, "Fundamental losses in solar cells," *Progress in Photovoltaics: Research and Applications*, vol. 19, no. 3, pp. 286–293, 2011.

[79] C. Keavney, V. Haven, and S. Vernon, "Emitter structures in mocvd inp solar cells," in *IEEE Conference on Photovoltaic Specialists*. IEEE, 1990, pp. 141–144.

[80] S. Johnston, A. A. Motz, J. Moore, M. Zheng, A. Javey, and P. Bermel, "Photoluminescence imaging characterization of thin-film inp," in *2015 IEEE 42nd Photovoltaic Specialist Conference (PVSC)*. IEEE, 2015, pp. 1–6.

[81] X. Yin, C. Battaglia, Y. Lin, K. Chen, M. Hettick, M. Zheng, C.-Y. Chen, D. Kiriya, and A. Javey, "19.2% efficient inp heterojunction solar cell with electron-selective tio2 contact," *ACS photonics*, vol. 1, no. 12, pp. 1245–1250, 2014.

[82] Y. P. Varshni, "Temperature dependence of the energy gap in semiconductors," *physica*, vol. 34, no. 1, pp. 149–154, 1967.

[83] M. Kasemann, D. Grote, B. Walter, W. Kwapil, T. Trupke, Y. Augarten, R. Bardos, E. Pink, M. Abbott, and W. Warta, "Luminescence imaging for the detection of shunts on silicon solar cells," *Progress in Photovoltaics: Research and Applications*, vol. 16, no. 4, pp. 297–305, 2008.

[84] F. Trombe *et al.*, "Perspectives sur l'utilisation des rayonnements solaires et terrestres dans certaines regions du monde," 1975.

[85] B. Bartoli, S. Catalanotti, B. Coluzzi, V. Cuomo, V. Silvestrini, and G. Troise, "Nocturnal and diurnal performances of selective radiators," *Applied Energy*, vol. 3, no. 4, pp. 267–286, 1977.

[86] C. Granqvist and A. Hjortsberg, "Radiative cooling to low temperatures: General considerations and application to selectively emitting sio films," *Journal of Applied Physics*, vol. 52, no. 6, pp. 4205–4220, 1981.

[87] S. Catalanotti, V. Cuomo, G. Piro, D. Ruggi, V. Silvestrini, and G. Troise, "The radiative cooling of selective surfaces," *Solar Energy*, vol. 17, no. 2, pp. 83–89, 1975.

[88] C. Granqvist, A. Hjortsberg, and T. Eriksson, "Radiative cooling to low temperatures with selectivity ir-emitting surfaces," *Thin Solid Films*, vol. 90, no. 2, pp. 187–190, 1982.

[89] A. R. Gentle and G. B. Smith, "Radiative heat pumping from the earth using surface phonon resonant nanoparticles," *Nano letters*, vol. 10, no. 2, pp. 373–379, 2010.

[90] Y. X. Yeng, M. Ghebrebrhan, P. Bermel, W. R. Chan, J. D. Joannopoulos, M. Soljačić, and I. Celanovic, "Enabling high-temperature nanophotonics for energy applications," *Proceedings of the National Academy of Sciences*, vol. 109, no. 7, pp. 2280–2285, 2012.

[91] M. Ghebrebrhan, P. Bermel, Y. Yeng, I. Celanovic, M. Soljačić, and J. Joannopoulos, "Tailoring thermal emission via q matching of photonic crystal resonances," *Physical Review A*, vol. 83, no. 3, p. 033810, 2011.

[92] A. P. Raman, M. A. Anoma, L. Zhu, E. Rephaeli, and S. Fan, "Passive radiative cooling below ambient air temperature under direct sunlight," *Nature*, vol. 515, no. 7528, pp. 540–544, 2014.

[93] Z. Chen, L. Zhu, A. Raman, and S. Fan, "Radiative cooling to deep sub-freezing temperatures through a 24-h day–night cycle," *Nature communications*, vol. 7, no. 1, pp. 1–5, 2016.

[94] Y. Zhai, Y. Ma, S. N. David, D. Zhao, R. Lou, G. Tan, R. Yang, and X. Yin, "Scalable-manufactured randomized glass-polymer hybrid metamaterial for daytime radiative cooling," *Science*, vol. 355, no. 6329, pp. 1062–1066, 2017.

[95] L. Zhu, A. P. Raman, and S. Fan, "Radiative cooling of solar absorbers using a visibly transparent photonic crystal thermal blackbody," *Proceedings of the national academy of sciences*, vol. 112, no. 40, pp. 12 282–12 287, 2015.

[96] Z. Zhou, X. Sun, and P. Bermel, "Radiative cooling for thermophotovoltaic systems," in *Infrared Remote Sensing and Instrumentation XXIV*, vol. 9973. International Society for Optics and Photonics, 2016, p. 997308.

[97] L. Micheli, E. F. Fernández, F. Almonacid, T. K. Mallick, and G. P. Smestad, "Performance, limits and economic perspectives for passive cooling of high concentrator photovoltaics," *Solar Energy Materials and Solar Cells*, vol. 153, pp. 164–178, 2016.

[98] X. Sun, T. J. Silverman, Z. Zhou, M. R. Khan, P. Bermel, and M. A. Alam, "Optics-based approach to thermal management of photovoltaics: selective-spectral and radiative cooling," *IEEE Journal of Photovoltaics*, vol. 7, no. 2, pp. 566–574, 2017.

[99] K. Araki, H. Uozumi, and M. Yamaguchi, "A simple passive cooling structure and its heat analysis for 500/spl times/concentrator pv module," in *Conference Record of the Twenty-Ninth IEEE Photovoltaic Specialists Conference, 2002.* IEEE, 2002, pp. 1568–1571.

[100] F. Gualdi, O. Arenas, A. Vossier, A. Dollet, V. Aimez, and R. Arès, "Determining passive cooling limits in cpv using an analytical thermal model," in *AIP Conference Proceedings*, vol. 1556, no. 1. American Institute of Physics, 2013, pp. 10–13.

[101] S. K. Natarajan, T. K. Mallick, M. Katz, and S. Weingaertner, "Numerical investigations of solar cell temperature for photovoltaic concentrator system with and without passive cooling arrangements," *International journal of thermal sciences*, vol. 50, no. 12, pp. 2514–2521, 2011.

[102] M. A. Green, Y. Hishikawa, W. Warta, E. D. Dunlop, D. H. Levi, J. Hohl-Ebinger, and A. W. Ho-Baillie, "Solar cell efficiency tables (version 50)," *Progress in Photovoltaics: Research and Applications*, vol. 25, no. 7, pp. 668–676, 2017.

[103] M. Taguchi, A. Yano, S. Tohoda, K. Matsuyama, Y. Nakamura, T. Nishiwaki, K. Fujita, and E. Maruyama, "24.7% record efficiency hit solar cell on thin silicon wafer," *IEEE Journal of Photovoltaics*, vol. 4, no. 1, pp. 96–99, 2014.

[104] W. G. Rees, *Physical principles of remote sensing*. Cambridge university press, 2013.

[105] C. Min, C. Nuofu, Y. Xiaoli, W. Yu, B. Yiming, and Z. Xingwang, "Thermal analysis and test for single concentrator solar cells," *Journal of Semiconductors*, vol. 30, no. 4, p. 044011, 2009.

[106] A. Gentle and G. Smith, "Is enhanced radiative cooling of solar cell modules worth pursuing?" *Solar Energy Materials and Solar Cells*, vol. 150, pp. 39–42, 2016.

[107] R. Landauer, "Electrical conductivity in inhomogeneous media," in *AIP Conference Proceedings*, vol. 40, no. 1. American Institute of Physics, 1978, pp. 2–45.

[108] M. Rubin, "Optical properties of soda lime silica glasses," *Solar energy materials*, vol. 12, no. 4, pp. 275–288, 1985.

[109] D. Chen, "Anti-reflection (ar) coatings made by sol–gel processes: a review," *Solar Energy Materials and Solar Cells*, vol. 68, no. 3-4, pp. 313–336, 2001.

[110] H. Phillip and E. Taft, "Kramers-kronig analysis of reflectance data for diamond," *Physical Review*, vol. 136, no. 5A, p. A1445, 1964.

[111] E. D. Palik, *Handbook of optical constants of solids*. Academic press, 1998, vol. 3.

[112] F. C. Krebs, "Polymer solar cell modules prepared using roll-to-roll methods: knife-over-edge coating, slot-die coating and screen printing," *Solar Energy Materials and Solar Cells*, vol. 93, no. 4, pp. 465–475, 2009.

[113] H. Wu, D. Kong, Z. Ruan, P.-C. Hsu, S. Wang, Z. Yu, T. J. Carney, L. Hu, S. Fan, and Y. Cui, "A transparent electrode based on a metal nanotrough network," *Nature nanotechnology*, vol. 8, no. 6, p. 421, 2013.

[114] V. Liu and S. Fan, "S4: A free electromagnetic solver for layered periodic structures," *Computer Physics Communications*, vol. 183, no. 10, pp. 2233–2244, 2012.

[115] S. Kurtz *et al.*, "Opportunities and challenges for development of a mature concentrating photovoltaic power industry," 2009.

[116] P. Pérez-Higueras, F. J. Muñoz-Rodríguez, C. Adame-Sánchez, L. Hontoria-García, C. Rus-Casas, A. González-Rodríguez, J. D. Aguilar-Peña, F. J. Gallego-Álvarez, I. González-Luchena, and E. F. Fernández, "High-concentrator photovoltaic power plants: Energy balance and case studies," in *High Concentrator Photovoltaics*. Springer, 2015, pp. 443–477.

[117] S. De Wolf, A. Descoeudres, Z. C. Holman, and C. Ballif, "High-efficiency silicon heterojunction solar cells: A review," *green*, vol. 2, no. 1, pp. 7–24, 2012.

[118] "International Technology Roadmap for Photovoltaic (ITRPV) Ninth Edition," Tech. Rep. September, 2018. [Online]. Available: http://www.itrpv.net/Reports/Downloads/

[119] F. Colville, "Mono based PERC modules to drive bifacial market entry in 2018," 2017.

[120] K. Yoshikawa, H. Kawasaki, W. Yoshida, T. Irie, K. Konishi, K. Nakano, T. Uto, D. Adachi, M. Kanematsu, H. Uzu *et al.*, "Silicon heterojunction solar cell with interdigitated back contacts for a photoconversion efficiency over 26%," *Nature Energy*, vol. 2, no. 5, p. 17032, 2017.

[121] P. Zheng, X. Zhang, J. Liu, X. Yuan, L. Zha, W. Chen, and H. Jin, "Bifacial solar products light new pathway to future PV," p. 59, apr 2018.

[122] T. J. Silverman, M. G. Deceglie, and K. A. Horowitz, "NREL Comparative PV LCOE Calculator." mar 2018.

[123] J. Libal, D. Berrian, and R. Kopecek, "Overview: energy yield simulations and calculation of LCOE for bifacial PV systems," oct 2017.

[124] F. Fertig, S. Nold, N. Woehrle, J. Greulich, I. Haedrich, K. Karin, M. Mittag, D. Biro, S. Rein, and R. Preu, "Economic feasibility of bifacial silicon solar cells," *Progress in Photovoltaics: Research and Applications*, vol. 24, no. 6, pp. 800–817, jan 2016. [Online]. Available: https://doi.org/10.1002{%}2Fpip.2730

[125] M. Morales-Masis, S. De Wolf, R. Woods-Robinson, J. W. Ager, and C. Ballif, "Transparent electrodes for efficient optoelectronics," *Advanced Electronic Materials*, vol. 3, no. 5, p. 1600529, 2017.

[126] Y.-Y. Chen, L. Korte, C. Leendertz, J. Haschke, J.-Y. Gan, and D.-C. Wu, "Simulation of contact schemes for silicon heterostructure rear contact solar cells," *Energy Procedia*, vol. 38, pp. 677–683, 2013.

[127] D. Diouf, J.-P. Kleider, T. Desrues, and P.-J. Ribeyron, "Study of interdigitated back contact silicon heterojunctions solar cells by two-dimensional numerical simulations," *Materials Science and Engineering: B*, vol. 159, pp. 291–294, 2009.

[128] K. R. McIntosh, M. J. Cudzinovic, D. D. Smith, W. P. Mulligan, and R. M. Swanson, "The choice of silicon wafer for the production of low-cost rear-contact solar cells," in *Photovoltaic Energy Conversion, 2003. Proceedings of 3rd World Conference on*, vol. 1. IEEE, 2003, pp. 971–974.

[129] O. Nichiporuk, A. Kaminski, M. Lemiti, A. Fave, and V. Skryshevsky, "Optimisation of interdigitated back contacts solar cells by two-dimensional numerical simulation," *Solar energy materials and solar cells*, vol. 86, no. 4, pp. 517–526, 2005.

[130] N. Tucher, J. Eisenlohr, P. Kiefel, O. Höhn, H. Hauser, M. Peters, C. Müller, J. C. Goldschmidt, and B. Bläsi, "3d optical simulation formalism optos for textured silicon solar cells," *Optics Express*, vol. 23, no. 24, pp. A1720–A1734, 2015.

[131] P. Kowalczewski and L. C. Andreani, "Towards the efficiency limits of silicon solar cells: How thin is too thin?" *Solar Energy Materials and Solar Cells*, vol. 143, pp. 260–268, 2015.

[132] M. A. Green, "Lambertian light trapping in textured solar cells and light-emitting diodes: analytical solutions," *progress in Photovoltaics: Research and Applications*, vol. 10, no. 4, pp. 235–241, 2002.

[133] I. Synopsys, "Sentaurus Device User Guide, L-2016.03, Synopsys, Mountain View, CA, USA, 2013." mar 2016.

[134] M. M. Desa, S. Sapeai, A. Azhari, K. Sopian, M. Y. Sulaiman, N. Amin, and S. H. Zaidi, "Silicon back contact solar cell configuration: A pathway towards higher efficiency," *Renewable and Sustainable Energy Reviews*, vol. 60, pp. 1516–1532, 2016.

[135] D. L. Meier and D. K. Schroder, "Contact resistance: Its measurement and relative importance to power loss in a solar cell," *IEEE transactions on electron devices*, vol. 31, no. 5, pp. 647–653, 1984.

[136] D. Meier, E. Good, R. Garcia, B. Bingham, S. Yamanaka, V. Chandrasekaran, and C. Bucher, "Determining components of series resistance from measurements on a finished cell," in *Photovoltaic Energy Conversion, Conference Record of the 2006 IEEE 4th World Conference on*, vol. 2. IEEE, 2006, pp. 1315–1318.

[137] T. C. Russell, R. Saive, A. Augusto, S. G. Bowden, and H. A. Atwater, "The influence of spectral albedo on bifacial solar cells: A theoretical and experimental study," *IEEE Journal of photovoltaics*, vol. 7, no. 6, pp. 1611–1618, 2017.

[138] A. Reinders, P. Verlinden, and A. Freundlich, *Photovoltaic solar energy: from fundamentals to applications*. John Wiley & Sons, 2017.

[139] K. Masuko, M. Shigematsu, T. Hashiguchi, D. Fujishima, M. Kai, N. Yoshimura, T. Yamaguchi, Y. Ichihashi, T. Mishima, N. Matsubara *et al.*, "Achievement of more than 25% conversion efficiency with crystalline silicon heterojunction solar cell," *IEEE Journal of Photovoltaics*, vol. 4, no. 6, pp. 1433–1435, 2014.

[140] R. V. K. Chavali, J. V. Li, C. Battaglia, S. De Wolf, J. L. Gray, and M. A. Alam, "A generalized theory explains the anomalous suns–V_{OC} response of si heterojunction solar cells," *IEEE Journal of Photovoltaics*, vol. 7, no. 1, pp. 169–176, 2017.

[141] T. J. Silverman, M. G. Deceglie, X. Sun, R. L. Garris, M. A. Alam, C. Deline, and S. Kurtz, "Thermal and electrical effects of partial shade in monolithic thin-film photovoltaic modules," *IEEE Journal of Photovoltaics*, vol. 5, no. 6, pp. 1742–1747, 2015.

[142] R. Kamada, T. Yagioka, S. Adachi, A. Handa, K. F. Tai, T. Kato, and H. Sugimoto, "New world record cu (in, ga)(se, s) 2 thin film solar cell efficiency beyond 22%," in *2016 IEEE 43rd Photovoltaic Specialists Conference (PVSC)*. IEEE, 2016, pp. 1287–1291.

[143] T. Kato, "$Cu(In, Ga)(Se, S)_2$ solar cell research in solar frontier: Progress and current status," *Japanese Journal of Applied Physics*, vol. 56, no. 4S, p. 04CA02, 2017.

[144] P. Rostan, J. Mattheis, G. Bilger, U. Rau, and J. Werner, "Formation of transparent and ohmic zno: Al/mose2 contacts for bifacial cu (in, ga) se2 solar cells and tandem structures," *Thin Solid Films*, vol. 480, pp. 67–70, 2005.

[145] T. Nakada, "Microstructural and diffusion properties of cigs thin film solar cells fabricated using transparent conducting oxide back contacts," *Thin Solid Films*, vol. 480, pp. 419–425, 2005.

[146] M. Mazzer, S. Rampino, G. Spaggiari, F. Annoni, D. Bersani, F. Bissoli, M. Bronzoni, M. Calicchio, E. Gombia, A. Kingma *et al.*, "Bifacial cigs solar cells grown by low temperature pulsed electron deposition," *Solar Energy Materials and Solar Cells*, vol. 166, pp. 247–253, 2017.

[147] N. Cavallari, F. Pattini, S. Rampino, F. Annoni, M. Barozzi, M. Bronzoni, E. Gilioli, E. Gombia, C. Maragliano, M. Mazzer *et al.*, "Low temperature deposition of bifacial cigs solar cells on al-doped zinc oxide back contacts," *Applied Surface Science*, vol. 412, pp. 52–57, 2017.

[148] G. Agostinelli, A. Delabie, P. Vitanov, Z. Alexieva, H. Dekkers, S. De Wolf, and G. Beaucarne, "Very low surface recombination velocities on p-type silicon wafers passivated with a dielectric with fixed negative charge," *Solar Energy Materials and Solar Cells*, vol. 90, no. 18-19, pp. 3438–3443, 2006.

[149] B. Hoex, J. Schmidt, R. Bock, P. Altermatt, M. Van De Sanden, and W. Kessels, "Excellent passivation of highly doped p-type si surfaces by the negative-charge-dielectric al 2 o 3," *Applied Physics Letters*, vol. 91, no. 11, p. 112107, 2007.

[150] W.-W. Hsu, J. Chen, T.-H. Cheng, S. Lu, W.-S. Ho, Y.-Y. Chen, Y.-J. Chien, and C. Liu, "Surface passivation of cu (in, ga) se2 using atomic layer deposited al2o3," *Applied Physics Letters*, vol. 100, no. 2, p. 023508, 2012.

[151] B. Vermang, J. T. Wätjen, C. Frisk, V. Fjällström, F. Rostvall, M. Edoff, P. Salomé, J. Borme, N. Nicoara, and S. Sadewasser, "Introduction of si perc rear contacting design to boost efficiency of $Cu(In, Ga)Se$ solar cells," *IEEE Journal of Photovoltaics*, vol. 4, no. 6, pp. 1644–1649, 2014.

[152] Y. Sun, Z. Zhou, R. Asadpour, M. A. Alam, and P. Bermel, "Tailoring interdigitated back contacts for high-performance bifacial silicon solar cells," *Applied Physics Letters*, vol. 114, no. 10, p. 103901, 2019.

[153] M. Xu, A. J. Wachters, J. van Deelen, M. C. Mourad, and P. J. Buskens, "A study on the optics of copper indium gallium (di) selenide (cigs) solar cells with ultra-thin absorber layers," *Optics express*, vol. 22, no. 102, pp. A425–A437, 2014.

[154] M. Gloeckler, A. Fahrenbruch, and J. Sites, "Numerical modeling of cigs and cdte solar cells: setting the baseline," in *Proceedings of 3rd World Conference on Photovoltaic Energy Conversion*, vol. 1, no. 1, 2003, pp. 491–494.

[155] K. Taretto, U. Rau, and J. Werner, "Numerical simulation of grain boundary effects in cu (in, ga) se2 thin-film solar cells," *Thin Solid Films*, vol. 480, pp. 8–12, 2005.

[156] K. F. Tai, R. Kamada, T. Yagioka, T. Kato, and H. Sugimoto, "From 20.9 to 22.3% cu (in, ga)(s, se) 2 solar cell: Reduced recombination rate at the heterojunction and the depletion region due to k-treatment," *Japanese Journal of Applied Physics*, vol. 56, no. 8S2, p. 08MC03, 2017.

[157] L. Assmann, J. Bernede, A. Drici, C. Amory, E. Halgand, and M. Morsli, "Study of the mo thin films and mo/cigs interface properties," *Applied Surface Science*, vol. 246, no. 1-3, pp. 159–166, 2005.

[158] R. C. Statistics, "International renewable energy agency (irena), march 2019," 2019.

[159] B. L. Sopori and P. Sheldon, "Screening of silicon wafers used in photovoltaics," Aug. 30 2011, uS Patent 8,006,566.

[160] R. Ramaprabha and B. Mathur, "Intelligent controller based maximum power point tracking for solar pv system," *International Journal of Computer Applications*, vol. 12, no. 10, pp. 37–41, 2011.

[161] C. Wei, Z. Zhang, W. Qiao, and L. Qu, "Reinforcement-learning-based intelligent maximum power point tracking control for wind energy conversion systems," *IEEE Transactions on Industrial Electronics*, vol. 62, no. 10, pp. 6360–6370, 2015.

[162] M. A. Islam and M. A. Kabir, "Neural network based maximum power point tracking of photovoltaic arrays," in *TENCON 2011-2011 IEEE Region 10 Conference*. IEEE, 2011, pp. 79–82.

[163] H. Abdelrahman, F. Berkenkamp, J. Poland, and A. Krause, "Bayesian optimization for maximum power point tracking in photovoltaic power plants," in *2016 European Control Conference (ECC)*. IEEE, 2016, pp. 2078–2083.

[164] Z. Ren, F. Oviedo, M. Thway, S. I. Tian, Y. Wang, H. Xue, J. D. Perea, M. Layurova, T. Heumueller, E. Birgersson *et al.*, "Embedding physics domain knowledge into a bayesian network enables layer-by-layer process innovation for photovoltaics," *npj Computational Materials*, vol. 6, no. 1, pp. 1–9, 2020.

[165] B. Cao, L. A. Adutwum, A. O. Oliynyk, E. J. Luber, B. C. Olsen, A. Mar, and J. M. Buriak, "How to optimize materials and devices via design of experiments and machine learning: Demonstration using organic photovoltaics," *ACS nano*, vol. 12, no. 8, pp. 7434–7444, 2018.

[166] J. Li, J. K. Ward, J. Tong, L. Collins, and G. Platt, "Machine learning for solar irradiance forecasting of photovoltaic system," *Renewable energy*, vol. 90, pp. 542–553, 2016.

[167] D. Assouline, N. Mohajeri, and J.-L. Scartezzini, "Quantifying rooftop photovoltaic solar energy potential: A machine learning approach," *Solar Energy*, vol. 141, pp. 278–296, 2017.

[168] Y. Buratti, J. Dick, Q. Le Gia, and Z. Hameiri, "A machine learning approach to defect parameters extraction: Using random forests to inverse the shockley-read-hall equation," in *2019 IEEE 46th Photovoltaic Specialists Conference (PVSC)*. IEEE, 2019, pp. 3070–3073.

[169] E. Garoudja, A. Chouder, K. Kara, and S. Silvestre, "An enhanced machine learning based approach for failures detection and diagnosis of pv systems," *Energy conversion and management*, vol. 151, pp. 496–513, 2017.

[170] M. Dhimish, V. Holmes, B. Mehrdadi, and M. Dales, "Comparing mamdani sugeno fuzzy logic and rbf ann network for pv fault detection," *Renewable Energy*, vol. 117, pp. 257–274, 2018.

[171] S. Lloyd, "Least squares quantization in pcm," *IEEE transactions on information theory*, vol. 28, no. 2, pp. 129–137, 1982.

[172] T. Song, A. Kanevce, and J. R. Sites, "Emitter/absorber interface of cdte solar cells," *Journal of Applied Physics*, vol. 119, no. 23, p. 233104, 2016.

[173] J. M. Kephart, R. M. Geisthardt, and W. Sampath, "Optimization of cdte thin-film solar cell efficiency using a sputtered, oxygenated cds window layer," *Progress in Photovoltaics: Research and Applications*, vol. 23, no. 11, pp. 1484–1492, 2015.

[174] J. M. Burst, J. N. Duenow, D. S. Albin, E. Colegrove, M. O. Reese, J. A. Aguiar, C.-S. Jiang, M. Patel, M. M. Al-Jassim, D. Kuciauskas *et al.*, "Cdte solar cells with open-circuit voltage breaking the 1 v barrier," *Nature Energy*, vol. 1, no. 3, pp. 1–8, 2016.

[175] A. Gupta, V. Parikh, and A. D. Compaan, "High efficiency ultra-thin sputtered cdte solar cells," *Solar Energy Materials and Solar Cells*, vol. 90, no. 15, pp. 2263–2271, 2006.

[176] J. Han, C. Spanheimer, G. Haindl, G. Fu, V. Krishnakumar, J. Schaffner, C. Fan, K. Zhao, A. Klein, and W. Jaegermann, "Optimized chemical bath deposited cds layers for the improvement of cdte solar cells," *Solar Energy Materials and Solar Cells*, vol. 95, no. 3, pp. 816–820, 2011.

[177] I. Irfan, H. Lin, W. Xia, H. N. Wu, C. W. Tang, and Y. Gao, "The effect of moox inter-layer on thin film cdte/cds solar cell," *Solar energy materials and solar cells*, vol. 105, pp. 86–89, 2012.

[178] S. Demtsu and J. Sites, "Effect of back-contact barrier on thin-film cdte solar cells," *Thin Solid Films*, vol. 510, no. 1-2, pp. 320–324, 2006.

[179] ——, "Quantification of losses in thin-film cds/cdte solar cells," in *Conference Record of the Thirty-first IEEE Photovoltaic Specialists Conference, 2005.* IEEE, 2005, pp. 347–350.

[180] A. D. Compaan, A. Gupta, S. Lee, S. Wang, and J. Drayton, "High efficiency, magnetron sputtered cds/cdte solar cells," *Solar Energy*, vol. 77, no. 6, pp. 815–822, 2004.

[181] R. G. Dhere, J. N. Duenow, C. M. DeHart, J. V. Li, D. Kuciauskas, and T. A. Gessert, "Development of substrate structure cdte photovoltaic devices with performance exceeding 10%," in *2012 38th IEEE Photovoltaic Specialists Conference*. IEEE, 2012, pp. 003 208–003 211.

[182] J. Perrenoud, L. Kranz, C. Gretener, F. Pianezzi, S. Nishiwaki, S. Buecheler, and A. Tiwari, "A comprehensive picture of cu doping in cdte solar cells," *Journal of Applied Physics*, vol. 114, no. 17, p. 174505, 2013.

[183] R. Kotikalapudi and contributors, "keras-vis," https://github.com/raghakot/keras-vis, 2017.

[184] D. P. Kingma and J. Ba, "Adam: A method for stochastic optimization," *arXiv preprint arXiv:1412.6980*, 2014.

[185] B. Bengfort, R. Bilbro, N. Danielsen, L. Gray, K. McIntyre, P. Roman, Z. Poh *et al.*, "Yellowbrick," 2018. [Online]. Available: http://www.scikit-yb.org/en/latest/

[186] C. Cortes and V. Vapnik, "Support-vector networks," *Machine learning*, vol. 20, no. 3, pp. 273–297, 1995.

VITA

VITA

Yubo Sun was born in Nanjing, China on January 21, 1989. He received Bachelor degree of Science in Electrical Engineering from Purdue University, West Lafayette in December, 2012. He continued his pursuit of Ph.D degree in the department of Electrical and Computer Engineering at Purdue University. He joined Prof. Bermel's research group in January of 2014 and became a member of Network for Photovoltaics Technology (NPT) group. His research interests include physics-based device modeling and simulation of photovoltaic devices, design and optimization of novel photovoltaic cells. He has a solid background in semiconductor device physics and multi-physics simulations that require coupling of optics, electronics and phonons. He is competent in using various numerical & statistical tool, which includes but not limited to Sentaurus TCAD, HSPICE, COMSOL Multiphysics, and Matlab etc. He is also proficient using cutting-edge machine learning tools and libraries (i.e. Keras, Scikit-Learn, and TensorFlow) for data analysis in research of interest. He is interested in discovering novel conceptual design of Photovoltaics, providing physical insights and paving the pathway for future improvement in PV industry.